Impacts of giant cloud condensation nuclei on precipitation formation in marine low clouds

Katherine Elise Mifsud

A thesis submitted in partial fulfillment

of the requirements of the degree of

Master of Science

University of Washington

2025

Committee:

Rob Wood

Roger Marchand

Peter Blossey

Program Authorized to Offer Degree

Department of Atmospheric and Climate Science

University of Washington

Abstract

Impacts of giant cloud condensation nuclei on precipitation formation in marine low clouds

Katherine Mifsud

Chair of the Supervisory Committee:
Robert Wood
Department of Atmosphere and Climate Science

Precipitation in low clouds strongly affects cloud responses to aerosol perturbations, thereby impacting aerosol radiative forcing of climate, a significant but indeterminate contribution to uncertainty in future warming. The onset of drizzle formation in marine low clouds may be influenced by the presence of coarse-mode sea salt aerosols with dry diameters exceeding 1 um. These particles can, under some circumstances, act as giant cloud condensation nuclei (GCCN) that benefit from rapid condensational growth to a size that initiates collision-coalescence. Aircraft-based in-situ observations of cloud microphysical properties and aerosol size distributions from the Aerosol-Cloud-Meteorology Interactions Over the Western Atlantic Experiment (ACTIVATE) are analyzed from January to June 2022. ACTIVATE focused on making detailed in situ microphysical measurements of aerosols and clouds using a low-flying research aircraft. The western Atlantic region is ideal for this study due to its location in the midlatitudes, where diverse cloud types can be observed under varying meteorological conditions. Unlike many aerosol-cloud interaction studies focused on subtropical regions, ACTIVATE's emphasis on the midlatitudes provides a unique opportunity to examine aerosol impacts on precipitation formation in an area characterized by complex cloud structures and dynamic atmospheric processes.

Observations from a cloud aerosol spectrometer (CAS) and a cloud droplet probe (CDP) in clear air from just below the cloud base are used to quantify size distributions of haze droplets. Clear-sky conditions for accurate interpretation of the size distributions are identified by strictly filtering for liquid water content below 0.0025 g/m^3 to remove contamination from cloud droplets and total precipitation number concentration below 100 particles per cubic meter ($\#/m^3$), as measured by a two-dimensional stereo probe. These thresholds ensure that the size distributions measure haze droplets without cloud or drizzle droplet contamination. Haze droplet size distributions reveal modest correlations with near surface-level wind speeds when averaged together into wind speed bins, a result consistent with other recent studies. This is seen by a strong correlation coefficient between wind speed and total concentration of $R = 0.90$ for the CAS and $R = 0.84$ for the CDP. And consequently, I conclude, as near surface wind speed increases, the production of giant cloud condensation nuclei increases.

Observed GCCN distributions and cloud thicknesses are used to drive simulations with an explicit microphysics parcel model, exploring the conditions under which the observed range of GCCN induces a first-order impact on precipitation rates. Analysis of droplet size distributions using a 1-dimensional kinematic super-droplet cloud model (PySDM) demonstrates that even the addition of a small number of GCCN accelerates the onset of drizzle and increases drizzle rate in the marine boundary layer. This effect was analyzed under conditions with liquid water paths similar to those in the thicker parts of low cloud fields over the Western Atlantic region. Similarly, analysis with observationally derived rainwater content as a function of total concentration and liquid water content for high and low GCCN concentrations reveals an increased ratio of condensate in precipitation drops to that in cloud drops for flights with higher measured concentrations of GCCN. These results suggest that GCCN can meaningfully influence precipitation in marine low clouds.

TABLE OF CONTENTS

LIST OF FIGURES

LIST OF TABLES

ACKNOWLEDGEMENTS

This research was supported by award NASA EVS-3 ACTIVATE (award 80NSSC23K0906). We thank Gao Chen, Michael Shook, Ewan Crosbie, and Armin Sorooshian for their help in identifying and selecting ACTIVATE datasets.

1. Introduction

a. Importance of Cloud-Aerosol Interactions in Climate

Cloud-aerosol interactions have a significant impact on climate, particularly through their influence on marine stratocumulus clouds, which cover roughly 20% of the planet's oceans and play a dominant role in modulating Earth's radiative energy balance (Hartmann and Short 1980). These interactions affect both cloud microphysics and macrophysics, including cloud albedo and lifetime, thereby altering the reflection of solar radiation and the overall radiative forcing of the climate system (Seinfeld et al., 2016). The stratocumulus-topped boundary layer (STBL) is essential to ocean-atmosphere dynamics and general circulation over midlatitude oceans (Nicholls et al., 1979). By regulating heat, moisture, and momentum exchanges between the ocean and atmosphere, the STBL profoundly influences large-scale climate systems (Wood 2012). Furthermore, marine stratocumuli reflect a large portion of the Earth's incoming solar radiation, while only minimally contributing to outgoing longwave radiation (Chen et al., 2000). This combination of radiative effects and expansive coverage makes stratocumulus clouds integral to the planet's overall radiative budget (Stephens and Greenwald 1991; Hartmann et al. 1992; L'Ecuyer et al., 2019; Wood 2021).

Unfortunately, clouds are the largest uncertainty in estimates and interpretations of the Earth's rapidly changing energy budget, and much of the uncertainty revolves around how aerosols interact with stratocumulus clouds (Pachauri et al., 2014, Bellouin et al., 2020). The Twomey effect describes how increases in cloud droplet concentration result from aerosol-cloud interactions (ACI). These increases reduce droplet size and increase total droplet surface area. As a result, clouds reflect more solar radiation, even without changes in cloud liquid water content. However, changes in droplet size can also alter cloud macrophysical properties (fractional coverage and cloud liquid water) by changing precipitation efficiency and by microphysical effects on cloud top entrainment rate (Bellouin et al., 2020; Seinfeld et al., 2016, Wood et al., 2024). The Twomey effect results in a negative radiative forcing, which leads to cooling. However, changes in cloud macrophysical properties due to aerosol perturbations can either amplify or offset this cooling, depending on the prevailing meteorological conditions and the characteristics of the clouds and boundary layer (Lohmann and Feichter 2005). Recent studies (Watson-Parris and Smith, 2022; Wood et al., 2024) suggest that aggressive aerosol mitigation policies, aimed at reducing air pollution and improving public health, is inadvertently exacerbating global warming by diminishing the cooling effect of aerosols. This highlights the complex interplay between aerosol mitigation and climate policy, further underscoring the need for a better understanding of aerosol-cloud interactions to accurately predict future climate scenarios (Persad et al., 2022).

The stratocumulus-topped boundary layer (STBL) forms under stable, often subsiding, lower tropospheric conditions, where sensible heat fluxes, surface heat fluxes, cloud-top entrainment, cloud-top radiative cooling, and turbulent mixing in the boundary layer create an environment conducive to the persistence of the marine stratocumulus clouds that are so integral to the planet's overall radiative budget (Wood and Bretherton 2006; Klein and Hartmann 1993; Lilly 1968; Wood 2012). Precipitation in marine stratocumuli is also essential to boundary layer dynamics, as it redistributes water vapor and heat, and can influence a cloud's lifetime and albedo (Feingold et al., 1996; Stevens et al., 1998b; Wood et al., 2009). Drizzle, in particular, peaks near the cloud base and can stabilize the STBL by warming the cloud layer and cooling the subcloud layer, leading to reduced turbulent mixing and increased stratification (Nicholls, 1984; Stevens et al., 1998; Ackerman et al., 2009, Wood 2005a; Wood 2012; vanZanten et al. 2005). Understanding drizzle in marine stratocumulus clouds is critical because it plays a key role in regulating cloud lifetime and boundary layer structure, both of which affect global climate systems. However, drizzle processes remain challenging to quantify making them a persistent source of uncertainty in climate models (Stevens and Feingold, 2009).

b. Aerosol-cloud-precipitation interactions

Additionally, aerosol-induced changes in precipitation in low clouds within the marine stratocumulus-topped boundary layer (STBL) affect cloud macrophysical adjustments to aerosol perturbations, thereby impacting aerosol radiative forcing of climate (Albrecht et al., 1989; Ackerman et al., 2004; Chen et al., 2012). These aerosol-cloud-precipitation interactions can induce what are known as cloud lifetime effects, which are the macrophysical cloud responses to aerosol changes (Stevens and Feingold, 2009). As these interactions occur on sub-kilometer scales, climate models poorly represent these cloud adjustments, limiting their representation and understanding of their full effects (Mülmenstädt and Feingold 2018). Cloud condensation nuclei (CCN) are aerosol particles that serve as the initial sites for cloud droplet formation and their availability are determined by the size, composition, and concentration of aerosols, plays a crucial role in aerosol-cloud-precipitation processes. When combined with updraft strength, CCN concentration influences the number and size of cloud droplets, which in turn affects the formation of drizzle and the overall precipitation efficiency of the cloud (Twomey, 1977; Martin et al. 1994; Jensen and Lee 2008; Wood 2012; Rosenfeld et al., 2019). After CCN activate into cloud droplets, the efficacy of collision-coalescence becomes a key factor in drizzle formation. Collision efficiency decreases strongly for cloud droplets with radii significantly smaller than ~10 μm (Berry 1967; Wood et al., 2009). Collision–coalescence is more efficient in clouds with fewer but larger droplets, enhancing the formation of precipitation (Albrecht et al., 1989). Another pathway for drizzle formation can be achieved through the existence of a tail of large "collector" droplets formed on giant cloud condensation nuclei (GCCN) that can initiate collision-coalescence (Ludlam 1951; Johnson 1982; Feingold et al., 1999; Jensen and Lee 2008, Jensen and Nugent 2017; Dziekan et al., 2021).

c. Giant cloud condensation nuclei

In marine environments, sea spray aerosols serve as a significant source of giant cloud condensation nuclei (Woodcock 1953; Feingold et al., 1999; Jensen and Nugent 2017; Dziekan et al., 2021). They are a huge source of particulate matter in the atmosphere and produce about 3–30 Pg yr^{-1} globally (Lewis and Schwartz, 2004; Grythe et al., 2014). Due to their chemical makeup, sea spray aerosols (SSA) are highly soluble and more likely to promote hygroscopic growth in a saturated environment and drive collision and coalescence (Petters and Kreidenweis 2007). Sea salt aerosols in the size range of interest for this study are primarily generated by the bursting of air bubbles at the ocean surface (Woodcock 1953). However, not all sea spray aerosols originate from bubble bursting. Under high wind conditions, typically exceeding 7–11 m s^{-1}, larger "spume" drops can form as wave crests are torn apart, injecting ultra-large sea salt particles into the marine boundary layer (O'Dowd 1995). While spume drops contribute to the overall sea spray aerosol population, the coarse-mode particles investigated in this study are more closely associated with bubble bursting.

While not all sea salt aerosols are large enough to serve as GCCN, those with a dry diameter larger than 1 μm can grow rapidly in cloud by condensation due to their high salt concentration. This process may allow some GCCN to grow larger than the more numerous cloud droplets formed on accumulation mode aerosol, enabling them to fall and collect smaller droplets, thereby initiating precipitation. By introducing larger droplets into the cloud system, the efficiency of converting cloud water into precipitation-sized drops is increased.

If the same cloud water is spread over smaller and more numerous cloud droplets, it will have the opposite effect; reducing precipitation efficiency and nominally extending the cloud lifetime (Twomey 1977; Wood et al., 2009). However, this decrease in cloud droplet size leads to a decrease in terminal velocity. These smaller droplets then sediment more slowly and cause an overall decrease in sedimentation of cloud liquid water near the cloud top inversion (Ackerman et al, 2004; Bretherton et al, 2007). This weaker sedimentation allows liquid water to remain near the cloud top, increasing evaporation rates, enhancing entrainment efficiency, potentially drying out the cloud layer, and reducing cloud lifetime.

d. Wind speed dependence and GCCN emissions

Evidence suggests that sea salt aerosol size distributions in the lower MBL are controlled by low-level wind speed across the ocean surface (Woodcock 1953; Monahan et al., 1983; Colón-Robles et al., 2006; Jensen and Lee 2008; Grythe et al., 2014). Previous efforts to constrain the process by which CCN activate into cloud droplets (Snider et al. 2003; Fountoukis et al. 2007) also identify a distinct connection between aerosol size and the vertical wind speed to the number of aerosols that activate. However, while past studies show that wind speed might be a key driver in sea salt aerosol production, other studies show that at similar wind speeds, wave dynamics, sea surface temperature (SST), and MBL depth may also play a crucial role (Dana & Hales, 1976; Skartveit, 1982; Lewis and Schwartz 2004; Jaeglé et al. 2011; Grythe et al., 2014). For example, Salter et al., 2015 demonstrate an increase in the production of sea salt aerosols larger than 1 um diameter with increasing SST. There are numerous source functions for sea salt aerosol production, each accounting for different mechanisms and environmental factors, which highlights the complexity of SSA generation (Lewis et al., 2004). Although the generation of sea salt aerosols can be influenced by multiple factors, wind speed remains a key variable due to its direct impact on the production of larger aerosols, which may act as giant cloud condensation nuclei. However, there is still strong variability in sea salt aerosol size distributions as a function of wind speed, as evident in the later Section 3b, which shows a range of observed distributions from multiple studies for similar wind speed conditions (Lewis and Schwartz 2004). The spread across different datasets highlights the complexity of aerosol generation processes beyond just wind speed influences.

e. GCCN and condensational growth

Condensational growth of the GCCN from the ocean surface through the cloud is important for growing to a size where they can initiate collision-coalescence (see Ludlam 1951) but has not been incorporated into physical parameterizations used in bulk microphysical models to this point, which can lead to an underestimation of warm rain formation (Jensen and Nugent 2017). Cloud droplets grown on

GCCN are highly concentrated solutions compared with the majority of cloud droplets, which are grown on much smaller accumulation mode aerosol particles. This makes the process of condensational growth of GCCN different than for accumulation mode CCN; it is accelerated via the Raoult effect (Jensen and Nugent 2017) and in some cases, may lead to a faster onset of warm drizzle (L'Ecuyer et al., 2009). The fundamental challenge to representing GCCN in microphysical models is that the condensational growth rate of cloud droplets depends not only on their size but also on the dry radius of the salt they contain. Only a few GCCN-containing "lucky droplets" would be needed to initiate collision-coalescence. Thus, GCCN-containing droplets must be treated as a distinct category of cloud hydrometeor, increasing model complexity. It is difficult to accurately capture this even in bin microphysical models, but super droplet methods are able to achieve the desired complexity (Shima et al., 2009; Shima et al., 2020; Li at al., 2022; Zmijewski et al., 2024). The Python Super-Droplet Method (PySDM) can achieve this (Bartmann et al., 2021, Azimi et al., 2024). Furthermore, since droplets formed on GCCN remain highly concentrated salt solutions, they can more easily resist evaporation and the larger GCCN can even continue growing by condensation as they descend through subsaturated downdrafts (Jensen and Nugent 2017). This contrasts with smaller cloud droplets grown on accumulation mode aerosol, which typically lose mass and may completely evaporate in similar conditions.

f. Research gaps and the need for further study

Despite advances in understanding GCCN's role in collisional growth, significant uncertainties remain. For example, past studies have used a wide range of GCCN sizes and concentrations, making direct intercomparison challenging. Jensen and Nugent (2017) estimated that at the 1 μm diameter size range, a concentration of 0.3 cm^{-3} could have a direct, non-negligible influence on drizzle formation. In contrast, Feingold et al. (1999) investigated significantly larger GCCN, with a 20 μm radius, and found that a much lower concentration on the order of 10^{-4} to 10^{-2} cm^{-3} was sufficient to enhance precipitation. Feingold et al. (1999) circumvented the problem of GCCN condensational growth by simply introducing 20-micron cloud droplets into the model, with the implicit assumption that these grew on GCCN. These differences in assumed particle size and concentration, as well as variations in the microphysical modeling approach, highlight the difficulty in comparing results across studies. Some studies have used the Super Droplet Method (SDM) (Dziekan et al., 2021), while others have relied on bulk or bin microphysics, each introducing unique assumptions and limitations. A stronger understanding of GCCN's impact on collision-coalescence and thus on drizzle formation is critical for improving cloud and precipitation parameterizations in climate models, particularly in marine stratocumulus regions where sea salt aerosols are abundant and can serve as GCCN. This knowledge can help reduce uncertainties in aerosol-cloud-precipitation interactions and their influence on global climate.

This thesis aims to address critical gaps in our understanding of coarse-mode cloud-aerosol interactions in marine stratocumulus clouds. We utilize the robust observational framework established by the NASA Sub-Orbital Aerosol-Cloud-Meteorology Interactions over the Western Atlantic Experiment (ACTIVATE) field campaign to answer these questions. The motivating research objectives of this campaign included improving process-level understanding and model representation of factors that govern cloud microphysical and macrophysical properties, how they impact cloud interactions with aerosols, the improvement of model parameterizations of aerosol activation and cloud formation, and the quantification of aerosol particle number concentration, cloud condensation nuclei concentration, and cloud droplet number concentration relationships (Sorooshian et al., 2023). ACTIVATE's objectives have helped frame our research goals.

Following a description of the data sources used in the current work (section 2), in section 3a we break down each flight into discrete legs to derive size-resolved aerosol concentration profiles from below the cloud base to within the cloud. This approach allows us to validate our measurements against established literature across different seasons, thereby assessing the universality of the coarse mode aerosols in various meteorological regimes.

Building on previous work (e.g., Woodcock, 1953; Colón-Robles et al., 2006), section 3b examines how near-surface wind speed influences the concentration and size distribution of these coarse-mode aerosols. This involves taking the size-resolved aerosol concentration profiles and binning them by flight leg averaged, near surface, ten-meter wind speed to understand the extent to which wind speed - coarse mode concentration relationships are universal.

Finally, section 3c investigates the extent to which variations in giant cloud condensation nuclei concentrations can modulate precipitation in marine stratocumulus clouds. We use a condensational growth model (PySDM) for the dry GCCN distributions (converted from ambient) to grow the droplets on their journey from the near-surface region where they are produced to the top of the cloud where they can potentially initiate precipitation. The goal is to determine whether and to what extent the presence of GCCN alters the cloud droplet size distribution and accelerates precipitation processes under varying aerosol and meteorological conditions. By comparing our modeled precipitation responses with observed size distributions and observations from the campaign, we can determine if higher concentrations of GCCN are linked to enhanced drizzle formation. This analysis is necessary not only to improve our understanding of aerosol-cloud interactions but also to contribute to better parameterizations, that include the impact of GCCN.

2. Data

The role of this section is to introduce the in-situ observations used in this study which were collected as part of the Aerosol-Cloud-Meteorology Interactions Over the Western Atlantic Experiment (ACTIVATE). The use of this dataset is extremely beneficial to the research study as it contains an unprecedented amount of data for meteorological, cloud, and aerosol properties over the western North Atlantic over several years. This allows us a wide range of conditions to look at different wind speeds and meteorological states, as well as examine aerosol conditions between clean and polluted states. The following subsections provide an overview of the campaign's purpose and setup, details on the instrumentation used, and descriptions of data sampling techniques. Data pre-processing will be detailed later with our methods.

A. ACTIVATE

ACTIVATE is a NASA Sub-Orbital field campaign that ran for five years, from January 2019 through June 2023 (Figure 1; Table 1). with the intent of providing globally important data detailing changes in warming and cooling planetary feedbacks, atmospheric aerosols and sources, and marine boundary layer cloud systems (Sorooshian et al., 2023). The observations relative to our research were collected in two deployments spanning from January to June 2022 in an attempt to capture different seasonal states to broaden the range of aerosol and meteorological conditions for analysis. Fieldwork plans were structured with a twin-flight (meaning two aircraft are flying together) design from NASA Langley Research Center in Virgina, North America out over the Western Atlantic and over Bermuda, where our observations were collected.

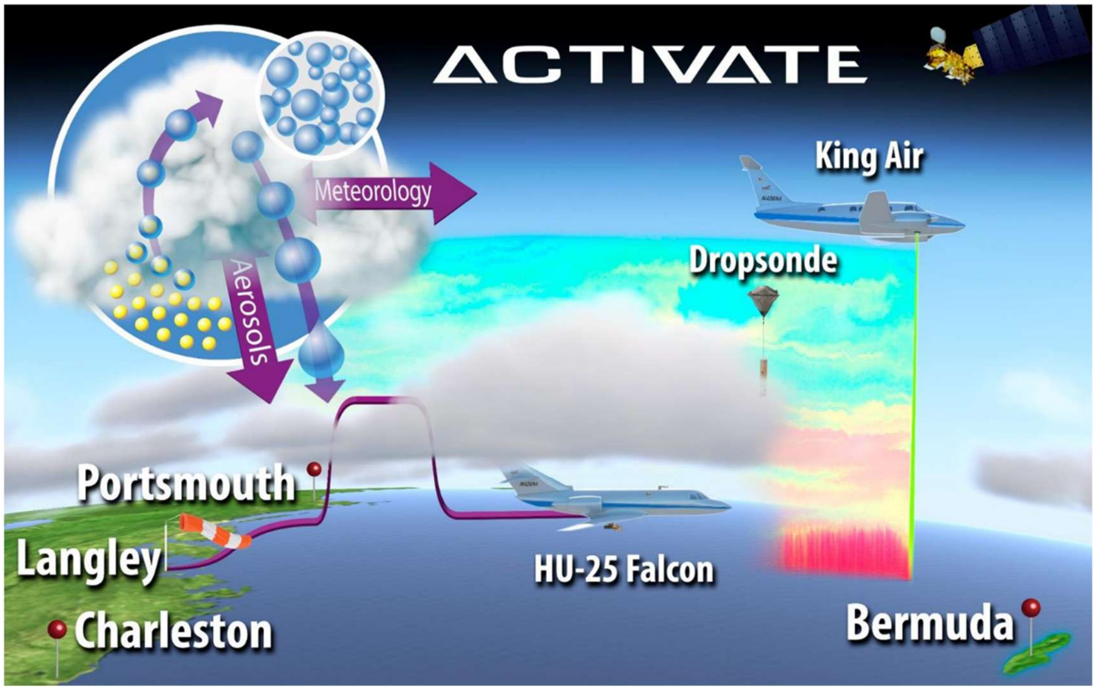

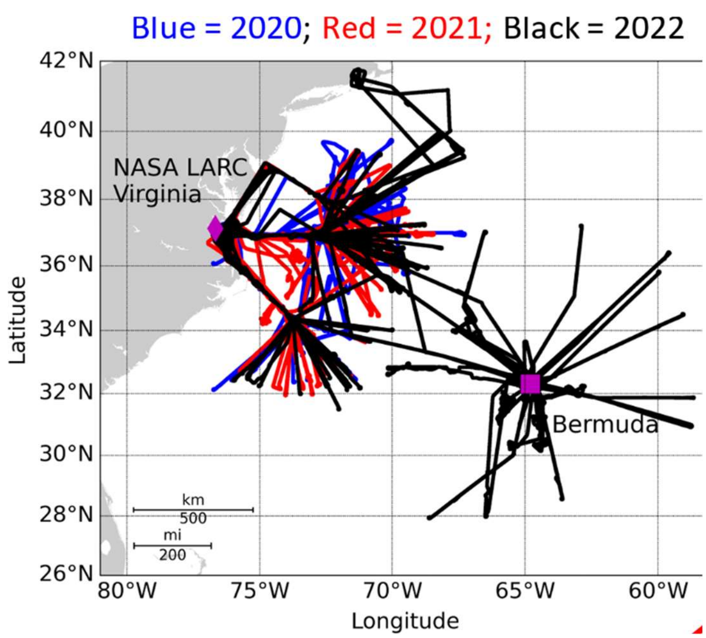

Figure 1 Overall ACTIVATE flight schematic and study region. Both the King Air and the Falcon leave from NASA Langley and fly over the Western Atlantic and over Bermuda to collect three years of data across multiple seasons (upper). The individual flight paths for each experimental year. 2020 flights are shown in blue, 2021 flights are shown in red, and 2022 flights are shown in black (lower). 2022 is the only year in which data was collected from over Bermuda (Sorooshian et al., 2023).

	Research Flights			Flight Hours		Joint Ensembles	
	Falcon	King Air	Joint	Falcon	King Air	Cloudy	Clear
Winter 2020	22	17	17	73	59	43	28
Summer 2020	18	18	18	60	67	58	36
* Winter 2021	17	19	15	56	66	47	25
Summer 2021	32	32	32	106	108	103	74
Winter 2021-2022	55	54	53	182	193	198	72
Summer 2022	30	28	27	97	98	86	46
Sum	***174***	***168***	***162***	***574***	***592***	***535***	***281***
Baseline Mission End Goal						250	15

Table 2 Table depicting the amount of flights for each season across all flight deployments for each aircraft. The important thing to note is that there were 162 joint flights in total and close to 600 hours of joint flight time (Sorooshian 2022).

i. Purpose and scope of the campaign

The campaign's data collection goals centered around low clouds over the Western Atlantic spanning the continuum of stratiform and cumulus clouds with post-frontal conditions, while also targeting model-based representations of various aerosol-cloud-meteorology-related interactions (Sooroshian et al., 2023). The experiment's explicit objectives include improving scientific understanding of how aerosol concentrations, cloud condensation nuclei (CCN), and cloud droplet populations are interconnected; gathering a comprehensive dataset that can be leveraged internationally for model intercomparison and detailed process studies; assessing current remote sensing techniques and refining approaches for future satellite missions; and enhancing satellite-based retrieval methods for cloud droplet numbers and CCN indicators (Sorooshian et al., 2023). To achieve these objectives, the focus remains on marine low clouds across a range of aerosol levels and weather scenarios, ensuring a robust dataset that can reveal critical links among aerosols, clouds, and meteorological conditions.

ii. Field set-up and flight schematics

The distinct advantage of a twin-aircraft flight dynamic over a single-aircraft study is the enablement of near-simultaneous, multi-level sampling of the boundary layer. In this campaign, the high-flying aircraft, the King Air, and the low-flying aircraft, the HU-25 Falcon, were in tight coordination in time and space (Sorooshian et al., 2023). This allows the full utilization of various instruments at different altitudes to capture a range of measurements across the boundary layer. Furthermore, this dual-platform approach minimizes temporal and spatial mismatches that can occur when relying on a single aircraft thus improving our ability to characterize aerosol-cloud interactions with higher accuracy. The direct comparison between remote sensing observations and in-situ measurements collected simultaneously offers a comprehensive picture of the vertical structure of aerosol properties and cloud-aerosol interactions. The data used for our research came from statistical survey missions, which captured measurements from about 150 m above the ocean surface to just below the boundary layer, though we utilize data only from 150 m above the surface to about 2.5 km (Figure 2).

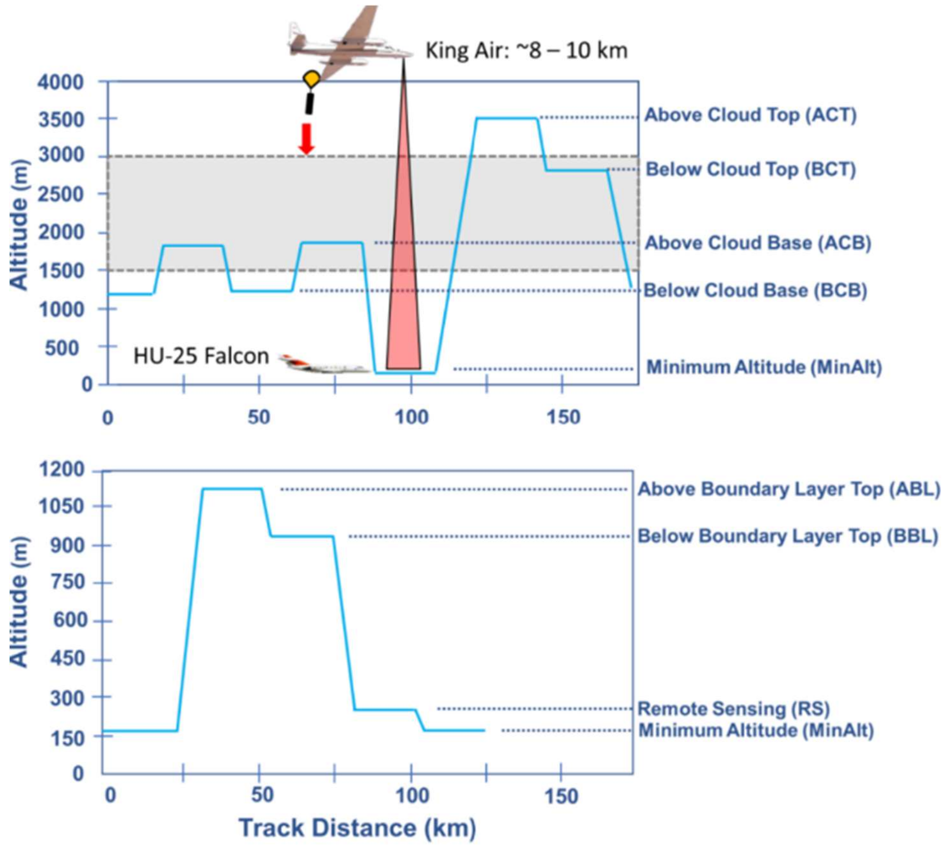

Figure 2 Flight ensemble schematics showing cloudy ensembles (top) and clear ensembles (bottom). All flight legs for cloudy and clear ensembles are shown, though we only utilize Below Cloud Base, Above Cloud Base, and Below Cloud Top in this study (Sorooshian et al., 2023).

The two aircraft utilized in this experiment were the NASA Langley Research Center's HU-25 Falcon and the King Air. The HU-25 Falcon, also referred to as the Falcon, was a lower-flying plane spanning a range of 3000 km and an altitude between 0.15 km to 3 km. The aircraft traveled at an average airspeed of 130 m/s with an average total flight duration of 4 hours. Among the instruments used in our study were the Diode Laser Hygrometer (DLH), two-dimensional Stereo probe (2-DS), Cloud Droplet Probe (CDP), and Cloud-Aerosol Spectrometer (CAS); all of which were externally mounted on the Falcon. Other instruments aboard the Falcon, though not utilized in this study, were a Fast Cloud Droplet Probe (FCDP), AC3-Cloud collector, CVI, and an isokinetic aerosol inlet. The main purpose of the Falcon’s flights was to collect in-situ observations of trace gas measurements (Ozone, CO, CO_2, H_2O), CCN, aerosol microphysics, aerosol composition, aerosol optical scattering and absorption, and hygroscopicity (Sorooshian et al., 2023). In opposition, the King Air flew at a higher altitude, above the Falcon, with an average altitude of 8 to 10 km above the surface and a maximum range of 1500 km. Similar to the Falcon, the average airspeed was 120 m/s, with the same average flight duration of 4 hours. Unlike the Falcon, the King Air carried a High Spectral Resolution Lidar (HSRL-2), Research Scanning Polarimeter (RSP), Dropsonde (AVAPS), and RSP support electronics, though this study only uses images from the HSRL-2 to remove cases with significant dust. In total, there were 152 joint aircraft missions, meaning both aircraft flew together for one to two missions per day. This totaled about 600 hours per aircraft throughout the campaign. For this study, we focused on flights from January to June 2022, for a total of 75 flights on 43 different dates. The dataset for 2022 was the most comprehensive year from 2020-2022, as 2020 and 2021 were impacted by COVID-19 (Sorooshian et al., 2023). Details about the flights from 2022 are displayed in Table 2. Flight paths for the chosen dates and flights in this study are shown in Figure S1 using lidar images from the HSRL-2. Aircrafts left NASA Langley Research Center (LARC) off the coast of Virginia and flew east over the Western Atlantic Ocean before returning to land for January - June 2020 and 2021. In 2022, January - May flight paths remained the same, but during June, flights were focused on collecting data around Bermuda.

Month 2022	**Total # of days**	**Total # of flights**	**Primary flight location**	**ACTIVATE deployment #**	**Season**
January	8	15	WNAO	5	Winter
February	9	15	WNAO	5	Winter
March	9	16	WNAO	5	Winter
May	8	12	WNAO	6	Summer
June	11	17	Bermuda	6	Summer

Table 2 Total flight statistics for all flights used in the study from January-June 2022. This includes the deployment number, the primary flight location (Western North Atlantic Ocean (WNAO)), and the season in which data was collected (Sorooshian et al., 2023).

There were two defined categories of “ensembles” for the Falcon; cloud-free and cloudy for each flight. These ensembles were comprised of different “legs” (Dadashazar et al., 2022; Sorooshian et al., 2023). These legs were flown in the following order: below the cloud base (BCB), above the cloud base (ACB), minimum altitude at 0.15 km (MinAlt), above the cloud top (ACT), below the cloud top (BCT), and then descended back to BCB height. Minimum altitude legs, below boundary layer top legs, and above boundary layer top legs with a descent back to minimum altitude were cloud-free ensembles. Cloudy ensembles consisted of minimum flying altitude, below cloud base, above cloud base, above cloud top, below cloud top, and a descent back to minimum altitude. The relevant leg lengths, ensemble lengths, and leg altitudes are summarized in Table 3. The detailed ensemble flight paths are shown in Figure 2. The systematic repetition of these flight ensembles has resulted in an extensive amount of data (Dadashazar et al., 2022). This study focuses on BCB, ACB, and BCT legs in cloud-free air to analyze coarse-mode sea salt aerosols. We did not utilize any “clear-sky” ensembles due to lack of sufficient data (Figure 3). There are more cloudy ensemble legs to work with, so we apply rigid filtering criteria to remove any cloud contamination and create “clear-sky” conditions from cloudy ensembles.

Leg type	**Leg altitude range**	**Average leg altitude**
Below cloud base (BCB)	0.110km - 2.46km	0.702km
Above cloud base (ACB)	0.125km - 2.72km	0.967km
Below cloud top (BCT)	0.11km - 5.48km	1.38km

Table 3 Flight leg statistics for the 4 relevant flight legs types in this study. Statistics detail the average leg time and average altitude where leg data was collected. Each leg length was, on average, 3.3 minutes long (Dadashazar et al., 2022; Sorooshian et al., 2023)

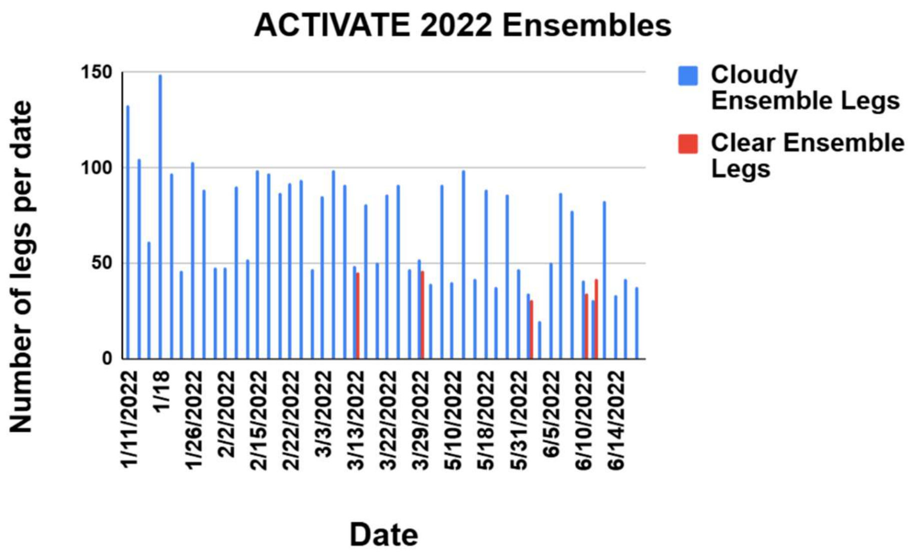

Figure 3 The amount of legs flown for different ensembles organized by date. There are more cloudy ensemble legs, and therefore more data to work with, than clear ensemble legs.

iii. Western Atlantic Meteorology

Previous field studies have also focused on characterizing the marine boundary layer, examining vertical profiles of clouds and aerosols, aerosol-cloud interactions, and examining various aerosol properties, like CCN. Past notable field work that analyzed the impact of GCCN on precipitation included seeding marine stratocumulus clouds with a salt powder solution off the coast of central California in 2011 as part of the Eastern Pacific Emitted Aerosol Cloud Experiment (EPEACE) (Jung et al., 2015). During these experiments, the emitted salt powder was intended to create GCCN concentrations of about 10^{-2} to 10^{-4} cm^{-3} for an average emitted particle size of 5 um diameter released at a rate of 5 x 10^{9} particles per second from a fluidized bed delivery system. Like ACTIVATE, EPEACE used in-situ probes, including a Cloud Aerosol Spectrometer which is relevant to our study, to gather observations. Results from Jung et al., 2015 indicated faster drizzle formation as a result of increased collision-coalescence after artificial seeding, which are consistent with what we know thus far of coarse mode sea salt aerosol-cloud interactions (Feingold 1999; Jensen and Lee 2008; Jensen and Nugent 2017). But, while the

EPEACE study (Jung et al., 2015) provided valuable insight into this relationship, its conclusions are limited by its narrow temporal and meteorological scope—being confined to a single summer case study flight. In other words, although EPEACE demonstrated that enhanced GCCN concentrations can lead to faster drizzle formation, the findings cannot be broadly generalized to other seasons or varying atmospheric conditions. These limitations underscore the need for a more comprehensive investigation. ACTIVATE, with its multi-season, multi-flight design, and extensive in-situ and remote sensing observations, offers the opportunity to examine the impacts of GCCN on precipitation across diverse conditions.

The Western North Atlantic Ocean, which is the focus for observations for June 2022, is unique in its atmospheric aerosol and chemical composition (Corral et al., 2021). This location contributes significantly to marine aerosol fluxes, like coarse mode sea salt aerosol to the MBL, which also happens to be the most dominant source of aerosol optical depth and boundary layer aerosol composition during ACTIVATE (Liu et al., 2023). However, in addition to natural marine emissions, the WNAO is strongly influenced by long-range transport of aerosols from both continental sources. The study region lies within a key pathway for pollutant transport from the North American East Coast, as well as the transatlantic transport of Saharan dust. These aerosol influxes are largely driven by large-scale meteorological features such as trade winds, midlatitude cyclones, and synoptic-scale frontal systems (Corral et al., 2021; Painemal et al., 2021). Dust transport over the Atlantic peaks during the summer months when large plumes from the Sahara are blown westward. Aerosol optical depth over the WNAO is primarily driven by sulfate and sea salt, which are the main contributors to total AOD, while black carbon and organic carbon exhibit smaller but seasonally varying influences (Painemal et al., 2021). An example of dust transport paths and North American pollutant transport over the study region is shown in Figure 4 (Sorooshian et al, 2020) and the seasonal variability and relative contributions of various aerosol species over the ACTIVATE study region are illustrated in Figure 5 (Painemal et al., 2021), which highlights the dominant aerosol types, including sulfate, sea salt, organic carbon, black carbon, and dust, along with their annual cycles. On the North American side of the Atlantic, midlatitude cyclones drive boundary layer outflow toward the Western Atlantic via northwesterly winds behind cold fronts.

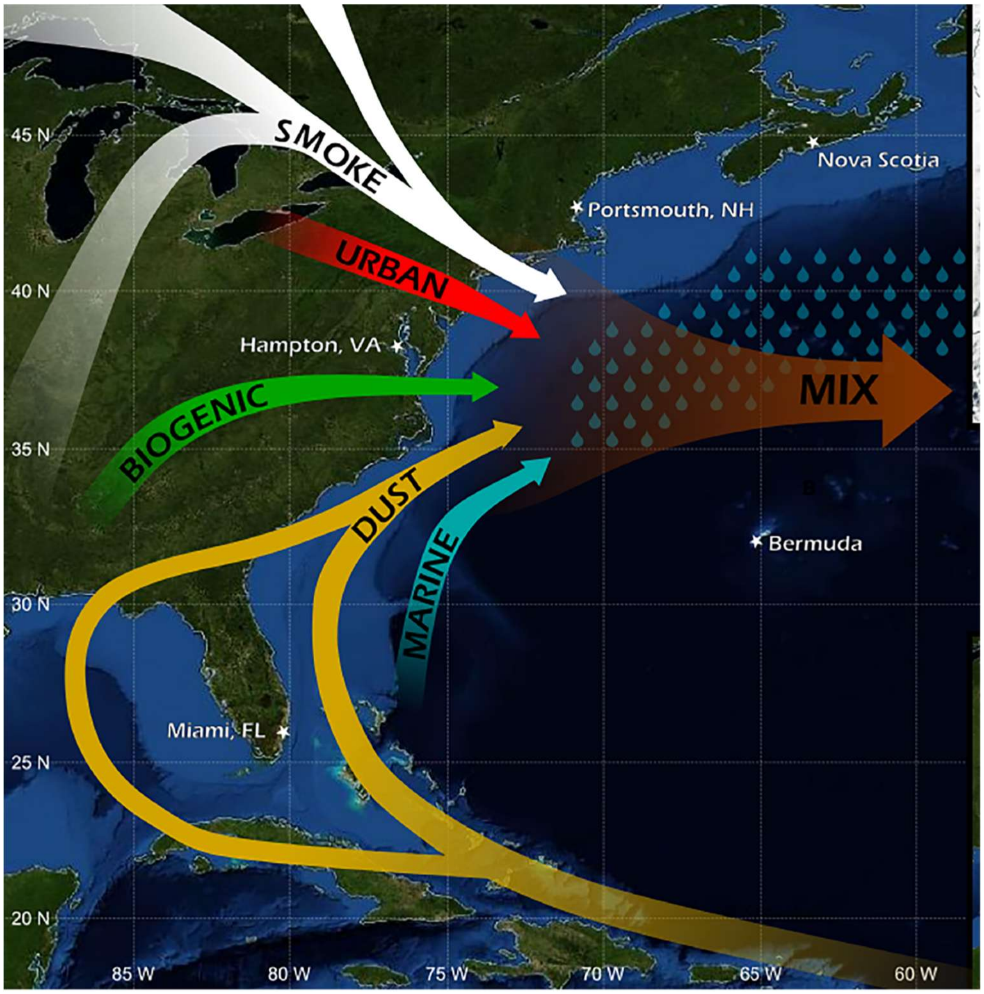

Figure 4 Dust and pollution transport pathways over the North Western Atlantic Ocean study region (Sorooshian et al., 2020).

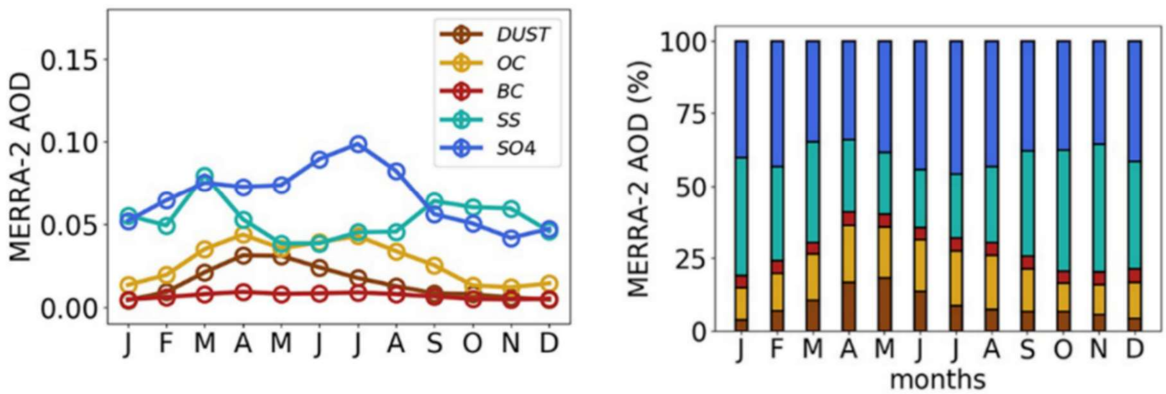

Figure 5 Seasonal variability of aerosols over the Western North Atlantic Ocean based on MERRA-2 reanalysis, showing the annual cycle of aerosol optical depth for key aerosol species (left) and the relative monthly contributions of each aerosol type to total aerosol optical depth (right) (Painemal et al., 2021).

iv. Key features of clouds and aerosols over the Western Atlantic

The study region is also characterized by strong seasonal variations in cloud cover, with low clouds being most prevalent in winter and least frequent in summer. These low clouds, which are primarily marine boundary layer clouds, are closely linked to postfrontal cold-air advection, leading to increased cloud cover during winter months. In contrast, high clouds are more dominant in summer, influenced by warm sea surface temperatures, tropical convection, and increased upper-level humidity (Painemal et al., 2021). The WNAO also exhibits a diverse range of cloud morphological regimes, consisting of a high frequency of shallow cumulus and stratocumulus clouds. Shallow cumulus clouds are most common over the warm waters of the Gulf Stream, particularly in winter, where they frequently form behind cold fronts as part of cold-air outbreaks. In contrast, stratocumulus clouds are more prevalent over the colder waters to the northeast (Painemal et al., 2021). Figure 6 (Painemal et al., 2021) illustrates the spatial variability of these two dominant cloud types. To summarize, this seasonal variability influences aerosol concentrations and their interactions with clouds, further making the Atlantic an ideal region for studying these processes.

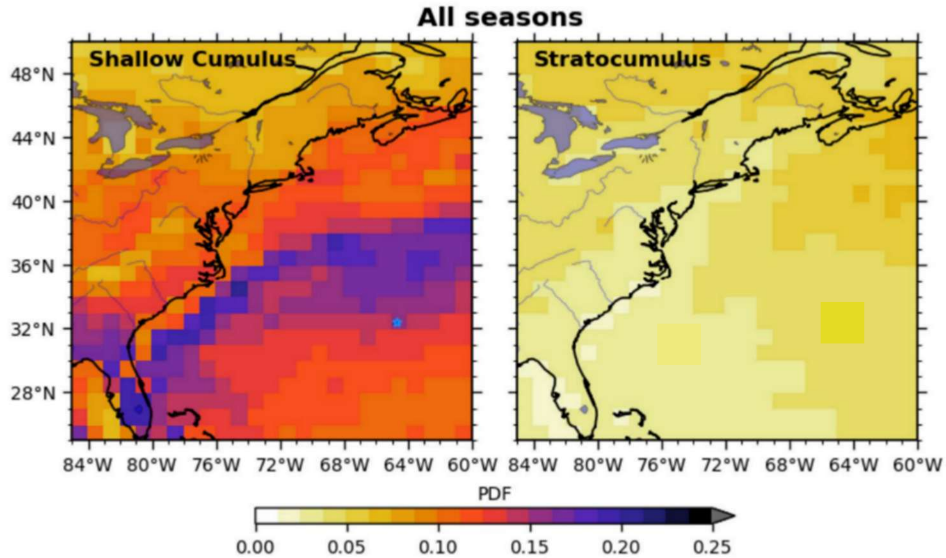

Figure 6 The spatial distribution and frequency of shallow cumulus (left) and stratocumulus cloud types (right) during all seasons over the study region (Painemal et al., 2021).

B. Instrumentation

This section provides an overview of the primary instruments used in this study to investigate GCCN size distributions. These include the Cloud-Aerosol Spectrometer (CAS) the Cloud Droplet Probe (CDP), and the SPEC 2-dimensional Stereo Probe (2D-S) and were selected for their ability to measure certain droplet size distributions, concentrations, and characteristics critical for understanding cloud-aerosol interactions and precipitation processes. The following subsections describe each instrument in detail, including their measurement capabilities, operating principles, and relevance to this research. All measurements for each instrument are taken at ambient relative humidity and reported seconds after midnight and relevant instrument details are provided in Table 4.

It is important to note that both the CAS and CDP are optical instruments, and their particle sizing depends on assumptions about the refractive index of measured particles. The CDP measures only forward-scattered light, while the CAS collects both forward and backscattered signals. According to the instrument manuals, a refractive index of 1.33 is assumed (Droplet Measurement Technologies 2017, 2018). Although some studies recommend applying additional refractive index corrections, particularly for sea salt aerosols, which in dry form have higher refractive indices (~1.5; Clarke et al., 2003; Bi et al., 2017), the CAS and CDP data used here have already been corrected. Because these measurements are taken at ambient relative humidity, the aerosols are hydrated at the time of sizing, which reduces the mismatch; hydrated sea salt aerosols typically have refractive indices between ~1.34 and 1.42 depending on RH (Bi et al., 2017). Still, if any residual bias existed in the hydrated sizing, it would propagate through the hygroscopic growth correction applied to derive dry diameters. This potential uncertainty is expected to be small but is acknowledged in the interpretation of the largest droplet sizes.

Instrument	Parameters measured	Size range (μm)	Reference
DMT cloud droplet probe (CDP)	Aerosol and cloud droplet number concentration, liquid water content, and effective radius/variance	2–50	Lance 2012
DMT cloud and aerosol spectrometer (CAS)	Aerosol and cloud droplet number concentration, liquid water content, and effective radius/variance	0.5–50	Baumgardner et al., 2001
SPEC Inc. two-dimensional stereo (2D-S) vertical and horizontal arms	Cloud number size distribution for liquid, ice, and total; liquid and ice water content; ice flag; effective diameter for liquid, ice, and total; and median volume diameter for liquid and total	29–1465	Kirschler et al., 2023
Diode laser hygrometer (DLH)	Water vapor	N/A	Diskin et al. (2002)

Table 4 Instruments and size ranges used to create size distributions in this study

i. Cloud Aerosol Spectrometer (CAS)

The measured particle size range for the CAS is 0.5 μm hydrated diameter to 50 μm diameter, making this instrument optimal for GCCN with dry diameters greater than 1 μm, but can still collect data on particles in the smaller size range that the CDP does not capture. Similar to the CDP, integrated aerosol and cloud droplet number distributions are reported in units of dN/dlogD for thirty-size range bins. Liquid water content is reported in g m^3, and effective radius, and effective variance are reported in μm.

The CAS samples at an area of 0.25 mm^2 and with a frequency of 1 Hz (Sorooshian et al., 2023). Measurements were made by the NASA Langley Aerosol Research Group.

ii. Cloud Droplet Probe (CDP)

The CDP (Droplet Measurement Technologies, DMT 2025) is the most common instrument used when analyzing cloud-aerosol interactions. Measurements were made by the NASA Langley Aerosol Research Group (LARGE). The sample area experimentally measured by DMT was 0.323 mm^2 (Sorooshian et al., 2023). It also has a high temporal sampling resolution, between 1 and 20 Hz, which varies based on deployment. For example, 2020 sampling resolution at 1 Hz proved difficult to distinguish cloud shape, so flights in 2021 and 2022 were sampled at 20 Hz. For the flights used in this study, sampling was at 20 Hz, but we aggregate data to 1 Hz for consistency with the CAS (more details in the Methods section). We do not measure cloud droplets with the CDP. We use this instrument only in cloud-free conditions. The CDP uses single-particle light scattering, and samples at a particle size range of 2 μm hydrated diameter to 50 μm diameter, which samples much of the SSA coarse mode. Integrated aerosol and cloud droplet numbers are reported units per cm^3 across thirty-size range bins somewhat unevenly but approximately logarithmically distributed across diameter D. Liquid water content is reported in g m^{-3}, and effective radius and effective variance are reported in μm (Moore et al., 2022). Effective radius is the ratio of the third to the second moment of a droplet size distribution and effective variance is the spread in that size distribution (Daum and Liu 2005).

iii. 2-dimensional Stereo probe (2-DS)

Finally, we use a SPEC Inc. 2D-S horizontal arm in this study to pull precipitation data and larger particle sizes not captured by the CAS or the CDP. This instrument produces shadow images of single particles using 128 photodiodes of 11.4 μm (Lawson et al., 2019; Kirschler et al., 2022). The 2D-S measures liquid water content, ice water content, and total, liquid, and ice number concentrations in m^{-3}. The ice and liquid median volume diameters represent the sizes at which half of the total particle volume (and therefore mass) is contributed by droplets smaller than that threshold and half by larger droplets. Particle size ranges from 28.5 μm diameter to 1464.90 μm diameter across 126 total size bins, optimal for analyzing large precipitation drops. Measurements were collected by a German research team (DLR).

3. Methods and Results

a. Size-resolved aerosol concentration profiles

To characterize aerosol concentration above the Western Atlantic, we analyze size-resolved hydrated (ambient) aerosol distributions derived from CAS observations from below the cloud base to within the cloud. We use 1 Hz data for 75 flights on 43 different dates from January to June 2022. Each 1 Hz observation is taken from a typical 3 minute below cloud base flight leg. Given the binning structure of recorded data within the CAS instrument's data files, we select measurements corresponding to haze particles ranging from 2.5 μm diameter to 50 μm diameter covering 18 bins (bins 12–29 out of 30 available size bins) ranging from 0.5 μm to 50 μm diameter in total. Clear-sky conditions for accurate interpretation of the size distributions are identified by strictly filtering for liquid water content below 0.0025 g m^{-3} from the CAS to remove contamination from cloud droplets and total precipitation number concentration below 100 particles m^{-3}, as measured by a two-dimensional stereo probe. These thresholds ensure the hydrated size distributions measure haze droplets without cloud or drizzle droplet interference. An average concentration is computed across the leg for each bin to provide a mean haze size distribution for the leg (cm^{-3} μm^{-1}). The size distribution can then be used to estimate concentrations and other moments. The analysis yielded 460 below cloud base legs with a mean altitude of 701 m, a mean 10 m wind speed of 5.3 m s^{-1} (Section 3b), and mean total flight leg concentration of 0.56 cm^{-3} where the concentration for each size bin is plotted against the central diameter (μm) of each of the 18 bins. The full range of wind speeds is provided later in the section and the full range for altitudes is provided in Figure S2 for these legs. 90 of the resulting 460 haze particle size distributions (for simplicity) as a function of deliquesced diameter are shown in section Figure 7.

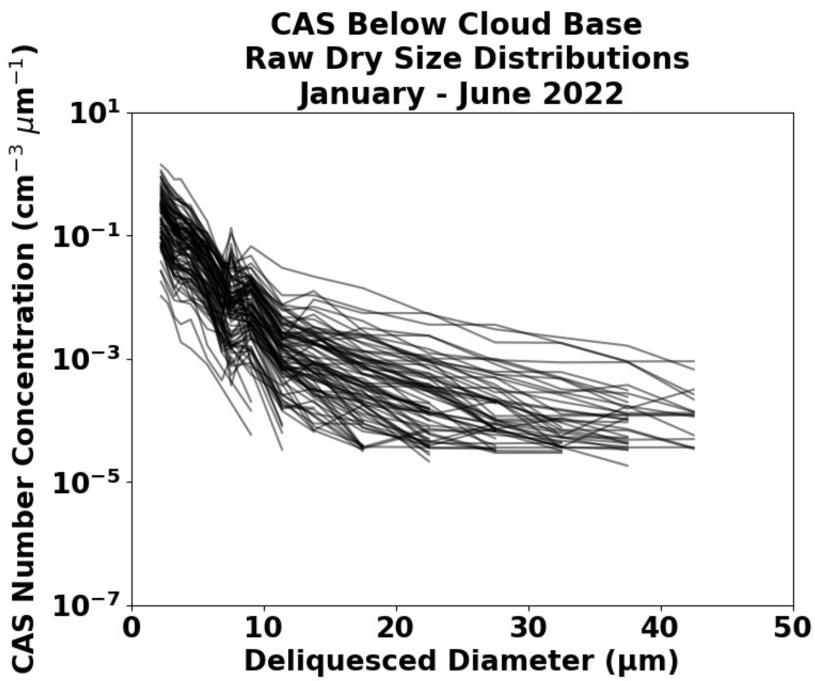

Figure 7 A selection of 90 of the total computed 460 hydrated size distributions. We only show 90 distributions because 460 distributions on the same figure obscures the form of the distributions.

We also estimate dry salt aerosol size distributions from our hydrated measurements. To convert an ambient (hydrated) size distribution to a dry salt size distribution, we need the average flight leg's relative humidity and the corresponding salt particle "growth factor" (Seinfeld and Pandis 2006). The hygroscopic growth factor quantifies how aerosol particles absorb moisture from the atmosphere, leading to an increase in their size. This growth factor is defined as the ratio of ambient (hydrated) diameter to its dry diameter. It is a function of relative humidity only, not of diameter (Tang 1996; Jensen 2008).

$$g(RH) = \frac{r_{hydrated}}{r_{dry}} \tag{1}$$

As RH increases, particles absorb more water, leading to a higher growth factor. We obtain an average relative humidity for each below cloud base flight leg from the Diode Laser Hygrometer aboard the HU-25 Falcon (Diskin et al., 2022). We derive our growth factor from the simplified form of the Köhler equation, where we assume the Kelvin term is negligible for supermicron droplets:

$$RH = 1 - \frac{b}{r^3} \tag{2}$$

The relative humidity for sea spray aerosols is equal to Equation 3 (Jensen 2008; Ackerman and Nugent 2023):

$$RH = \frac{1}{1 - RH} \tag{3}$$

The hygroscopicity parameter for sea spray aerosols is denoted by kappa, “k”, which can be substituted for the Raoult term in Equation 2, resulting in the following growth factor in Equation 4. We used a kappa value of 1.7.

$$g(RH) = \left[\frac{k}{(1-RH)}\right]^{\frac{1}{3}} \tag{4}$$

We convert our ambient size distributions to dry size distributions:

$$r_{dry} = \frac{r_{hydrated}}{g(RH)} \tag{5}$$

The growth factor is entirely dependent on relative humidity, so it varies across all flight legs. The average growth factor across all flight legs in this study is 2.19. Distributions of the growth factor across all flight legs are shown in Figure 8.

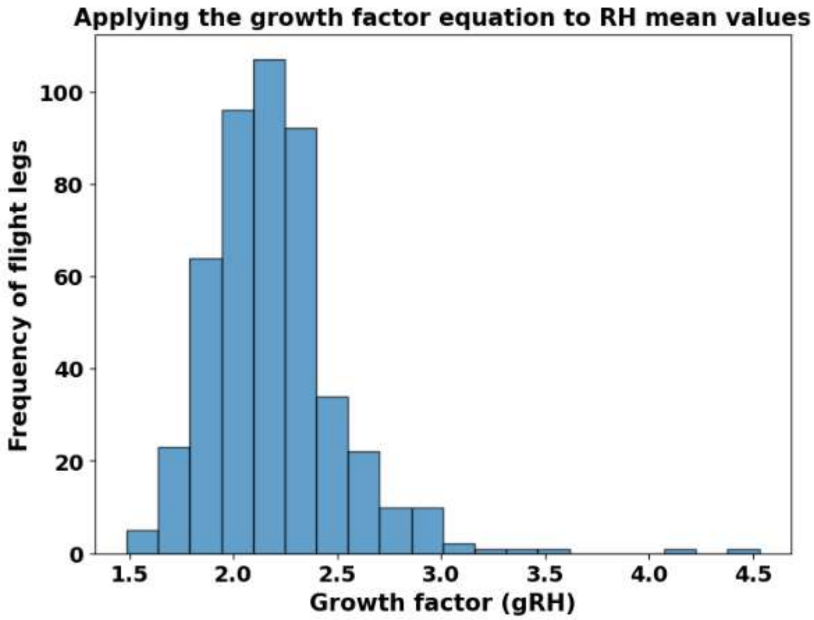

Figure 8 The distribution of the growth factor (Equation 4, where kappa is 1.7), dependent on flight leg RH, used to correct ambient size distributions to dry size distributions across all below cloud base flight legs.

Applying Equation 5 results in a set of size distributions reflecting dry aerosol conditions. We show an example of the conversion from an ambient distribution to a dry distribution for a single flight leg in March.

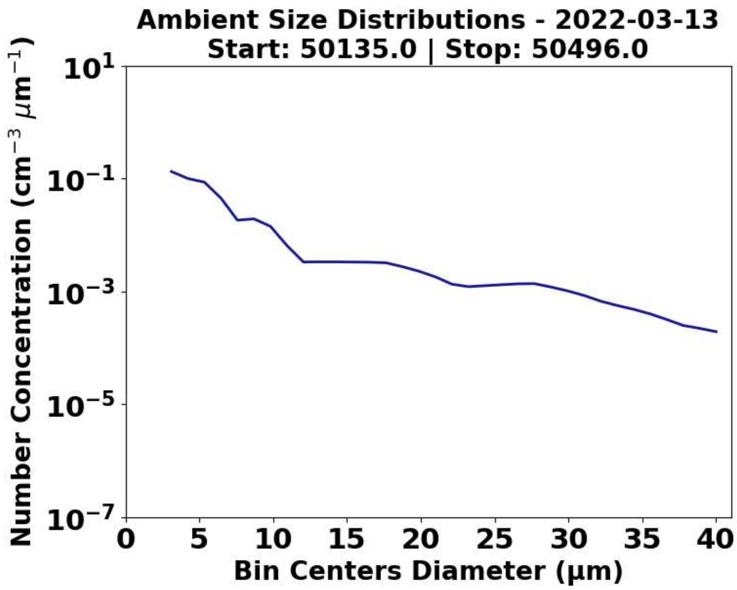

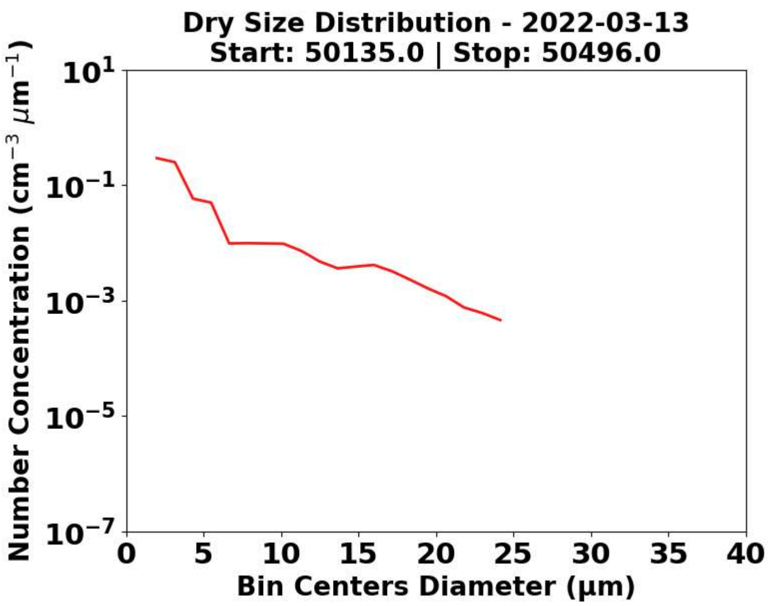

Figure 9 The hydrated size distribution (upper) and the converted dry size distribution (lower).

Figure 10 depicts the same 90 size distributions shown in Figure 7, converted to dry, as 460 distributions are too dense for a single figure. However, all future analysis is computed using all distributions.

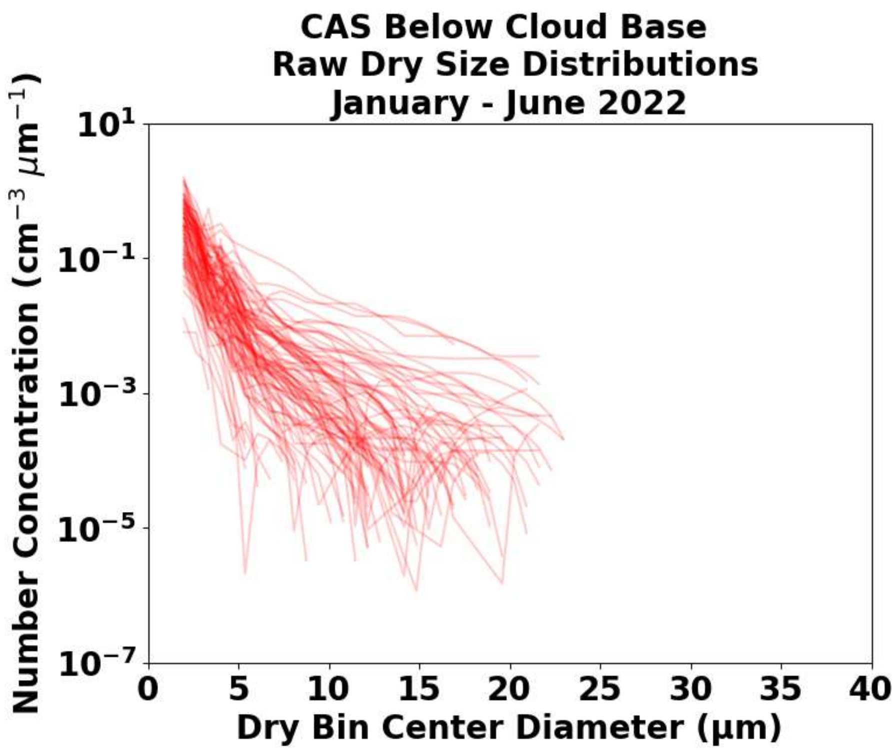

Figure 10 90 distributions showing the typical behavior of dry aerosol size distributions from our dataset.

Observing Figure 10, our distributions exhibit a flattening trend toward the larger particle sizes rather than a steep decline that would be consistent with the nature of GCCN size distributions represented in other studies (Cólon-Robles et al., 2006). Flight legs sampled in this study averaged a sample time of 180 seconds, which is a relatively short sample time, meaning a small number of particles are likely to be observed within this time frame as opposed to a sample time on the order of 30 minutes to an hour. Low particle counts can result in “shot noise” and a flattening of the size distributions at certain size ranges. One possible method to work with shot noise is to concatenate a set number of individual 3-minute legs into “superlegs” so as to create legs with longer sampling time. However, we cannot do this. The number of legs logged per flight per day varies extremely (between 2-16 legs) and concatenating across multiple flights or days would risk introducing additional variability due to changing meteorological and flight conditions Instead, to smooth shot noise, we fit an equation of exponential decay to each size distribution, shows how the number concentration of dry aerosols decreases as particle size increases:

$$n(D_{dry}) = N_{0,\,dry} e^{-\frac{D_{dry}}{D_{e,\,dry}}} \tag{6}$$

$N_{0,\,dry}$ represents the intercept and $D_{e,dry}$ represents the e-folding diameter, which controls how quickly the concentration decreases with size. We overlay the exponential fits with each size distribution from Figure 10, resulting in Figure 11. However, at the larger particle size range, the exponential fits do not agree very well with the distributions.

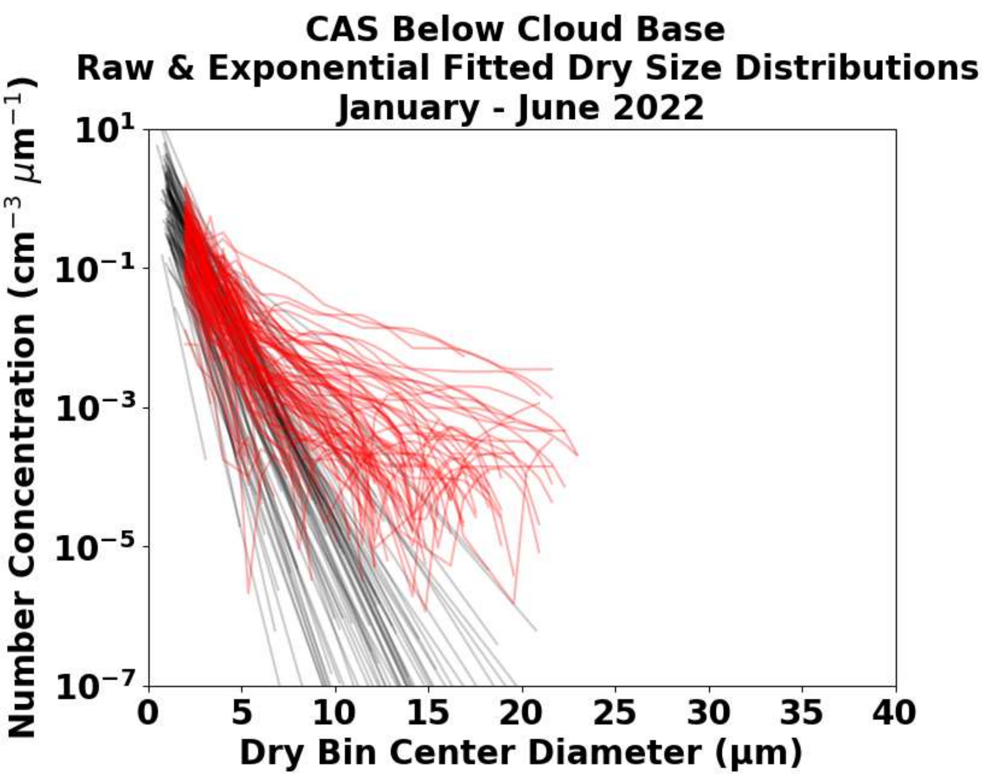

Figure 11 The exponential fits to each distribution (Figure 10) compared with the raw distributions.

To work with these distributions, given their high particle counting error, we estimate the relative error for each distribution as a function of particle counts:

$$relative\ error\ = \frac{\sqrt{N_{counts}}}{N_{counts}} \tag{7}$$

The relative counting error for all distributions is shown in Figure 12, where the red line depicts where the dry size distributions reach a counting error of 1 or 100%. This occurs for many distributions between 5-10 μm diameter meaning the relative error past the 10 μm range is high and results in a lot of noise.

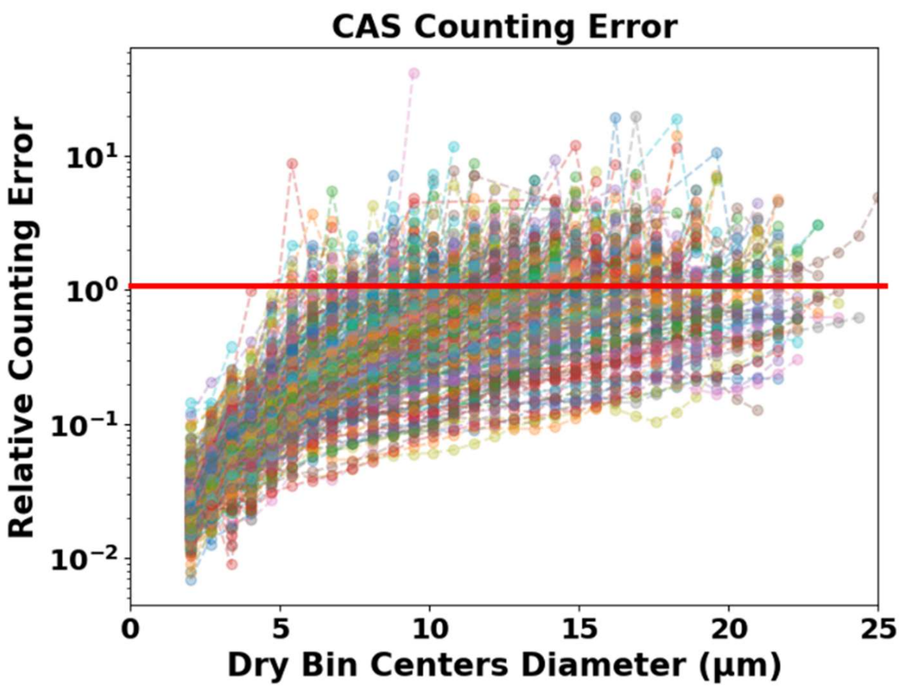

Figure 12 The relative counting error for the CAS as a function of dry diameter for all size distributions.

This noise, and the reason we see our exponential fits diverge from our raw data at the larger particle size range (Figure 11), is a result of these high counting errors at our larger particle size range. To accommodate this noise at the larger size range, we adjust our exponential fits from Figure 11 to only fit each distribution to 10 μm diameter. The adjusted 10 μm diameter fits overlaid with the distributions from Figure 10 are depicted in Figure 13.

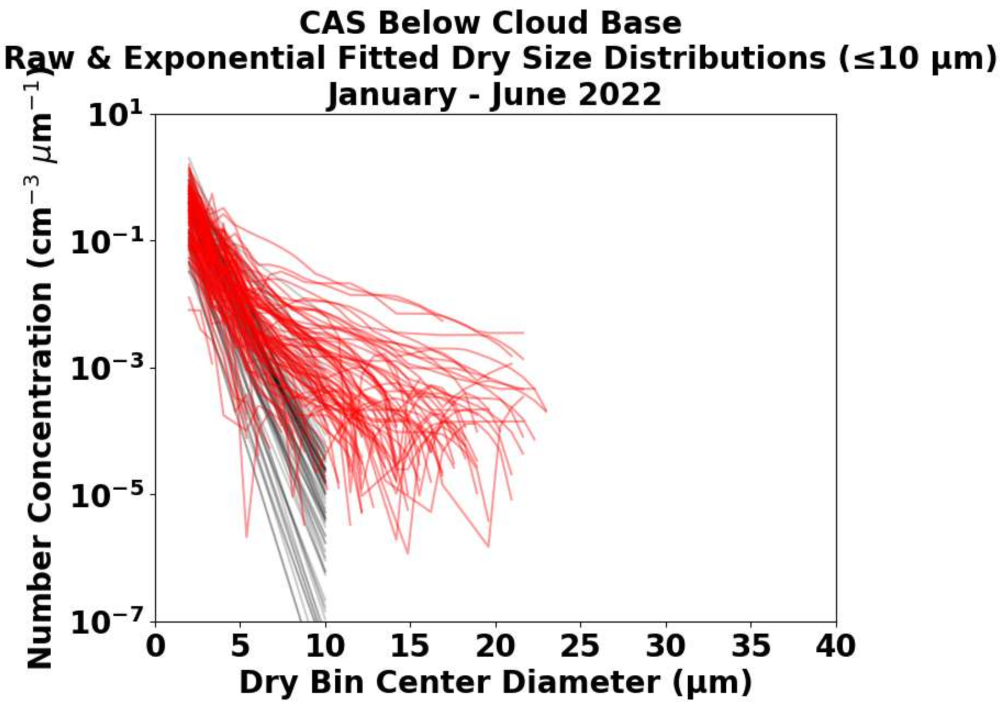

Figure 13 The adjusted 10 μm diameter exponential fits for each dry size distribution.

These final fitted distributions serve as the foundation for subsequent analysis with wind speed influence on coarse-mode aerosol concentrations.

To contextualize our dry distributions, we compare our average CAS dry distribution, taken linearly, (Figure 14) with Colón-Robles et al. (2006, their Figure 2c). While their measurements were conducted in the tropical Atlantic, rather than the Western Atlantic, the general shape of their distributions is a reasonable check to ensure our calculated distributions are within expected bounds. This comparison can help confirm that our methodology produces physically reasonable results, even if it is not a direct validation, given the differing conditions of Colón-Robles et al. 2006 and ACTIVATE. Figure 14 depicts the dry size distribution for individual flight legs as a function of dry diameter using observations from a Giant Nucleus Impactor (GNI), taken from Colón-Robles et al. (2006). Unlike the CAS, which directly sample haze particles in ambient air in real time as they pass through the instrument's sample volume, the GNI collects airborne aerosol particles on glass slides, for post-flight humidification and optical analysis (Colón-Robles et al., 2006). One thing to note is the GNI has a huge sample volume at 10 liters per second with 10s exposure intervals (Jensen et al., 2020). The CAS measures about 25 $cm^3\ s^{-1}$, or about 5 liters for 180 seconds of sampling. The GNI sample volume is ~20 times bigger. Thus, the noise floor of the GNI is much lower, causing the distributions for the GNI to extend much further into the larger diameter range. If we overlay our average CAS dry distribution (red) with Colón-Robles et al. 2006 (black), we see the distributions agree very well, despite the cloud-aerosol spectrometer instrument counting errors (Figure 12). The consistency in distribution shape suggests that our methodology produces physically reasonable results within the expected range for sea spray aerosol distributions.

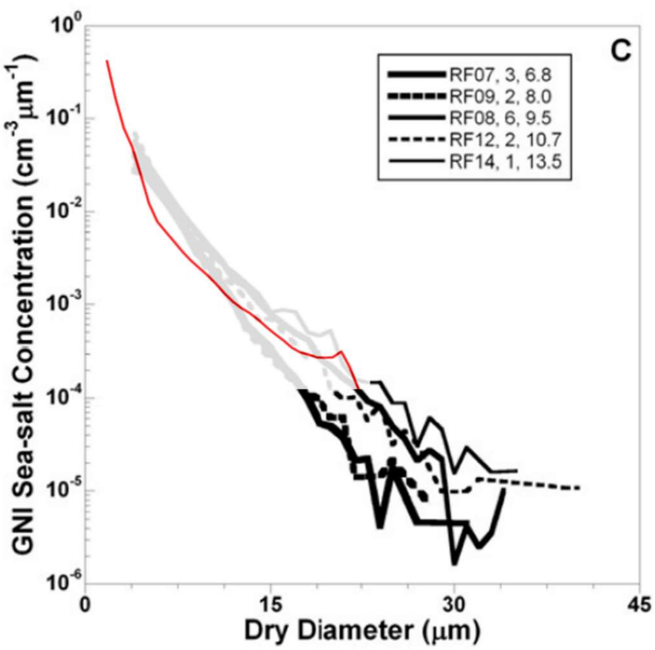

Figure 14 The average CAS dry size distribution (red) compared with individual dry size distributions from Colón-Robles et al. 2006 (black) using observations from a GNI.

b. Wind speed influence on coarse-mode aerosol concentrations

To contextualize the relationship between near-surface wind speed and coarse-mode aerosol size distributions, we compare our results to a previous observational study (Colón-Robles et al., 2006). This study has established key relationships between increasing wind speed and enhanced coarse mode sea spray aerosol production. While prior datasets were collected in different regions and using various measurement techniques (Lewis and Shwartz 2004, their Figure 22), they're general findings of increased concentration with increasing wind speed provide a useful reference for evaluating the robustness of our findings.

Since aircraft wind speed measurements are taken at varying altitudes above the ocean surface, we apply a logarithmic wind profile correction (Equation 8) to standardize all wind speeds to a reference height of 10 meters (Stull 1988). Our mean wind speed across all of our below-cloud base legs is 5.13 m s^{-1} with a standard deviation of 2.65 m s^{-1}. The distribution of estimated 10 m wind speeds are shown in Figure 15.

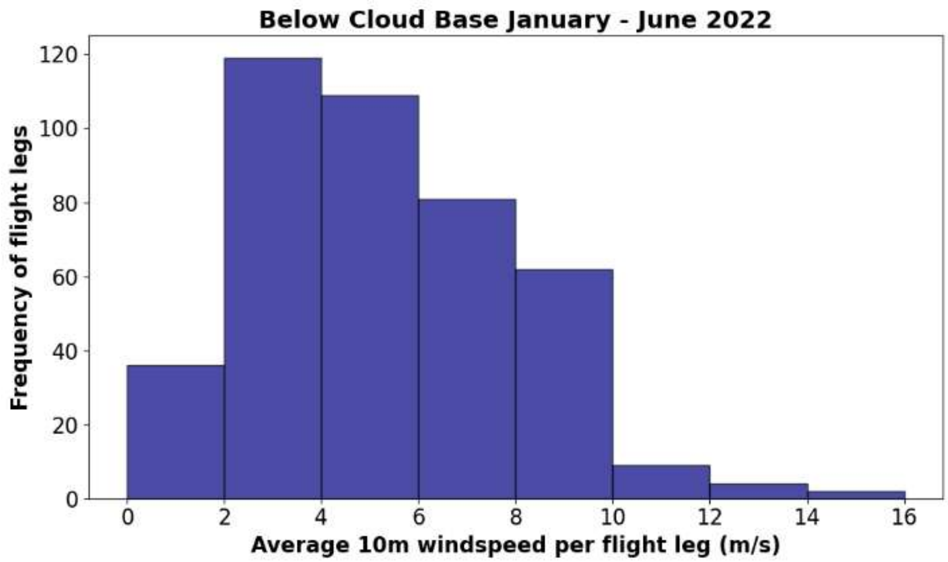

Figure 15 Distributions of leg averaged wind speed at 10 m.

$$U_{10} = U_z \times \left[\frac{\log(10m \ \times \ Z_0)}{\log{(Z \ \times \ Z_0)}}\right] \tag{8}$$

Here, U_{10} is the wind speed at 10 m above the surface (m s^{-1}), U_z is the average flight leg wind speed (m s^{-1}), Z_0 is the roughness length above the ocean surface set to 0.02 m for the open ocean (Peña and Gryning 2008), and Z is the average flight leg altitude (m).

We compare measurements from both the CAS and the CDP in our wind speed analysis to assess the robustness of our results, given the variability in past studies regarding the influence of wind speed on concentration. Using two instruments with the same size range (>2 μm) us to evaluate whether the observed relationships hold consistently across different instruments. The CDP instruments size binning structure differs for measured hydrated particles from the CAS. The full size range of the CDP is 2.0 μm to 50 μm diameter across thirty size bins. Here, we utilize all thirty bins to construct our ambient and dry size distributions. Furthermore, for the flights used in this study, CDP sampling took place at 20 Hz, but we aggregate data to 1 Hz for consistency with the CAS. The relationship between total concentration and wind speed for both instruments is shown in Figure 16. The CDP and the CAS both show extremely low correlations between wind speed and concentration for leg averaged distributions. One notable difference is that the CDP has a few outlier concentrations that are much higher than those observed with the CAS. The weak correlation between wind speed and concentration is a robust feature across our flight legs in ACTIVATE, regardless of the instrument used to collect observations.

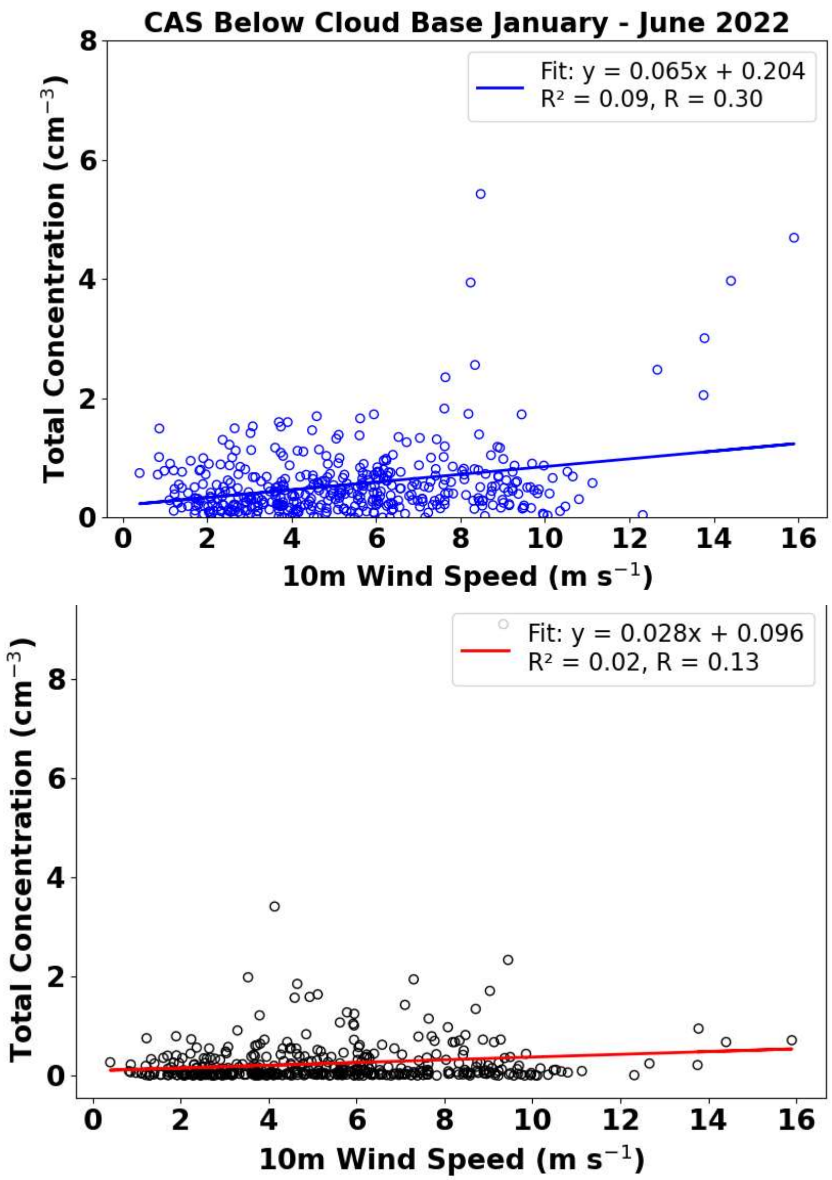

Figure 16 CAS (upper) and CDP (lower) total haze particle concentration as a function of average 10 m wind speed. A correlation coefficient is calculated for both the CAS and CDP relationships. The CAS shows a very weak R= 0.30 and the CDP, an even weaker R= 0.13

We compare our CAS and CDP relationships with Colón-Robles et al. 2006 to assess the relative strength of our correlations. While this is not a direct comparison, given that Colón-Robles et al. used different instruments, sampled in the trade winds over the western Atlantic, and operated under different meteorological conditions, it serves as a useful reference point. Rather than a test of validity, this comparison functions as a sanity check to contextualize our observations within the broader range of studies examining the relationship between wind speed and aerosol concentration.

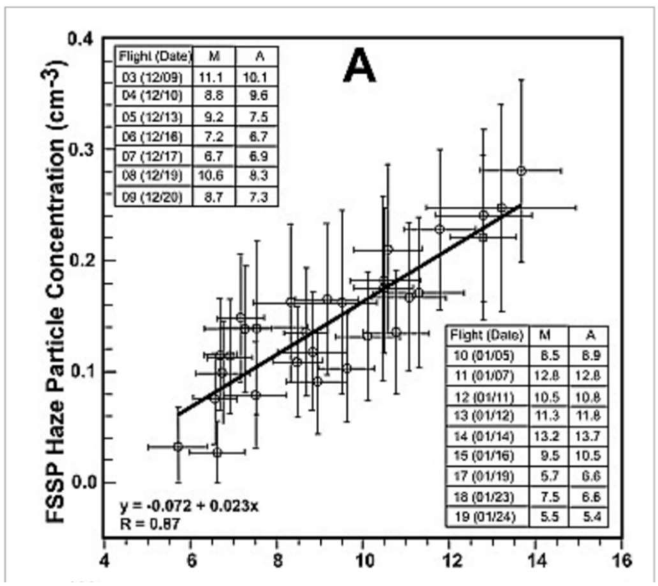

Figure 17 Figure 1a from Colón-Robles et al., 2006 depicting a strong positive relationship between total FSSP haze particle concentration (cm^{-3}) and average wind speed ($m\ s^{-1}$) with an R value of 0.87 for 19 flights.

The study by Colón-Robles et al. 2006 found a strong positive relationship between wind speed and total droplet concentration. As the wind speed goes from 6 $m\ s^{-1}$ to 13 $m\ s^{-1}$, the concentration increases from 0.08 to 0.25, which is relatively similar to the CAS and CDP observations shown in Figure 16 from ACTIVATE. compared to CAS and CDP observations from ACTIVATE. This study was based on 30-minute flight legs during the Rain in Shallow Cumulus over the Ocean (RICO) campaign (2004–2005) over the trade winds in the western Atlantic. In contrast, ACTIVATE flights used 3-minute sampling legs, which likely introduced higher particle counting errors. The longer sampling time in RICO may have reduced these errors, making the wind speed–concentration relationship more apparent than in our measurements. To optimize our data given the short sampling time, we categorized flight legs into six wind speed bins that capture the full range of observed wind speeds. These bins were designed to represent the overall wind speed range in our dataset, 0 $m\ s^{-1}$ to 16 $m\ s^{-1}$. Figure 18 shows the probability density function (PDF) of 10 m wind speeds, with red dashed lines marking the boundaries of the six wind speed bins. The selected wind speed ranges are 0–2.5, 2.5–3.5, 3.5-5, 5-7, 7-9, and >9 m s^{-1}. Initial k-means clustering suggested two bins, but this was deemed insufficient to represent the full distribution, particularly given the concentration of data around 5 m s^{-1}. Instead, we manually selected six bins to balance coverage across the wind speed range while maintaining reasonable bin widths. We tried our subsequent analysis with four bins and five bins (not shown) and concluded that our analysis with six wind speed bins was robust.

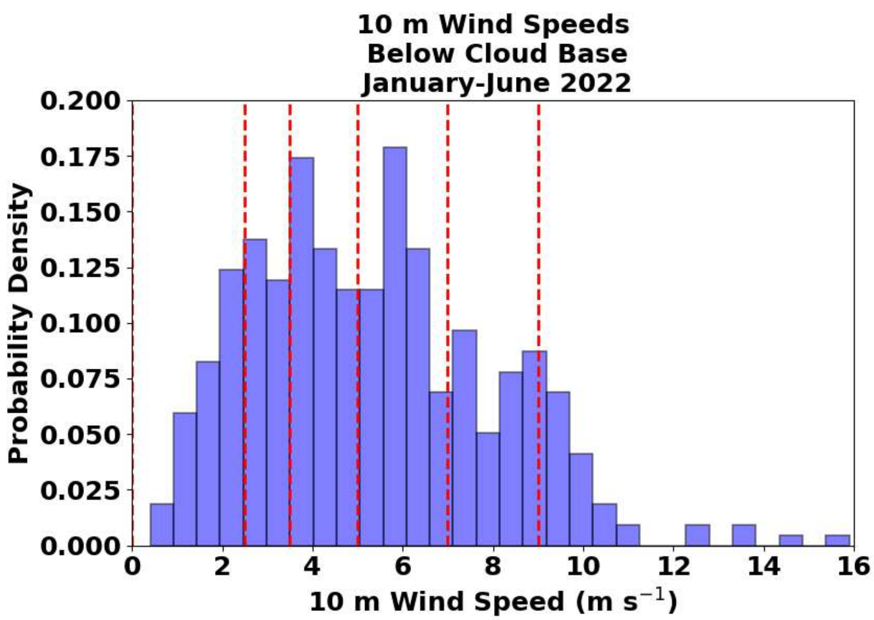

Figure 18 A probability density function of 10 m wind speed showing 6 bins of wind speeds 0–2.5, 2.5–3.5, 3.5-5, 5-7, 7-9, and >9 m s^{-1}.

There are several flight legs with no recorded wind speed in the data files. This is possibly due to an instrument recording error. For each flight leg associated with an average 10 m wind speed, we average our dry size distributions together, resulting in one average size distribution for each of the six wind speed ranges. Following the same size distribution creation procedures as the CAS (Section 3a), we incorporate comparisons with the CDP. The six binned size distributions are presented in Figure 19 for each instrument with standard error bars for each average distribution. The standard error quantifies the uncertainty in the average value due to the finite number of legs within each wind speed range. Standard error is calculated as:

$$SE = \frac{\sigma}{\sqrt{N}} \tag{9}$$

Where σ represents the standard deviation in concentration in each wind speed bin and N represents the number of distributions averaged into each bin.

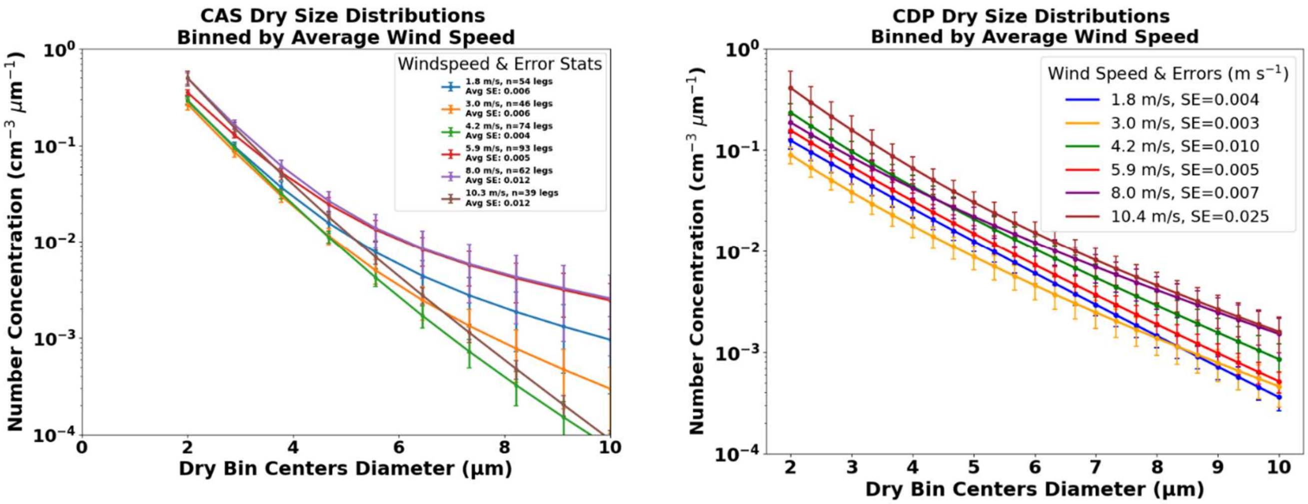

Figure 19 CAS (left) and CDP (right) dry size distributions binned by average wind speed, with colors representing different wind speed bins: blue (0–2.5 ms^{-1}), orange (2.5-3.5 ms^{-1}), green (3.5-5 ms^{-1}), red (5-7 ms^{-1}), purple (7-9 ms^{-1}), and brown (>9 ms^{-1}). Standard error bars indicate the standard error after averaging across flight legs within each bin.

The CAS and CDP dry size distributions show distinct trends across wind speed bins, with separation in number concentration for smaller diameters (2–4 μm) and larger diameters (>6 μm) where error bars do not overlap, indicating a significant effect of wind speed. However, in the intermediate range (4–6 μm), the error bars overlap across most bins in both CAS and CDP, suggesting less distinguishable differences in number concentration between wind speed categories. Ideally, based on the strong influence of wind speed on concentration from previous studies (Colón-Robles et al. 2006; Lewis and Schwartz 2004), we would expect to see an increase in concentration with increasing wind speed bins. However, this pattern is not entirely consistent across our averaged distributions. For the CAS, the highest concentrations are observed at our third and second highest wind speed bins (5.9 ms^{1} red; 8 ms^{1}, purple) rather than at the highest wind speed bin (10.3 ms^{1}, brown), suggesting a peak at intermediate wind speeds rather than a continuous increase. In contrast, the CDP exhibits a slightly clearer trend, where the highest wind speed bin (10.4 ms[1], brown), generally shows higher concentrations. However, the lower-level wind speed bin (4.2 ms[1], green) yields a higher concentration than the 5.9 ms^{-1} (red) rather than showing a distinct increase in concentration as we increase in wind speed, as we might expect. Regardless of these differences between instrument distributions, for the most part, at higher wind speeds, there exists higher coarse-mode aerosol concentration.

To further analyze these results by computing a line of best fit between the total concentration for each wind speed distribution and the average wind speed in each corresponding bin for both instruments (Figure 20).

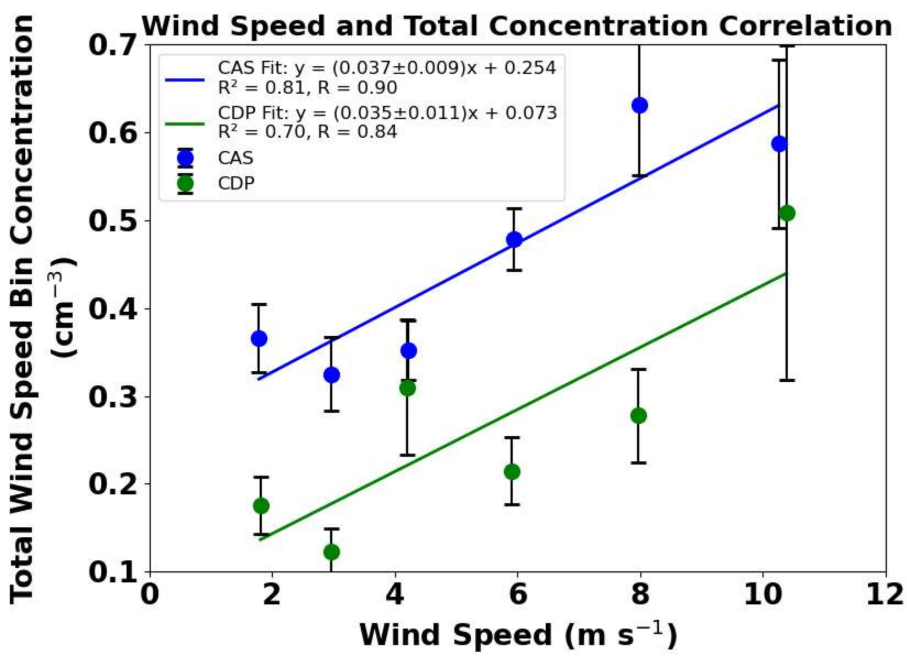

Figure 20 The relationship between total wind speed bin concentration and average 10 m wind speed for the CAS (blue) and the CDP (green) with lines of best fit. R =0.90 for the CAS and R =0.84 for the CDP. Both coefficients reveal positive trends.

According to Figure 20, both the CAS and CDP show a clear relationship between wind speed and total aerosol concentration when binned by wind speed, revealing positive trends across different wind regimes. As average wind speed increases, total concentration also increases. The relationship with wind speed is stronger when multiple distributions are averaged together, rather than analyzing individual flight legs as a function of wind speed (Figure 16). The short flight leg sample time of 180 seconds obscures any possible trend between wind speed and concentration, making analysis with individual flight legs difficult. This positive relationship seen in Figure 20 is more comparable to Colón-Robles et al. 2006, with both the CDP and CAS R-values (0.90 and 0.84 respectively) very similar to the R value in Figure 17.

We also compute a line of best fit between the total mass of coarse-mode aerosol for each wind speed distribution and the average wind speed in each corresponding bin for both instruments (Figure 21).

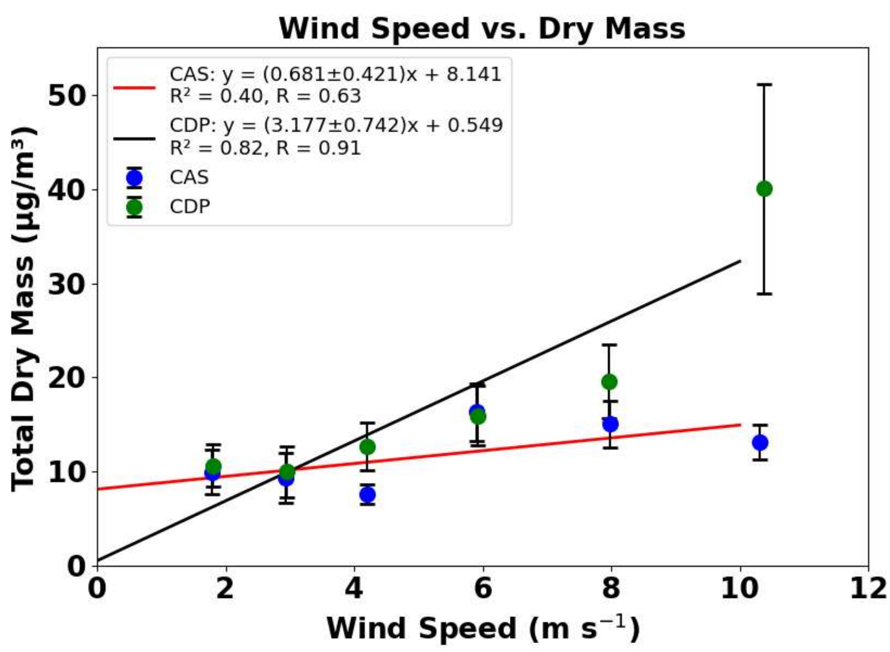

Figure 21 The relationship between total wind speed bin mass and average 10 m wind speed for the CAS (blue) and the CDP (green) with a line of best fit (red). R =0.63 for the CAS and R =0.91 for the CDP. Both coefficients reveal positive trends.

Mass dependence on wind speed is noisier than for total number concentration. This is expected because mass is controlled by the larger particles which are occur more infrequently. The correlation between mass and wind speed is weaker than the correlation between the total concentration and wind speed. However, the trends for mass and wind speed for each instrument are still positive and stronger than the noisy trend between wind speed and individual flight legs.

The time it takes GCCN to fall out of the atmosphere is a function of terminal velocity and altitude of the sub cloud layer. Terminal velocity is dependent on the square of the size of the GCCN, so larger particles with more mass fall out of the atmosphere more quickly than smaller particles with less mass. Furthermore, wind speed at the surface tends to remain relatively steady over about 12 hours (Daoud et al., 2003), which is roughly the GCCN fall out timescale for GCCN with ambient sizes of about 10 μm dry diameter. Smaller particles (< 1μm) last for several days in the atmosphere, making them less correlated with instantaneous wind speed (Ackerman et al., 2025). It is possible the mass measured by the CDP is more strongly correlated with wind speed because the particles measured may be larger than those measured by the CAS (Figure 20).

c. Modeling GCCN influence on precipitation

To assess the potential role of giant cloud condensation nuclei (GCCN) in drizzle formation, we use a particle-based condensational and collisional growth model to simulate cloud droplet evolution from the near-surface to cloud top (Bartmann et al., 2022). The Super Droplet Method (SDM), which is applied within our model, tracks groups of droplets representative of individual droplets. It does not have numerical diffusion or advection (Shima 2009). We are using a 1D model configuration for PySDM that is described more fully in Shipway and Hill (2011). A column of air is lifted (details are provided below), resulting in saturation and condensational growth, followed by collision-coalescence. This allows a calculation of how the aerosol particles grow as they are lofted above the cloud base, allowing us to determine their influence on cloud microphysics and precipitation initiation. This Lagrangian-based model tracks the growth of any specified dry aerosol size distribution, which may include a supermicron (GCCN) distribution. We establish a single lognormal accumulation mode size distribution that is somewhat representative of typical marine conditions (e.g. Fig 1 from Fitzgerald 1991) to act as a control distribution without the presence of GCCN. This distribution mode is centered at 0.24 μm diameter. The standard deviation of the log of the diameter is 1.4, which is typical of marine accumulation mode distribution widths (see e.g., Table 3 in Heintzenberg et al. 2000). The number concentration is set to 100 cm^{-3}, which is typical of relatively clean marine conditions (Heintzenberg et al., 2000). We choose three representative exponential fits from Section 3a to act as three case studies to represent the GCCN distributions, allowing us to assess the response of precipitation to varying GCCN concentrations and masses. Particles in the accumulation mode and coarse mode are assumed to be hygroscopic (hygroscopicity parameter "kappa" of 0.7, Petters and Kreidenweis 2008). Variations in hygroscopicity within the range of values in the marine boundary layer do not yield very different results. The simulation assumes an initially constant relative humidity profile that is just below saturation (99%) up to 740 m, above which relative humidity decreases rapidly to mimic boundary layer conditions. Similarly, the potential temperature is held constant at 297 K below 740 m before increasing sharply above 740 m to suppress condensation above this altitude. The atmospheric pressure follows a hydrostatic profile. The updraft velocity m s^{-1} increases steadily in time and then decreases again to zero, with the following function:

$$\omega_{(t)} = \omega_0 \sin\left(\frac{\pi t}{T}\right) \tag{10}$$

There is no downdraft in this simulation. ω_0 represents the maximum updraft speed (0.2 m s^{-1}) and this peak ascent rate is reached at time t=T/2, with T, fixed at 1000 seconds. Liquid water path (LWP) after lifting is defined as 464 g m^{-2}, which is representative of the thicker parts of marine boundary layer clouds that are likely to be precipitating (Rémillard et al., 2012). As the model runs, particles remain within the column, where the updraft initiates their growth via condensation upon reaching supersaturation. They continue growing for 1000 seconds, after which the updraft ceases and drops sediment out. Both condensation and collision coalescence can take place throughout and after the ascent (Barr 2025). The total simulation length is 1 hour, selected for computational efficiency, and the vertical resolution is 50 m (particle positions are not discretized into height bins, but the number of super droplets is specified to be the same in each height bin). To assess the variability in precipitation response, we conduct 30 simulations for each case study, as well as the accumulation mode distribution, due to the stochastic nature of the model. The collisions of the super droplets within this model are handled stochastically. The super droplets that collide in one simulation might not collide in another simulation (Shima 2009). Therefore, running an adequate number of simulations is essential. Our goal in using this model is to see to what the effect of GCCN is on precipitation both in terms of mass of GCCN and total concentration of GCCN. We do this only for distributions from one instrument (CAS) for computational efficiency. However, Figure 21 shows us that the masses for the CAS and CDP are quite different. So, eventually it might be beneficial to run CDP distributions through PySDM to compare with the results for the CAS.

We choose three case study GCCN dry size distributions to serve as model input against the accumulation mode control distribution. To choose these case studies, we extract the slope and intercept parameters (Figure 22) from 10 μm exponentially fitted dry size distributions (Section 3a). We also compute the total coarse-mode dry mass of sea salt (μg m^{-3}) of each GCCN size distribution (Equation 11) and overlay mass contours with our extracted exponential fit parameters (Figure 25). Coarse-mode dry GCCN mass M_{dry} is determined as:

$$M_{dry} = \frac{\pi}{6}\rho_s N_{0,dry} \int_{(D_{dry})_{min}=2\ \mu m}^{\infty} ({D_{dry}}^3) e^{-\frac{D_{dry}}{D_{e,dry}}} dD_{dry} \tag{11}$$

The density of sea salt, ρ_s, is 2200 kg m^{-3}, M_{dry} is the total dry mass concentration per flight leg (expressed in units of μg m^{-3}), $N_{0,dry}$ is the dry intercept, $(D_{dry})_{min}$ is the minimum dry diameter, D_{dry}

is the dry diameter (μm), and $D_{e,dry}$ is the e-folding diameter previously extracted from the exponential fit to the dry size distributions (section 3a). We integrate to infinity (rather than 10 due to our exponential fits in Section 3a) because the difference in including mass from below 10 μm or including all mass is negligible. The distribution of coarse-mode dry mass is shown in Figure 23. The mean mass is 10.25 µg m^{-3}.

We choose three distributions, each along different mass contours to ensure we have a range of mass values serving as model input. The distributions should be chosen to be representative of the overall behavior of our data so they cannot be outlier distributions, neither in terms of mass nor concentration. We also ensure two distributions have similar concentrations, but different decay rates. We choose these cases arbitrarily, and they are denoted by the red stars in Figure 22. The parameters for these

three distributions are listed in Table 5. We discover that each case study corresponds to three different flight dates in 2022. These are also listed in Table 5.

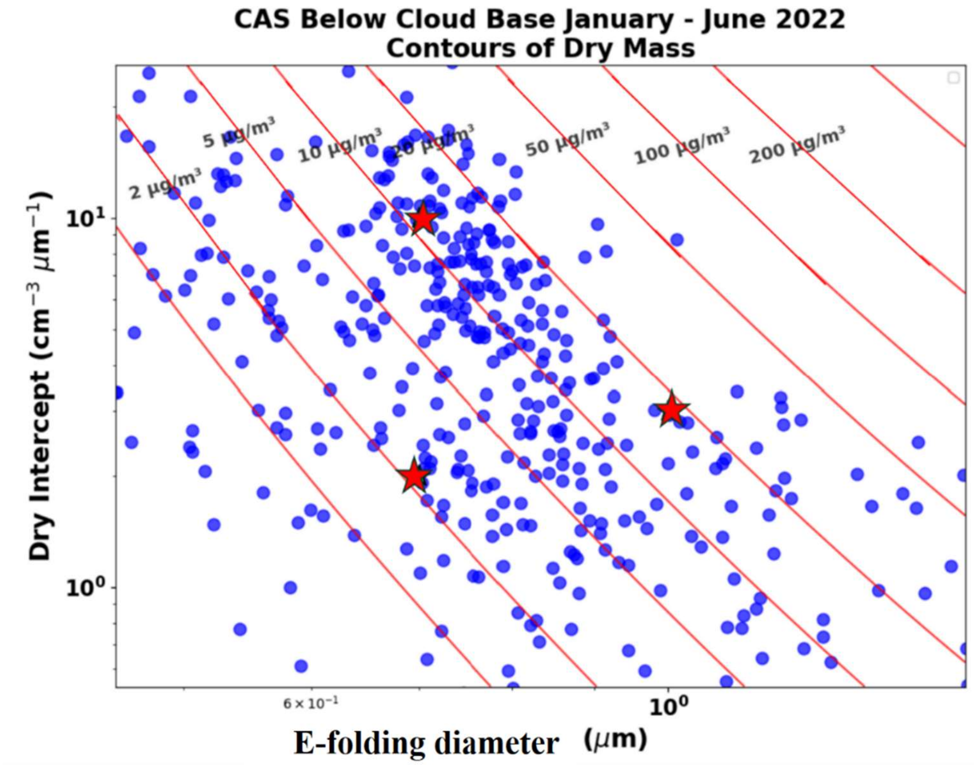

Figure 22 Slope and intercept values extracted from each fitted dry distribution with mass contours overlaid. The red stars show the three case study distributions

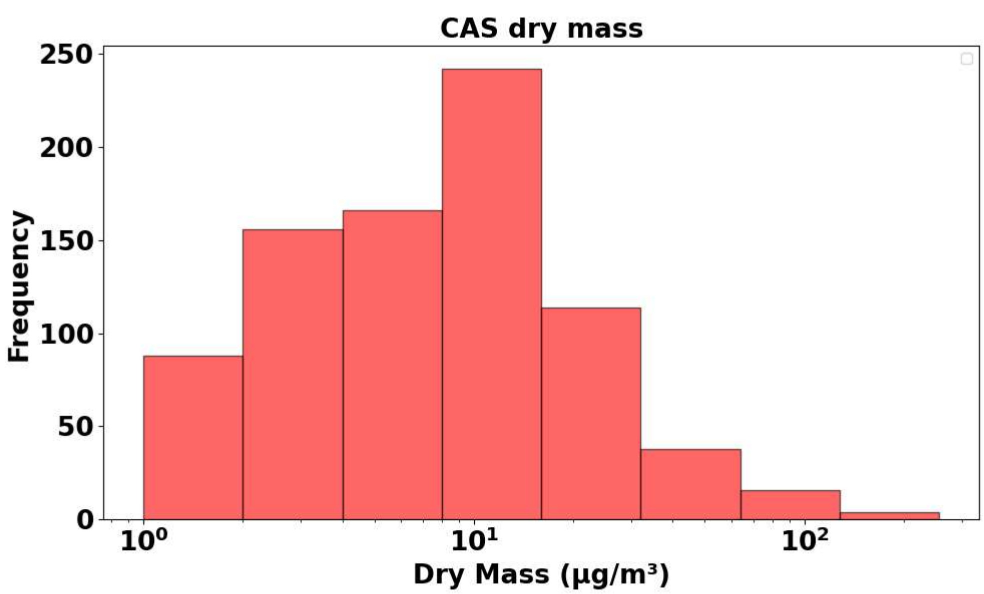

Figure 23 Distribution of total dry mass across all flight legs used in this study.

PySDM case studies

Case	Dry Slope (μm)	Dry Intercept (cm^{-3} μm^{-1})	Mass (μg m^{-3})	Total Concentration (cm^{-3})
January 26, 2022	0.7	10	11.0	1.0
January 24, 2022	0.7	2	3.0	0.2
February 3, 2022	1.2	3	37.0	0.8

Table 5 The three chosen case studies with corresponding flight date, slope and intercept parameters extracted from their exponential fits, total dry coarse-mode masses, and total concentrations.

To demonstrate the use of this model, we show a single time series of mean drizzle rate for surface precipitation across all 30 simulations for one of the dry GCCN case study distributions. Shaded regions represent the interquartile range around the mean drizzle rate to show the spread of drizzle rates across different simulations (Figure 24).

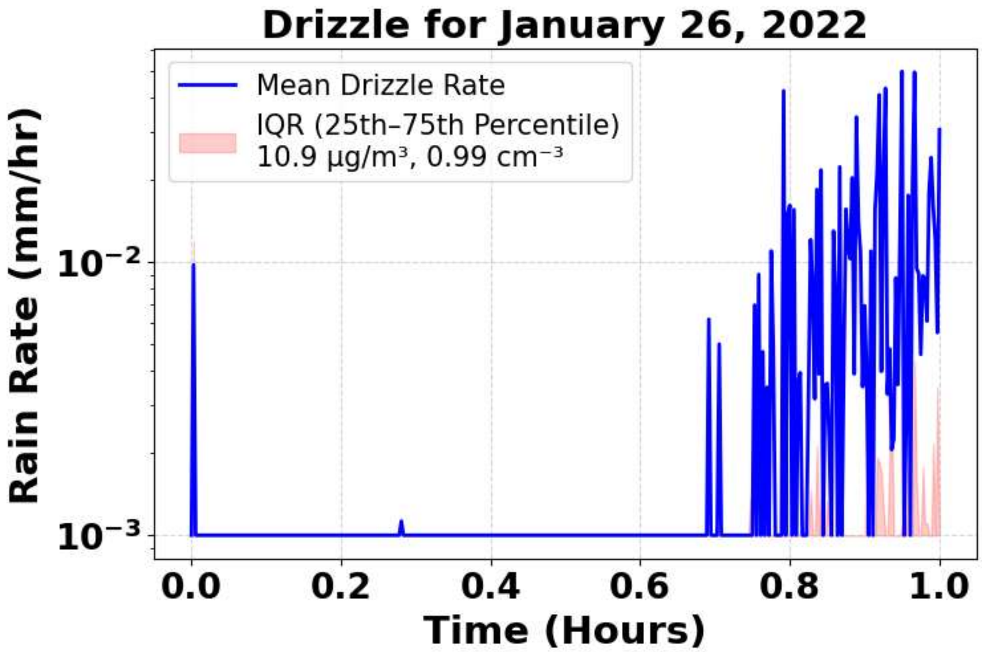

Figure 24 A time series of mean rain rate across all 30 simulations for one case study GCCN dry distribution (January 26, 2022). Standard deviation in rain rate is shaded.

We also show total rain rate over the hour-long simulation, across each of the 30 simulations, which we get by integrating over the time step of 10 s to get total accumulated rainfall for each simulation, as a function of mass and as a function of total concentration (Figure 25).

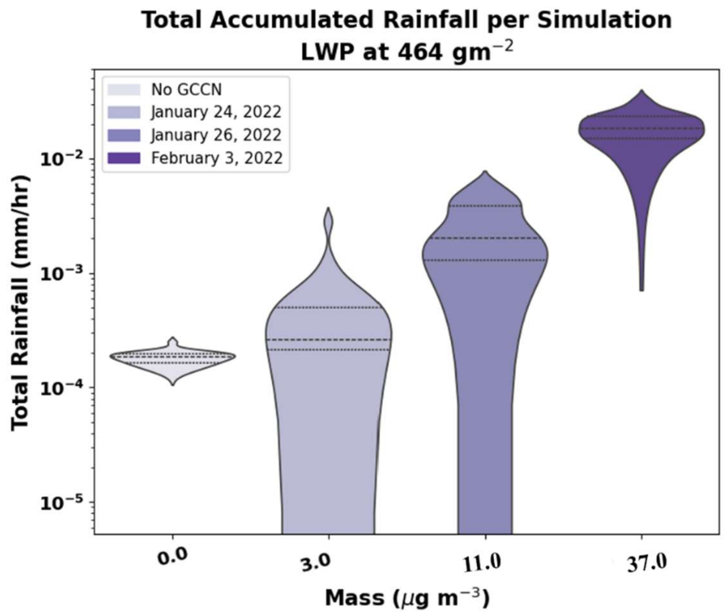

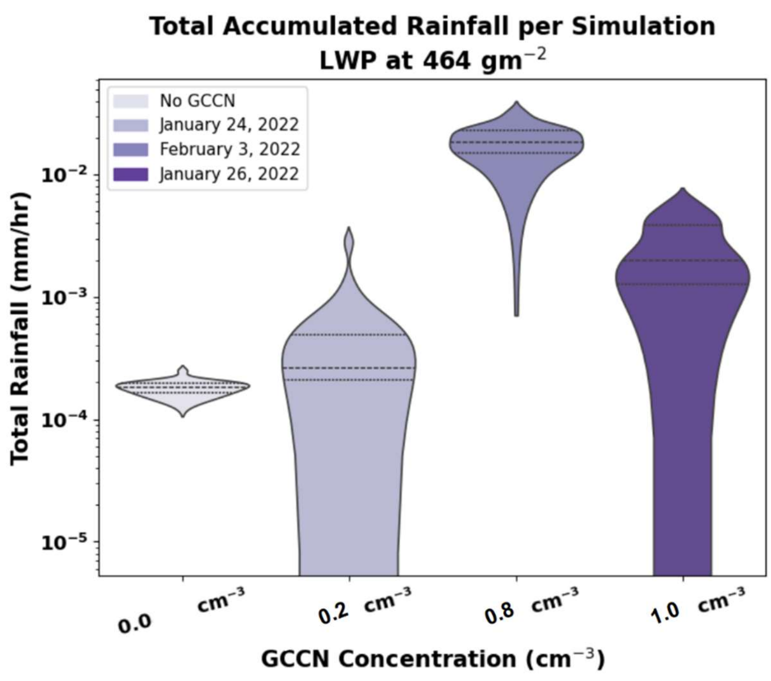

Figure 25 Total rainfall across all case studies for each simulation as a function of mass (upper) and as a function of GCCN concentration (lower) Dashed black line indicates the median drizzle rate and the dotted black lines indicate the 25th and 75th percentiles.

The relationship between total rainfall and mass of GCCN is monotonic; increasing mass leads to increases in drizzle. Concentration of GCCN does not display the same behavior as mass does with drizzle. The case study corresponding to the highest mass, February 3, 2022 ($M_{dry} = 37.0\ \mu g\ m^{-3}$) does not correspond to the highest concentration. Instead, the concentration for February 3, 2022 is 0.8 cm^{-3}, while the concentration for January 26, 2022, with a moderate mass ($M_{dry} = 11.0\ \mu g\ m^{-3}$) contains the largest concentration, 1.0 cm^{-3}. This suggests in the case of February 3, 2022, mass may be more dominant than concentration in influencing drizzle, a finding that warrants study in future work. In the control run where no GCCN are present, there is essentially no precipitation ($10^{-4}\ mm\ hr^{-1}$ is negligible). In comparison to the control, the presence of GCCN increases precipitation, regardless of mass or concentration. The mean and median drizzle rates for each GCCN case study are shown in Table 6. Since heavy drizzle is typically represented in mm/day, February 3 is the only meaningful case of precipitation. The drizzle rates for the other two cases are too small.

PySDM Drizzle Rate for 3 Cases of varying GCCN

	Dry Mass (μg/m³)	Total Concentration (cm⁻³)	Median Drizzle Rate (mm/hr)	Mean Drizzle Rate (mm/hr)
January 26, 2022	10.936	0.9967	0.002	0.0026
January 24, 2022	3.007	0.2284	0.0003	0.0005
February 3, 2022	36.85	0.8043	0.0187	0.0187

Table 6 The mean and median drizzle rates for each GCCN case study computed across all 30 simulations for each distribution. The highest mean and median drizzle rates correspond to the February 3, 2022 (high mass, moderate concentration).

d. GCCN influence on Rain Water Content

In addition to using PySDM, we analyze observational rainwater content (RWC) as a function of cloud droplet total concentration and liquid water content (LWC). ACTIVATE does not have aircraft remote sensors that provide liquid water path (LWP) measurements. Instead, we can use the total liquid water content (LWC), provided as the sum of the CAS (CWC, cloud water content) and the 2DS (RWC, precipitation water).

We compute a total in-cloud number concentration for every second of cloudy data for every flight leg, rather than using leg averages. To gather in-cloud data, we take measurements from above cloud base legs (ACB) and below cloud top legs (BCT). We merge the ACB and BCT legs into a unified dataset. We identify in-cloud conditions from the CAS using a CWC threshold >0.01 g m^{-3}, ensuring that only data points within the cloud are considered. For each second of flight data, we sum droplet concentrations from CAS bins corresponding to diameters from 2.5 μm to 50 μm (bins 12–29) for a cloud number concentration (N_c) every 1 Hz (cm^{-3}).

We also quantify raindrop number concentration (N_r) using 1 Hz measurements from the 2DS for precipitation data for each flight leg. We only identify precipitation during in-cloud conditions using the same CWC threshold of >0.01 g m^{-3}. For rain number concentration, we use bins from 62.70 μm to 1464.90 μm diameter (bins 6-128) from the 2DS. Rain drop concentration is computed by summing number concentrations across size bins in the same strategy as computing in-cloud number concentration.

We estimate rainwater content (g m^{-3}) for each second of data by computing the total liquid water mass associated with precipitation-sized droplets.

$$RWC = \frac{\pi}{6} \times \rho_w \sum_{i=6}^{128} N \times D^3 \times dD \tag{12}$$

The density of water, ρ_w is calculated as 1000 g m^{-3}, N is the droplet concentration in bin i, and D is the bin center. We then sum the cloud droplet number concentration (N_c) and the rain droplet number concentration (N_r) to get a total in-cloud number concentration (N_t cm^{-3})
following:

$$N_t = N_c + N_r \tag{13}$$

We find N_r to be much less than N_c so equation 13 simplifies to $N_t = N_c$ within a fraction of a percent. Similarly, CWC and RWC are summed to compute the total liquid water content (g m^{-3}) per second.

$$LWC = RWC + CWC \tag{14}$$

To analyze the fractional contribution of precipitation within the cloud, we compute the percentage ratio of rainwater to total condensate:

$$\frac{RWC}{LWC} \times 100 \tag{15}$$

To generate examine RWC as a function of total LWC and total concentration (Figure 26), we bin the total number concentration and LWC into logarithmically spaced bins (4x4 bins in each dimension) to capture observed variability. We take the mean RWC and LWC in each bin and compute the average RWC/LWC ratio of each bin following equation 15. The percentage RWC/LWC ratio (Fig. 26) is darker red when indicating higher precipitation fractions and darker blue to indicate lower precipitation contributions. Regions with no data are masked in gray. The mean number concentration over all cloudy data is 125 cm^{-3} and the mean LWC is 0.1 g m^{-3}. Precipitation appears to be controlled by a higher LWC and lower total concentration, as indicated by the warmer colors.

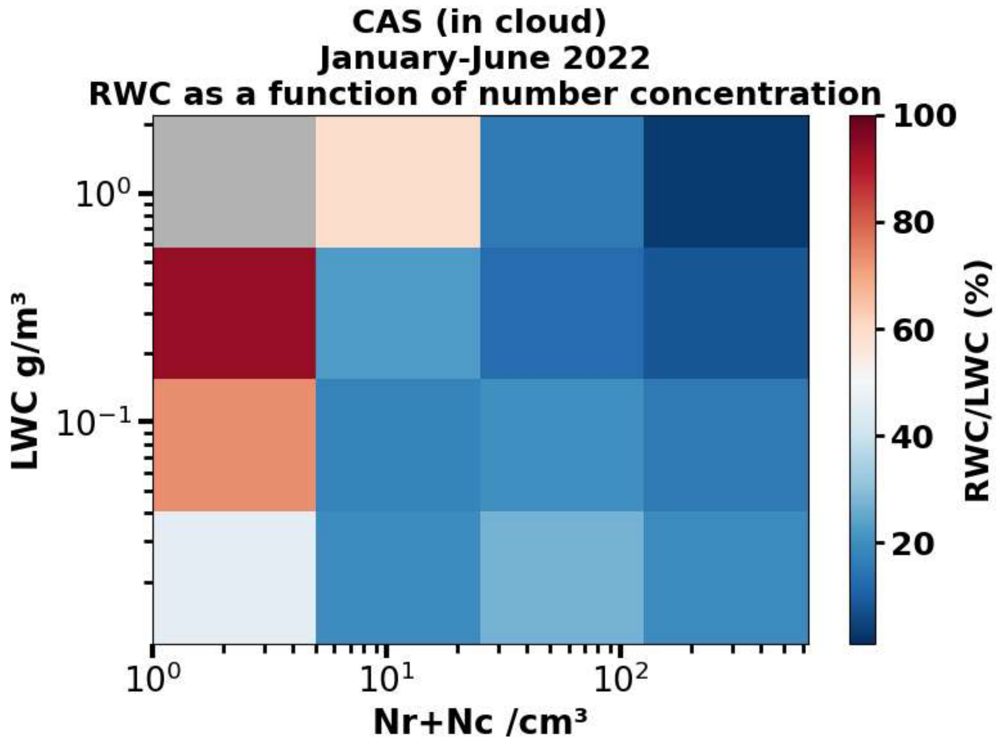

Figure 26 RWC as a function of number concentration and total LWC. Warmer colors indicate a higher fraction of RWC.

Figure 26 shows the key controlling factors in precipitation formation, but it does not isolate the impacts of GCCN on precipitation efficiency. To achieve this, we set a fixed LWC and number concentration. We select 0.1 to 0.3 g m^{-3} LWC and 50 to 200 cm^{-3} based on the high density of data points (black box region in Figure 27). We began this analysis using a 10x10 binning scheme but transitioned to a 4x4 bin setup because the finer binning resulted in too few data points per bin, making the analysis less statistically robust. When we applied our fixed LWC and Nr+Nc concentration ranges, the updated binning produced an average of 200–400 points per bin, ensuring more stable and reliable estimates of RWC/LWC.

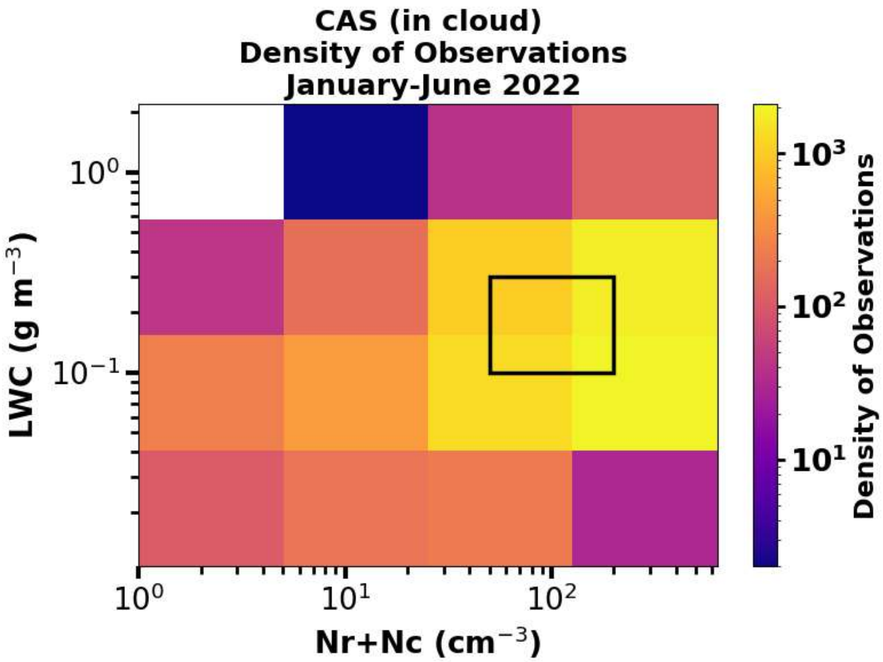

Figure 27 Selecting a region to perform fixed LWC and number concentration analysis based on the density of observations.

We want to use the isolated region 0.1 to 0.3 g m^{-3} LWC and 50 to 200 cm^{-3} in Figure 27 to look at RWC conditions as a function of varying amount of GCCN. Specifically, we want to compare high and low amounts of GCCN in this region. We take our previously calculated leg-averaged GCCN concentrations (Section 3b) by computing the mean GCCN concentration across all legs within each flight. Since our data is stored in leg averages rather than at 1 Hz resolution, this approach results an average GCCN concentration per each of our 75 flights. To categorize each flight, we take the top 50% (37 flights) as "high GCCN" (mean=0.8 cm^{-3}) and the bottom 50% (38 flights) as "low GCCN" (mean=0.3 cm^{-3}). To assess the robustness of our results using 50% split categories, we repeated the same analysis with a “high GCCN” category of the top 20% of flights and a “low GCCN” category of the bottom 80% of flights and a “high GCCN” category of the top 40% of flights and a “low GCCN” category of the bottom 60% of flights (Figure S3). The observed differences in RWC/LWC remained consistent across these thresholds, indicating that our results are robust. We then recompute RWC within the same region for both categories for the 50% split (Figure 28). We group the data by flight-mean GCCN. Violin plots depicting the distribution of GCCN concentration for each category are shown in Figure 29.

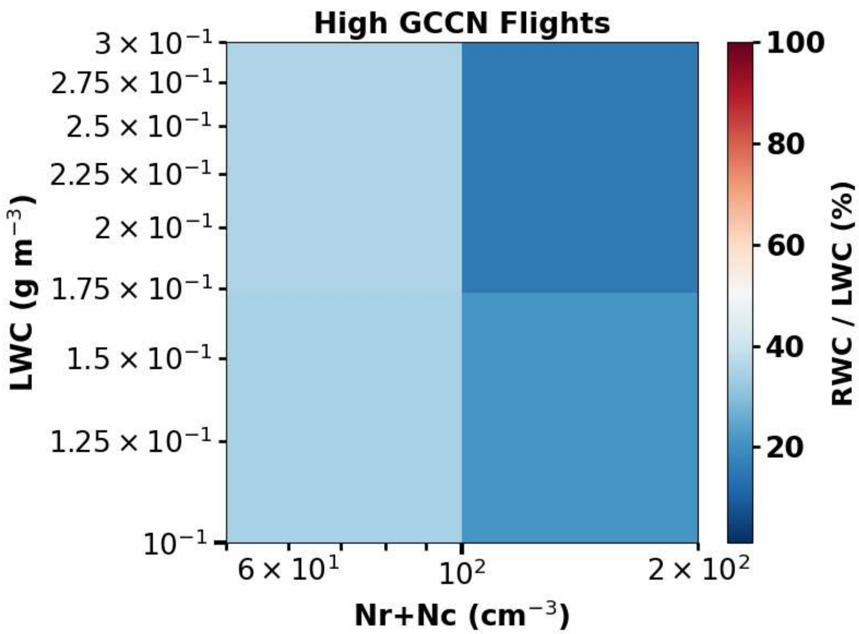

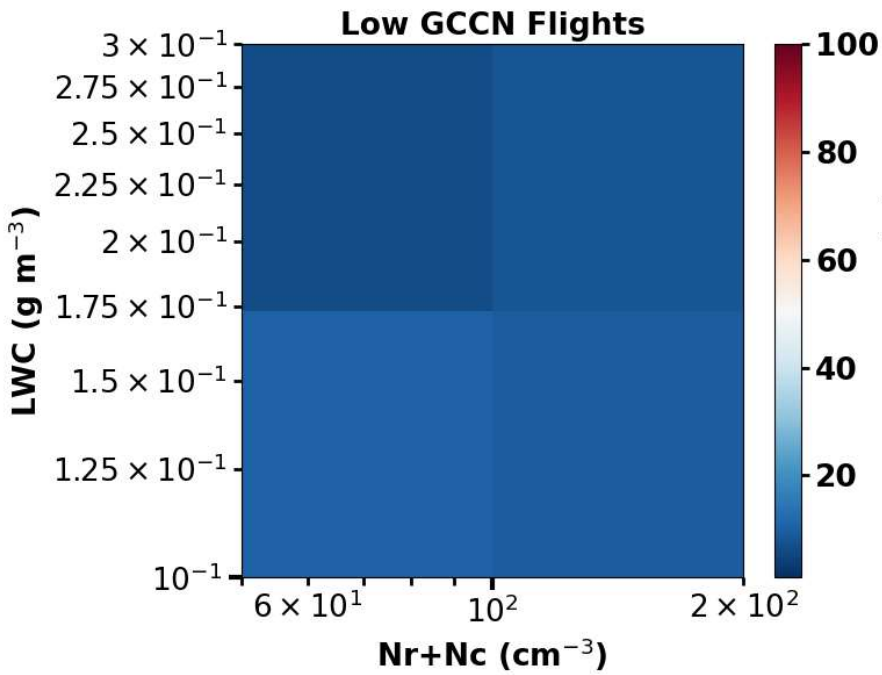

Figure 28 RWC as a function of fixed LWC (0.1 to 0.3 g m^{-3}) and concentration (50 to 200 cm^{-3}) for flights containing higher amounts of GCCN (upper) versus lower amounts of GCCN (lower). Warmer colors indicated higher RWC.

In Figure 28, the "high GCCN" flight category exhibits more regions of enhanced RWC/LWC (%), particularly at higher LWC values (~0.25–0.3 g m^{-3}) and lower-to-moderate droplet concentrations (~50–100 cm^{-3}). This suggests that higher amounts of GCCN tend to lead to higher amounts of precipitation for given values of LWC and Nr+Nc. There is a clear increase in rainwater content between the "high GCCN" and "low GCCN" categories. To visualize this difference more clearly and assess statistical significance, we performed bootstrapping within each bin. For each bin, we resampled 10,000 times with replacement to compute a distribution of mean differences, from which we derived 90% confidence intervals and determined significance based on whether the interval excluded zero (Figure 30).

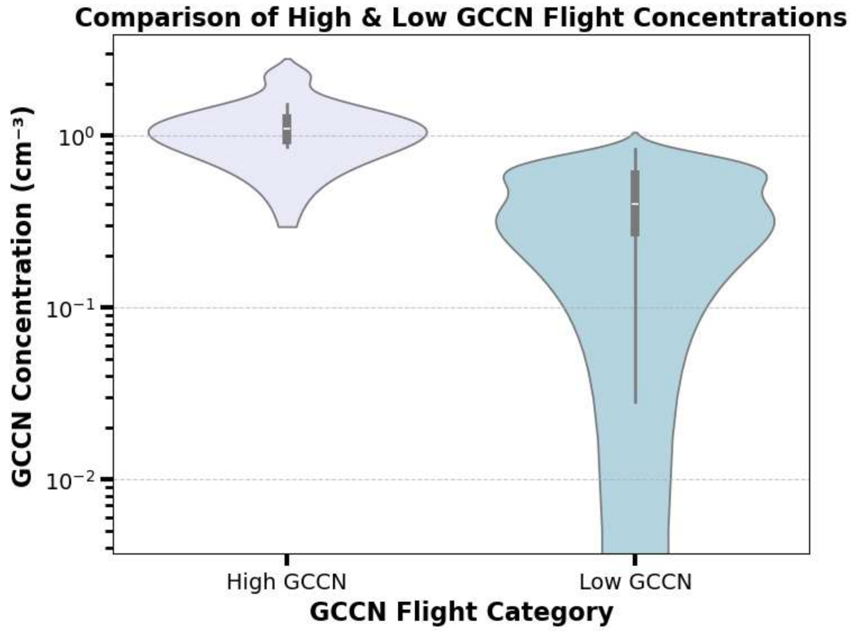

Figure 29 Distributions of "high GCCN" number concentration and "low GCCN" number concentration. The width of each violin represents the density of data points, with solid gray lines indicating the interquartile range (IQR) and white dots representing the median values.

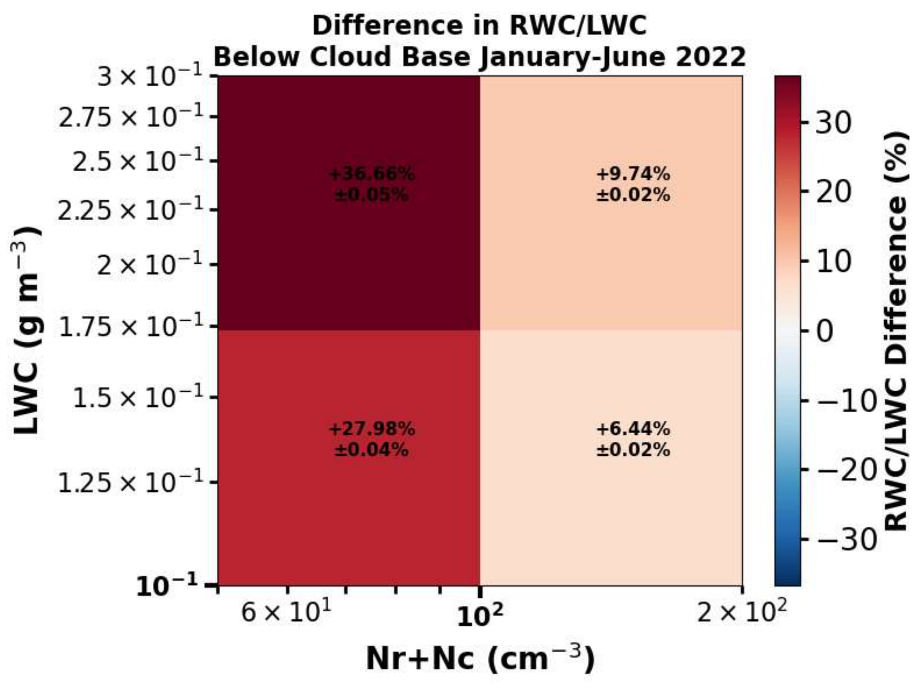

Figure 30 Difference in RWC between "high GCCN" and "low GCCN" flight categories as a function of fixed LWC and fixed concentration. Each grid cell shows the mean difference in RWC/LWC (%) with bootstrapped ±90% confidence intervals, computed from 10,000 resamples and the standard error.

There is an increase in RWC for flights containing higher concentrations of giant cloud condensation nuclei throughout all of the grided bins, with the highest increase being at our highest LWC and lowest number concentration (upper left grid cell). This enhancement suggests that the presence of GCCN contributes to an overall increase in rainwater content, consistent with the hypothesis that larger aerosols increase collision-coalescence efficiency and overall production of drizzle.

Given that our model results in PySDM show that mass might be more dominate in influencing drizzle than concentration, we also compute rainwater content for our fixed region of LWC and concentration, but this time isolate the effects of mass of GCCN, rather than concentration of GCCN. We calculate our dry GCCN mass (Section 3c) and continue to categorize it by flight in the same fashion as our GCCN categories above. To categorize each flight, we take the top 50% (37 flights) as "high GCCN mass" (mean = 42 $ug\, m^{-3}$) and the bottom 50% (38 flights) as "low GCCN mass" (mean = 4.3 $ug\, m^{-3}$). Again, to assess the robustness of our results using 50% split categories, we repeated the same analysis with a “high GCCN” category of the top 20% of flights and a “low GCCN” category of the bottom 80% of flights and a “high GCCN” category of the top 40% of flights and a “low GCCN” category of the bottom 60% of flights (Figure S5). The observed differences in RWC/LWC remained consistent across these thresholds, indicating that our results are robust. We then recompute RWC within the same region for both mass categories (Figure 31). Violin plots depicting the distribution of GCCN mass for each category are shown in Figure 32. We compute another difference plot to visualize how RWC is impacted by higher GCCN mass versus lower GCCN mass more clearly and continue to use our bootstrapping technique of resampling 10,000 times with replacement (Figure 32).

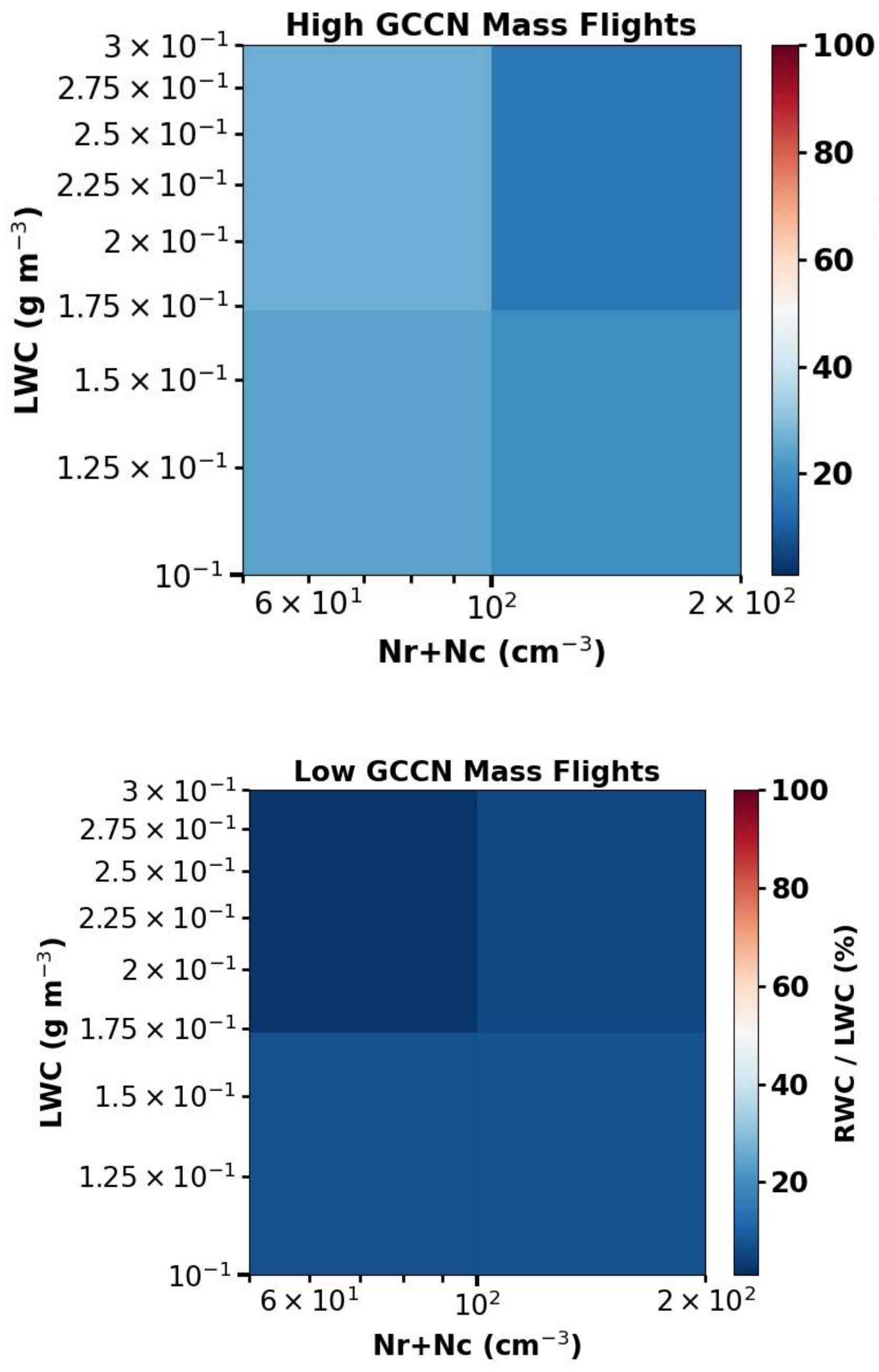

Figure 31 RWC as a function of fixed LWC (0.1 to 0.3 g m^{-3}) and concentration (50 to 200 cm^{-3}) for flights containing higher mass of GCCN (upper) versus lower mass of GCCN (lower). Warmer colors indicated higher RWC.

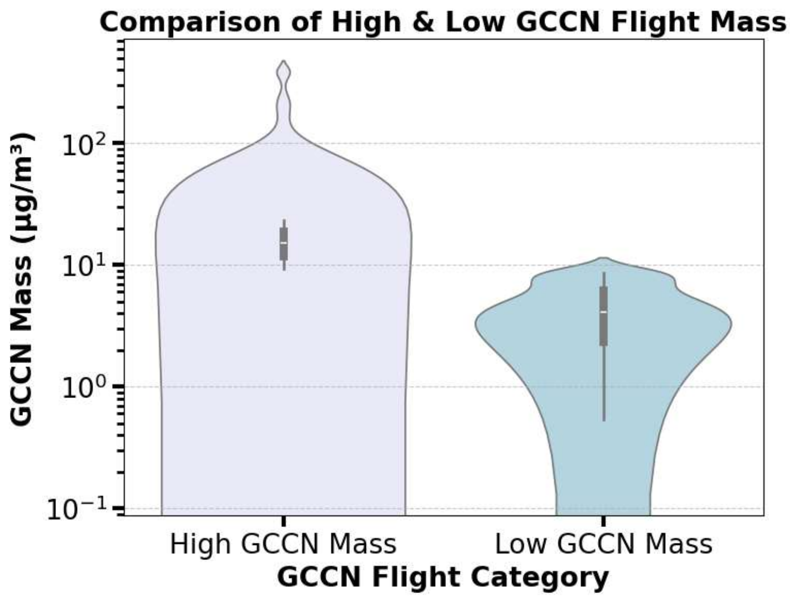

Figure 32 Distributions of "high GCCN mass" and "low GCCN mass". The width of each violin represents the density of data points, with solid gray lines indicating the interquartile range (IQR) and white dots representing the median values.

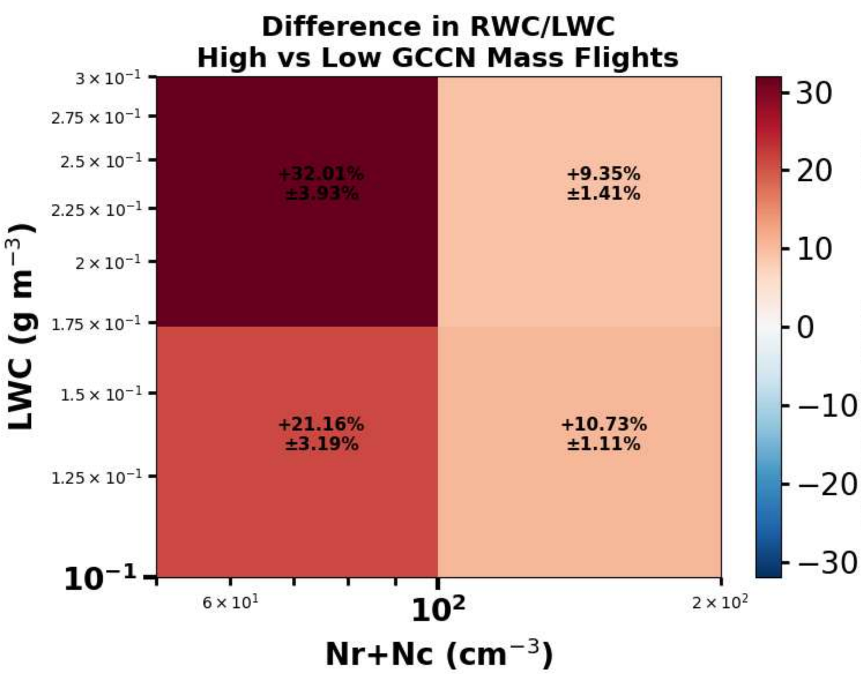

Figure 33 Difference in RWC between "high GCCN mass" and "low GCCN mass" flight categories as a function of fixed LWC and concentration. Each grid cell shows the mean difference in RWC/LWC (%) with bootstrapped ±90% confidence intervals, computed from 10,000 resamples and the standard error.

There is an increase in RWC for flights containing higher GCCN mass (larger coarse-mode particles) across all gridded bins, with the highest enhancement occurring in the highest LWC and lowest number concentration bin (upper left grid cell). This is slightly lower than the increase seen in the same bin for high vs. low GCCN concentration (Figure 30). However, at higher number concentrations (lower right grid cell), RWC increases more in response to larger GCCN than it does in response to more GCCN, when comparing Figure 30 and Figure 33. This suggests that the mass of coarse-mode aerosols may exert a stronger influence on RWC than their number concentration, in agreement with our PySDM case study simulations. The larger GCCN likely enhance drizzle formation by increasing droplet collection efficiency. Finally, we show a final violin plot comparing RWC across both concentration and mass (Figure 34). The violin plot shows that GCCN mass exhibits a wider spread and higher median RWC compared to concentration, with high mass flights having a significantly elevated median and a narrow interquartile range (IQR) at higher RWC values, while high concentration flights show a lower median with a broader IQR and a more even distribution across lower RWC values. We see that mass has a stronger and more consistent influence on RWC compared to concentration.

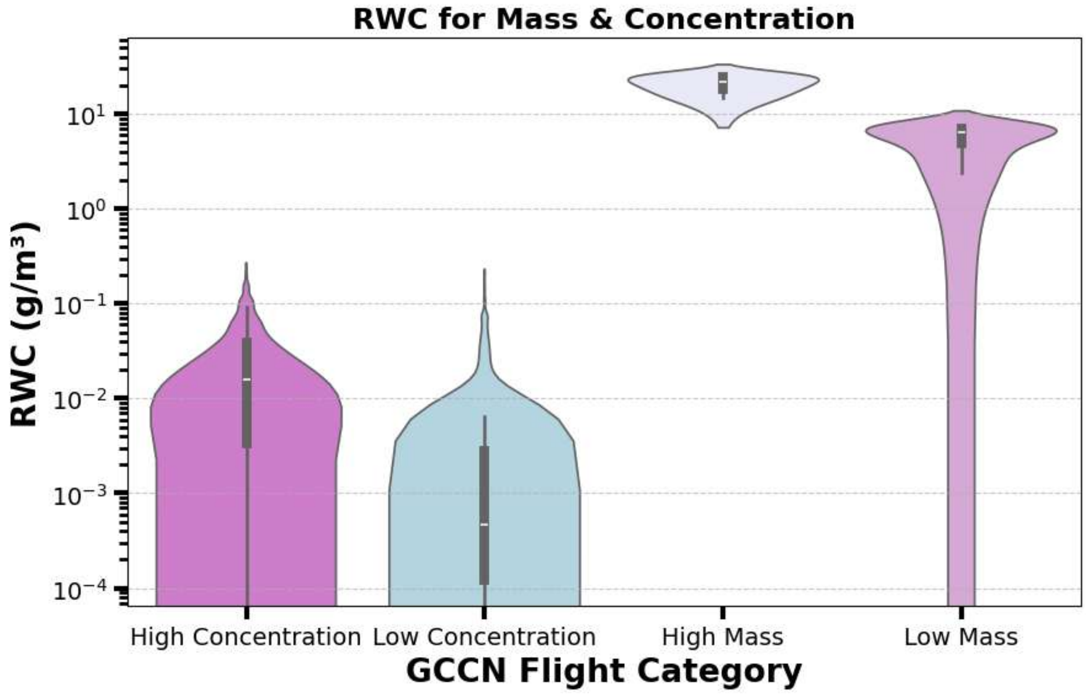

Figure 34 Violin plot showing the distribution of RWC for high and low GCCN mass and concentration flights. The width of each violin represents the density of data points, with solid gray lines indicating the interquartile range (IQR) and white dots representing the median values. Different colors distinguish between high and low GCCN categories for both mass (lavender and light purple) and concentration (light blue and pink).

4. Summary and Conclusions

This study aims to improve our understanding of the interactions between giant cloud condensation nuclei and marine stratocumulus clouds. We investigate these interactions with aircraft observations from the NASA Sub-Orbital ACTIVATE campaign over the Western North Atlantic Ocean. This research investigates the impacts of GCCN by first characterizing coarse-mode observations through size-resolved aerosol concentration profiles. This allows us to compare our observations with previous work (Colón-Robles et al., 2006) to evaluate the consistency of coarse-mode aerosol characteristics across different studies. We also analyze the influence of wind speed on coarse-mode aerosol concentration and size distribution. We achieve this by comparing our aerosol distributions with previous literature (Colón-Robles, et al., 2006), averaging our distributions based on average wind speed, and computing statistical correlations between wind speed, total concentration, and aerosol mass. Finally, we assess the impacts of GCCN on drizzle formation through PySDM and observationally derived rainwater content. The three main findings from this study are:

- Coarse-mode aerosols follow an exponential decay distribution, consistent with prior studies, though large counting errors affect the largest particle sizes.
- The relationship between wind speed and coarse-mode aerosol concentration is positive and comparable to past studies (Colón-Robles, et al., 2006) when averaging multiple flight legs, suggesting that longer sample time helps reveal this correlation more clearly.
- The presence of giant cloud condensation nuclei enhances drizzle formation, with mass playing a more consistent role than concentration.

The analysis of 460 dry size distributions from the cloud-aerosol spectrometer consistently show roughly exponential distributions. Smaller coarse-mode particles (~2-10 μm) tend to dominate the total aerosol concentration in our dataset. The dry distributions are impacted by high counting errors toward the larger size ranges (>10 μm diameter) resulting in a flattening of the distributions, rather than the steep decline toward the larger particle sizes in similar studies (Colón-Robles, et al., 2006). We compare our averaged dry distributions with Colón-Robles, et al., 2006 and find our averaged dry distribution agrees quite well despite large counting errors from short leg sample time. Our concentrations are higher than the 2006 study, on average, but we recognize that our size-resolved aerosol distributions are derived from instruments with different detection limits, strict clear-sky sampling conditions, and significantly shorter flight leg times, which may contribute to these differences. Despite these differences, the overall exponential decay structure is consistent across Colón-Robles, et al., 2006, reinforcing the robustness of our methodology in representing sea spray aerosol size distributions. Furthermore, the fluctuations observed beyond 10 μm in our observations from the CAS, and in observations from Colón-Robles, et al., 2006 suggest general increased variability in the larger coarse-mode range between the two studies. Ultimately, these results confirm that our observed size distributions of mass and concentration are broadly similar to those from other studies that have attempted to measure GCCN and this builds confidence that our quantification of GCCN levels in the ACTIVATE region (where there have not been prior studies like this) are quantitatively similar to GCCN distributions in other regions with similar wind speeds. Therefore, they provide a strong foundation for our further analysis with GCCN, wind speed, and precipitation processes.

The relationship between wind speed and coarse-mode aerosol concentrations in this study aligns with previous findings (Colón-Robles, et al., 2006, Woodcock 1953, Lewis and Schwartz 2004), but only when flight legs are averaged together to reveal correlations that might not be as transparent with the low sample time in ACTIVATE. While past studies (Colón-Robles, et al., 2006) found a strong positive correlation between wind speed and total aerosol concentration, our analysis showed only a weak or negligible correlation for both the CAS and the CDP, unless we average multiple distributions together based on the average 10 m wind speed associated with each distribution. This suggests that while wind speed does contribute to increased coarse-mode aerosol production, the presence of this relationship might be dependent on the particle sample volume.

We would also expect concentration to increase with increasing wind speed, but even when averaging our distributions together, we saw that higher wind speeds correspond to greater total concentrations only some of the time. For the CAS, the highest wind speed bin with an average wind speed of 9.8 m s^{-1}did not result in the largest concentration of particles. For the CDP, the two moderate wind speed bins with average wind speeds at 4.8 m s^{-1} and 7.5 m s^{-1} resulted in very similar total concentrations. After averaging our distributions together, the positive relationship between these averaged distributions and wind speed is more comparable to Colón-Robles et al. 2006. We also find that mass dependence on wind speed is noisier than for total number concentration. The correlation between mass and wind speed is weaker than the correlation between the total concentration and wind speed. However, the trends for mass and wind speed for each instrument are still positive and stronger than the noisy trend between wind speed and individual flight legs.

Previous studies have analyzed various other source functions of GCCN, such as sea surface temperature and wave dynamics (Dana & Hales, 1976; Skartveit, 1982; Lewis and Schwartz 2004; Jaeglé et al. 2011; Grythe et al., 2014, Salter et al., 2015). It would be beneficial to analyze our observations from ACTIVATE in terms of other source functions of GCCN rather than focusing analysis on wind speed, since high counting errors for low sampling time can obscure this relationship. For example, the European Centre for Medium-Range Weather Forecasts (ECMWF) Ocean Wave Model provides information on wave height. We can use this with ERA-5 reanalysis data to take a closer look at the production of GCCN.

Our simulations with PySDM reveal clear connections between the presence of GCCN and drizzle production. All three case studies containing GCCN, regardless of their differing masses and concentrations, showed increased drizzle compared to the control simulation with no GCCN. Our case studies allowed us to isolate the roles of total GCCN concentration and GCCN mass, showing that both factors contribute to drizzle formation, but their relative importance varies. The relationship with mass and drizzle production in our simulations is monotonic. As mass increases, so does the drizzle rate. The concentration and drizzle production relationship, varies. For the case of February 3, 2022, it appears the mass may be more dominant in driving drizzle production than concentration. This suggests that, for this example, GCCN mass may exert a stronger influence on drizzle rate when aerosol size distributions shift toward larger particles, rather than more numerous smaller-sized coarse-mode aerosols. However, this relationship between these three case studies of differing mass and concentration is not definitive. We need to test more distributions before we can truly assess whether mass or concentration really controls drizzle. Given that we have 460 possible distributions to serve as model input, it is essential to expand our analysis beyond these three case studies to leverage the full extent of our dataset and robustly determine the relative roles of GCCN mass and concentration in drizzle formation.

Furthermore, there is a large spread in precipitation rates across all simulations (Figure 28) for every case, including the accumulation mode simulations. Some simulations indicated no precipitation at all. Given that the collision scheme in this model is stochastic, this could contribute to the noise and variability observed across simulations. To better understand these uncertainties, we could adjust our model setup by varying the simulation timing or adjusting some of the input variables.

Our observational analysis of RWC under fixed LWC and total concentration conditions reveals that higher amounts of GCCN increase RWC. The "high GCCN" flight category exhibits more frequent occurrences of high RWC/LWC ratios, particularly in conditions with already moderate to high LWC (Figure 32). This effect is further highlighted in the difference plot, where the largest enhancements in RWC occur at higher LWC values (Figure 34). However, we incorporated our GCCN measurements as averages over entire flight legs, but we use cloud and rain droplet concentration data at much finer temporal resolution. This discrepancy in scale may contribute to inconsistencies in our comparisons, as we cannot directly factor in the instantaneous GCCN number concentrations. They are in clear-sky conditions while the raindrop and cloud droplet concentrations are in-cloud. We also performed the same

RWC analysis but for mass, rather than concentration. We see that mass has a stronger and more consistent influence on RWC compared to concentration, which is consistent with our modeling case studies. However, we do not actually know how robust the differences in RWC for both concentration and mass are for their respective high and low categories, given that some grid cells have more data points than others. To address this challenge, we need to perform statistical significance testing across every region of our difference map to determine where the observed RWC differences between high and low categories are most significant. Moreover, rather than using a simple data split (low concentration/low mass) vs. (high concentration/mass) threshold, we should explore alternative methods to more distinctly separate high and low GCCN conditions.

The overall findings of this study provide insight into the interactions between giant cloud condensation nuclei and marine stratocumulus clouds using observational data. We find that wind speed can increase the concentration of GCCN and that GCCN can influence drizzle in marine stratocumulus clouds. These effects can have broader impacts on climate as GCCN can influence cloud lifetime and cloud albedo. GCCN concentrations may enhance precipitation efficiency, leading to shorter-lived clouds and decreases in cloud albedo. Since stratocumulus clouds are key in modulating Earth's radiation budget, understanding the role that coarse-mode sea spray aerosols play is essential for improving climate model representations of cloud-aerosol interactions.

Bibliography

0237 Pdf Atmospheric Chemistry And Physics 2nd Ed J. Seinfeld, S. Pandis (Wiley, 2006) WW. Accessed May 13, 2025. http://archive.org/details/0237-pdf-atmospheric-chemistry-and-physics-2nd-ed-j.-seinfeld-s.-pandis-wiley-2006-ww.

Ackerman, Andrew S., Michael P. Kirkpatrick, David E. Stevens, and Owen B. Toon. "The Impact of Humidity above Stratiform Clouds on Indirect Aerosol Climate Forcing." *Nature* 432, no. 7020 (December 2004): 1014–17. https://doi.org/10.1038/nature03174.

Ackerman, Andrew S., Margreet C. vanZanten, Bjorn Stevens, Verica Savic-Jovcic, Christopher S. Bretherton, Andreas Chlond, Jean-Christophe Golaz, et al. "Large-Eddy Simulations of a Drizzling, Stratocumulus-Topped Marine Boundary Layer," March 1, 2009. https://doi.org/10.1175/2008MWR2582.1.

Ackerman, Katherine L., Alison D. Nugent, and Chung Taing. "Mechanisms Controlling Giant Sea Salt Aerosol Size Distributions along a Tropical Orographic Coastline." *Atmospheric Chemistry and Physics* 23, no. 21 (November 3, 2023): 13735–53. https://doi.org/10.5194/acp-23-13735-2023.

"Aerosol–Cloud Drop Concentration Closure for Clouds Sampled during the International Consortium for Atmospheric Research on Transport and Transformation 2004 Campaign - Fountoukis - 2007 - Journal of Geophysical Research: Atmospheres - Wiley Online Library." Accessed May 13, 2025. https://agupubs.onlinelibrary.wiley.com/doi/full/10.1029/2006JD007272.

"AR5 Synthesis Report: Climate Change 2014 — IPCC." Accessed May 13, 2025. https://www.ipcc.ch/report/ar5/syr/.

Barr, Jason. Stochastic Collection Model for ACTVATE, 2025.

Bartman, Piotr, Oleksii Bulenok, Kamil Górski, Anna Jaruga, Grzegorz Łazarski, Michael A. Olesik, Bartosz Piasecki, Clare E. Singer, Aleksandra Talar, and Sylwester Arabas. "PySDM v1: Particle-Based Cloud Modeling Package for Warm-Rain Microphysics and Aqueous Chemistry." *Journal of Open Source Software* 7, no. 72 (April 25, 2022): 3219. https://doi.org/10.21105/joss.03219.

Bellouin, N., J. Quaas, E. Gryspeerdt, S. Kinne, P. Stier, D. Watson-Parris, O. Boucher, et al. "Bounding Global Aerosol Radiative Forcing of Climate Change." *Reviews of Geophysics* 58, no. 1 (2020): e2019RG000660. https://doi.org/10.1029/2019RG000660.

Berry, E. X. "Cloud Droplet Growth by Collection," November 1, 1967. https://journals.ametsoc.org/view/journals/atsc/24/6/1520-0469_1967_024_0688_cdgbc_2_0_co_2.xml.

Bisht, Ravi. "An Introduction to Boundary Layer Meteorology." *Springer*. Accessed May 13, 2025. https://www.academia.edu/41118210/An_Introduction_to_Boundary_Layer_Meteorology.

Bretherton, C. S., P. N. Blossey, and J. Uchida. "Cloud Droplet Sedimentation, Entrainment Efficiency, and Subtropical Stratocumulus Albedo." *Geophysical Research Letters* 34, no. 3 (2007). https://doi.org/10.1029/2006GL027648.

Chen, Ting, Yuangchong Zhang, and William B. Rossow. "Sensitivity of Atmospheric Radiative Heating Rate Profiles to Variations of Cloud Layer Overlap," August 15, 2000. https://journals.ametsoc.org/view/journals/clim/13/16/1520-0442_2000_013_2941_soarhr_2.0.co_2.xml.

Colón-Robles, Marilé, Robert M. Rauber, and Jørgen B. Jensen. "Influence of Low-Level Wind Speed on Droplet Spectra near Cloud Base in Trade Wind Cumulus." *Geophysical Research Letters* 33, no. 20 (2006). https://doi.org/10.1029/2006GL027487.

"Condensational Growth of Drops Formed on Giant Sea-Salt Aerosol Particles in: Journal of the Atmospheric Sciences Volume 74 Issue 3 (2017)." Accessed May 13, 2025. https://journals.ametsoc.org/view/journals/atsc/74/3/jas-d-15-0370.1.xml.

Corral, Andrea F., Rachel A. Braun, Brian Cairns, Vesta Afzali Gorooh, Hongyu Liu, Lin Ma, Ali Hossein Mardi, et al. "An Overview of Atmospheric Features Over the Western North Atlantic Ocean and North American East Coast – Part 1: Analysis of Aerosols, Gases, and Wet Deposition Chemistry." *Journal of Geophysical Research: Atmospheres* 126, no. 4 (2021): e2020JD032592. https://doi.org/10.1029/2020JD032592.

Dadashazar, Hossein, Andrea F. Corral, Ewan Crosbie, Sanja Dmitrovic, Simon Kirschler, Kayla McCauley, Richard Moore, et al. "Organic Enrichment in Droplet Residual Particles Relative to out of Cloud over the

Northwestern Atlantic: Analysis of Airborne ACTIVATE Data." *Atmospheric Chemistry and Physics* 22, no. 20 (October 28, 2022): 13897–913. https://doi.org/10.5194/acp-22-13897-2022.

Dana, M. Terry, and Jeremy M Hales. "Statistical Aspects of the Washout of Polydisperse Aerosols." *Atmospheric Environment (1967)* 10, no. 1 (January 1, 1976): 45–50. https://doi.org/10.1016/0004-6981(76)90258-4.

Daoud, Wessam Z., Jonathan D. W. Kahl, and Jugal K. Ghorai. "On the Synoptic-Scale Lagrangian Autocorrelation Function," February 1, 2003. https://journals.ametsoc.org/view/journals/apme/42/2/1520-0450_2003_042_0318_otssla_2.0.co_2.xml.

Diskin, G. "DLH: Diode Laser Hygrometer Measurements of H2O(v).," 2022.

Dziekan, Piotr, Jørgen B. Jensen, Wojciech W. Grabowski, and Hanna Pawlowska. "Impact of Giant Sea Salt Aerosol Particles on Precipitation in Marine Cumuli and Stratocumuli: Lagrangian Cloud Model Simulations," December 1, 2021. https://doi.org/10.1175/JAS-D-21-0041.1.

Feingold, Graham, William R. Cotton, Sonia M. Kreidenweis, and Janel T. Davis. "The Impact of Giant Cloud Condensation Nuclei on Drizzle Formation in Stratocumulus: Implications for Cloud Radiative Properties," December 1, 1999. https://journals.ametsoc.org/view/journals/atsc/56/24/1520-0469_1999_056_4100_tiogcc_2.0.co_2.xml.

Feingold, Graham, Sonia M. Kreidenweis, Bjorn Stevens, and W. R. Cotton. "Numerical Simulations of Stratocumulus Processing of Cloud Condensation Nuclei through Collision-Coalescence." *Journal of Geophysical Research: Atmospheres* 101, no. D16 (1996): 21391–402. https://doi.org/10.1029/96JD01552.

Fountoukis, Christos, Athanasios Nenes, Nicholas Meskhidze, Roya Bahreini, William C. Conant, Haflidi Jonsson, Shane Murphy, et al. "Aerosol–Cloud Drop Concentration Closure for Clouds Sampled during the International Consortium for Atmospheric Research on Transport and Transformation 2004 Campaign." *Journal of Geophysical Research: Atmospheres* 112, no. D10 (2007). https://doi.org/10.1029/2006JD007272.

GitHub. "Meteorological-Books/Atmospheric-Boundary-Layer/An-Introduction-to-Boundary-Layer-Meteorology-Stull.Pdf at Master · kbSSR/Meteorological-Books." Accessed May 13, 2025. https://github.com/kbSSR/Meteorological-Books/blob/master/Atmospheric-boundary-layer/An-Introduction-to-Boundary-Layer-Meteorology-Stull.pdf.

"GMD - Modeling Collision–Coalescence in Particle Microphysics: Numerical Convergence of Mean and Variance of Precipitation in Cloud Simulations Using the University of Warsaw Lagrangian Cloud Model (UWLCM) 2.1." Accessed May 13, 2025. https://gmd.copernicus.org/articles/17/759/2024/.

"GMD - Predicting the Morphology of Ice Particles in Deep Convection Using the Super-Droplet Method: Development and Evaluation of SCALE-SDM 0.2.5-2.2.0, -2.2.1, and -2.2.2." Accessed May 13, 2025. https://gmd.copernicus.org/articles/13/4107/2020/.

Grythe, H., J. Ström, R. Krejci, P. Quinn, and A. Stohl. "A Review of Sea-Spray Aerosol Source Functions Using a Large Global Set of Sea Salt Aerosol Concentration Measurements." *Atmospheric Chemistry and Physics* 14, no. 3 (February 3, 2014): 1277–97. https://doi.org/10.5194/acp-14-1277-2014.

Hartmann, Dennis L., Maureen E. Ockert-Bell, and Marc L. Michelsen. "The Effect of Cloud Type on Earth's Energy Balance: Global Analysis," November 1, 1992. https://journals.ametsoc.org/view/journals/clim/5/11/1520-0442_1992_005_1281_teocto_2_0_co_2.xml.

Hartmann, Dennis L., and David A. Short. "On the Use of Earth Radiation Budget Statistics for Studies of Clouds and Climate," June 1, 1980. https://journals.ametsoc.org/view/journals/atsc/37/6/1520-0469_1980_037_1233_otuoer_2_0_co_2.xml.

Heintzenberg, J., D. C. Covert, and R. van Dingenen. "Size Distribution and Chemical Composition of Marine Aerosols: A Compilation and Review." *Tellus B: Chemical and Physical Meteorology* 52, no. 4 (January 1, 2000). https://doi.org/10.3402/tellusb.v52i4.17090.

Jaeglé, L., P. K. Quinn, T. S. Bates, B. Alexander, and J.-T. Lin. "Global Distribution of Sea Salt Aerosols: New Constraints from in Situ and Remote Sensing Observations." *Atmospheric Chemistry and Physics* 11, no. 7 (April 4, 2011): 3137–57. https://doi.org/10.5194/acp-11-3137-2011.

Jensen, Jørgen B., and Sunhee Lee. “Giant Sea-Salt Aerosols and Warm Rain Formation in Marine Stratocumulus,” December 1, 2008. https://doi.org/10.1175/2008JAS2617.1.

Jensen, Jørgen B., and Alison D. Nugent. “Condensational Growth of Drops Formed on Giant Sea-Salt Aerosol Particles,” March 1, 2017. https://doi.org/10.1175/JAS-D-15-0370.1.

Johnson, David B. “The Role of Giant and Ultragiant Aerosol Particles in Warm Rain Initiation,” February 1, 1982. https://journals.ametsoc.org/view/journals/atsc/39/2/1520-0469_1982_039_0448_trogau_2_0_co_2.xml.

Jung, E., B. A. Albrecht, H. H. Jonsson, Y.-C. Chen, J. H. Seinfeld, A. Sorooshian, A. R. Metcalf, S. Song, M. Fang, and L. M. Russell. “Precipitation Effects of Giant Cloud Condensation Nuclei Artificially Introduced into Stratocumulus Clouds.” *Atmospheric Chemistry and Physics* 15, no. 10 (May 22, 2015): 5645–58. https://doi.org/10.5194/acp-15-5645-2015.

Kirschler, Simon, Christiane Voigt, Bruce Anderson, Ramon Campos Braga, Gao Chen, Andrea F. Corral, Ewan Crosbie, et al. “Seasonal Updraft Speeds Change Cloud Droplet Number Concentrations in Low-Level Clouds over the Western North Atlantic.” *Atmospheric Chemistry and Physics* 22, no. 12 (June 28, 2022): 8299–8319. https://doi.org/10.5194/acp-22-8299-2022.

Klein, Stephen A., and Dennis L. Hartmann. “The Seasonal Cycle of Low Stratiform Clouds,” August 1, 1993. https://journals.ametsoc.org/view/journals/clim/6/8/1520-0442_1993_006_1587_tscols_2_0_co_2.xml.

Kubar, Terence L., Dennis L. Hartmann, and Robert Wood. “Understanding the Importance of Microphysics and Macrophysics for Warm Rain in Marine Low Clouds. Part I: Satellite Observations,” October 1, 2009. https://doi.org/10.1175/2009JAS3071.1.

“Large-Eddy Simulations of Marine Boundary Layer Clouds Associated with Cold-Air Outbreaks during the ACTIVATE Campaign. Part II: Aerosol–Meteorology–Cloud Interaction in: Journal of the Atmospheric Sciences Volume 80 Issue 4 (2023).” Accessed May 13, 2025. https://journals.ametsoc.org/view/journals/atsc/80/4/JAS-D-21-0324.1.xml?tab_body=pdf.

“Large-Eddy Simulations of Marine Boundary Layer Clouds Associated with Cold-Air Outbreaks during the ACTIVATE Campaign. Part II: Aerosol–Meteorology–Cloud Interaction in: Journal of the Atmospheric

Sciences Volume 80 Issue 4 (2023).” Accessed May 13, 2025. https://journals.ametsoc.org/view/journals/atsc/80/4/JAS-D-21-0324.1.xml.

L’Ecuyer, Tristan S., Wesley Berg, John Haynes, Matthew Lebsock, and Toshihiko Takemura. “Global Observations of Aerosol Impacts on Precipitation Occurrence in Warm Maritime Clouds.” *Journal of Geophysical Research: Atmospheres* 114, no. D9 (2009). https://doi.org/10.1029/2008JD011273.

L’Ecuyer, Tristan S., Yun Hang, Alexander V. Matus, and Zhien Wang. “Reassessing the Effect of Cloud Type on Earth’s Energy Balance in the Age of Active Spaceborne Observations. Part I: Top of Atmosphere and Surface,” October 1, 2019. https://doi.org/10.1175/JCLI-D-18-0753.1.

Lewis, Ernie R. “An Examination of Köhler Theory Resulting in an Accurate Expression for the Equilibrium Radius Ratio of a Hygroscopic Aerosol Particle Valid up to and Including Relative Humidity 100%.” *Journal of Geophysical Research: Atmospheres* 113, no. D3 (2008). https://doi.org/10.1029/2007JD008590.

Lewis, Ernie R., and Stephen E. Schwartz. “Methods of Determining Size-Dependent Sea Salt Aerosol Production Fluxes.” In *Sea Salt Aerosol Production: Mechanisms, Methods, Measurements and Models*, 101–18. American Geophysical Union (AGU), 2004. https://doi.org/10.1002/9781118666050.ch3.

Li, Jing, Barbara E. Carlson, Yuk L. Yung, Daren Lv, James Hansen, Joyce E. Penner, Hong Liao, et al. “Scattering and Absorbing Aerosols in the Climate System.” *Nature Reviews Earth & Environment* 3, no. 6 (June 2022): 363–79. https://doi.org/10.1038/s43017-022-00296-7.

Li, Xiang-Yu, Hailong Wang, Jingyi Chen, Satoshi Endo, Simon Kirschler, Christiane Voigt, Ewan Crosbie, et al. “Large-Eddy Simulations of Marine Boundary Layer Clouds Associated with Cold-Air Outbreaks during the ACTIVATE Campaign. Part II: Aerosol–Meteorology–Cloud Interaction,” March 14, 2023. https://doi.org/10.1175/JAS-D-21-0324.1.

Lilly, D. K. “Models of Cloud-Topped Mixed Layers under a Strong Inversion.” *Quarterly Journal of the Royal Meteorological Society* 94, no. 401 (1968): 292–309. https://doi.org/10.1002/qj.49709440106.

Lohmann, U., and J. Feichter. “Global Indirect Aerosol Effects: A Review.” *Atmospheric Chemistry and Physics* 5, no. 3 (March 3, 2005): 715–37. https://doi.org/10.5194/acp-5-715-2005.

Martin, G. M., D. W. Johnson, and A. Spice. “The Measurement and Parameterization of Effective Radius of Droplets in Warm Stratocumulus Clouds,” July 1, 1994. https://journals.ametsoc.org/view/journals/atsc/51/13/1520-0469_1994_051_1823_tmapoe_2_0_co_2.xml.

Monahan, Edward C., Christopher W. Fairall, Kenneth L. Davidson, and Patricia Jones Boyle. “Observed Inter-Relations between 10m Winds, Ocean Whitecaps and Marine Aerosols.” *Quarterly Journal of the Royal Meteorological Society* 109, no. 460 (1983): 379–92. https://doi.org/10.1002/qj.49710946010.

Moore, Richard, and Luke Ziemba. “LARGE In-Situ Cloud Measurements for ACTIVATE Data Workshop.” 2022.

Mülmenstädt, Johannes, and Graham Feingold. “The Radiative Forcing of Aerosol–Cloud Interactions in Liquid Clouds: Wrestling and Embracing Uncertainty.” *Current Climate Change Reports* 4, no. 1 (March 1, 2018): 23–40. https://doi.org/10.1007/s40641-018-0089-y.

Nicholls, S. “The Dynamics of Stratocumulus: Aircraft Observations and Comparisons with a Mixed Layer Model.” *Quarterly Journal of the Royal Meteorological Society* 110, no. 466 (1984): 783–820. https://doi.org/10.1002/qj.49711046603.

Nicholls, S., and C. J. Readings. “Aircraft Observations of the Structure of the Lower Boundary Layer over the Sea.” *Quarterly Journal of the Royal Meteorological Society* 105, no. 446 (1979): 785–802. https://doi.org/10.1002/qj.49710544604.

———. “Aircraft Observations of the Structure of the Lower Boundary Layer over the Sea.” *Quarterly Journal of the Royal Meteorological Society* 105, no. 446 (1979): 785–802. https://doi.org/10.1002/qj.49710544604.

O’Dowd, Colin D., Michael H. Smith, Ian E. Consterdine, and Jason A. Lowe. “Marine Aerosol, Sea-Salt, and the Marine Sulphur Cycle: A Short Review.” *Atmospheric Environment* 31, no. 1 (January 1, 1997): 73–80. https://doi.org/10.1016/S1352-2310(96)00106-9.

"Operator Manual: Cloud Aerosol Spectrometer Depolarization Option (CAS-DPOL) – Droplet Measurement Technologies." Accessed May 7, 2025. https://www.dropletmeasurement.com/manual/operator-manual-cloud-aerosol-spectrometer-depolarization-option-cas-dpol/.

"Operator Manual: Cloud Droplet Probe (CDP-2) – Droplet Measurement Technologies." Accessed May 7, 2025. https://www.dropletmeasurement.com/manual/operations-manual-cloud-droplet-probe-cdp-2/.

Painemal, David, Andrea F. Corral, Armin Sorooshian, Michael A. Brunke, Seethala Chellappan, Vesta Afzali Gorooh, Seung-Hee Ham, et al. "An Overview of Atmospheric Features Over the Western North Atlantic Ocean and North American East Coast—Part 2: Circulation, Boundary Layer, and Clouds." *Journal of Geophysical Research: Atmospheres* 126, no. 6 (2021): e2020JD033423. https://doi.org/10.1029/2020JD033423.

"(PDF) Comments on 'Parameterization of the Autoconversion Process. Part I: Analytical Formulation of the Kessler-Type Parameterizations.'" Accessed May 13, 2025. https://www.researchgate.net/publication/234119957_Comments_on_Parameterization_of_the_Autoconversion_Process_Part_I_Analytical_Formulation_of_the_Kessler-Type_Parameterizations.

"(PDF) Measurements and Modelling of the Wind Speed Profile in the Marine Atmospheric Boundary Layer." *ResearchGate*. Accessed May 13, 2025. https://doi.org/10.1007/s10546-008-9323-9.

"(PDF) The 2DS (Stereo) Probe: Design and Preliminary Tests of a New Airborne, High-Speed, High-Resolution Particle Imaging Probe." *ResearchGate*, February 6, 2025. https://doi.org/10.1175/JTECH1927.1.

Persad, Geeta G., Bjørn H. Samset, and Laura J. Wilcox. "Aerosols Must Be Included in Climate Risk Assessments." *Nature* 611, no. 7937 (November 2022): 662–64. https://doi.org/10.1038/d41586-022-03763-9.

Petters, M. D., and S. M. Kreidenweis. "A Single Parameter Representation of Hygroscopic Growth and Cloud Condensation Nucleus Activity." *Atmospheric Chemistry and Physics* 7, no. 8 (April 18, 2007): 1961–71. https://doi.org/10.5194/acp-7-1961-2007.

Rémillard, Jasmine, Pavlos Kollias, Edward Luke, and Robert Wood. “Marine Boundary Layer Cloud Observations in the Azores,” November 1, 2012. https://doi.org/10.1175/JCLI-D-11-00610.1.

ResearchGate. “Occurrence of Lower Cloud Albedo in Ship Tracks.” Accessed May 7, 2025. https://www.researchgate.net/publication/258563763_Occurrence_of_lower_cloud_albedo_in_ship_tracks.

Rosenfeld, Daniel, Yannian Zhu, Minghuai Wang, Youtong Zheng, Tom Goren, and Shaocai Yu. “Aerosol-Driven Droplet Concentrations Dominate Coverage and Water of Oceanic Low-Level Clouds.” *Science* 363, no. 6427 (February 8, 2019): eaav0566. https://doi.org/10.1126/science.aav0566.

Salter, M. E., P. Zieger, J. C. Acosta Navarro, H. Grythe, A. Kirkevåg, B. Rosati, I. Riipinen, and E. D. Nilsson. “An Empirically Derived Inorganic Sea Spray Source Function Incorporating Sea Surface Temperature.” *Atmospheric Chemistry and Physics* 15, no. 19 (October 6, 2015): 11047–66. https://doi.org/10.5194/acp-15-11047-2015.

Seinfeld, John H., Christopher Bretherton, Kenneth S. Carslaw, Hugh Coe, Paul J. DeMott, Edward J. Dunlea, Graham Feingold, et al. “Improving Our Fundamental Understanding of the Role of Aerosol−cloud Interactions in the Climate System.” *Proceedings of the National Academy of Sciences* 113, no. 21 (May 24, 2016): 5781–90. https://doi.org/10.1073/pnas.1514043113.

Shima, S., K. Kusano, A. Kawano, T. Sugiyama, and S. Kawahara. “The Super-Droplet Method for the Numerical Simulation of Clouds and Precipitation: A Particle-Based and Probabilistic Microphysics Model Coupled with a Non-Hydrostatic Model.” *Quarterly Journal of the Royal Meteorological Society* 135, no. 642 (2009): 1307–20. https://doi.org/10.1002/qj.441.

Shipway, B. J., and A. A. Hill. “Diagnosis of Systematic Differences between Multiple Parametrizations of Warm Rain Microphysics Using a Kinematic Framework.” *Quarterly Journal of the Royal Meteorological Society* 138, no. 669 (2012): 2196–2211. https://doi.org/10.1002/qj.1913.

Skartveit, Arvid. “Wet Scavenging of Sea-Salts and Acid Compounds in a Rainy, Coastal Area.” *Atmospheric Environment (1967)* 16, no. 11 (January 1, 1982): 2715–24. https://doi.org/10.1016/0004-6981(82)90356-0.

Smith, Stuart D., Robert J. Anderson, Wiebe A. Oost, C. Kraan, Nico Maat, Janice De Cosmo, Kristina B. Katsaros, et al. "Sea Surface Wind Stress and Drag Coefficients: The Hexos Results." *Boundary-Layer Meteorology* 60, no. 1 (July 1, 1992): 109–42. https://doi.org/10.1007/BF00122064.

Snider, Jefferson R., Sarah Guibert, Jean-Louis Brenguier, and J.-P. Putaud. "Aerosol Activation in Marine Stratocumulus Clouds: 2. Köhler and Parcel Theory Closure Studies." *Journal of Geophysical Research: Atmospheres* 108, no. D15 (2003). https://doi.org/10.1029/2002JD002692.

Sorooshian, Armin, Mikhail D. Alexandrov, Adam D. Bell, Ryan Bennett, Grace Betito, Sharon P. Burton, Megan E. Buzanowicz, et al. "Spatially Coordinated Airborne Data and Complementary Products for Aerosol, Gas, Cloud, and Meteorological Studies: The NASA ACTIVATE Dataset." *Earth System Science Data* 15, no. 8 (August 3, 2023): 3419–72. https://doi.org/10.5194/essd-15-3419-2023.

Stephens, Graeme L., and Thomas J. Greenwald. "The Earth's Radiation Budget and Its Relation to Atmospheric Hydrology: 2. Observations of Cloud Effects." *Journal of Geophysical Research: Atmospheres* 96, no. D8 (1991): 15325–40. https://doi.org/10.1029/91JD00972.

Stevens, Bjorn, William R. Cotton, Graham Feingold, and Chin-Hoh Moeng. "Large-Eddy Simulations of Strongly Precipitating, Shallow, Stratocumulus-Topped Boundary Layers," December 1, 1998. https://journals.ametsoc.org/view/journals/atsc/55/24/1520-0469_1998_055_3616_lesosp_2.0.co_2.xml.

Stevens, Bjorn, and Graham Feingold. "Untangling Aerosol Effects on Clouds and Precipitation in a Buffered System." *Nature* 461, no. 7264 (October 2009): 607–13. https://doi.org/10.1038/nature08281.

Strapp, J. Walter, W. R. Leaitch, and P. S. K. Liu. "Hydrated and Dried Aerosol-Size-Distribution Measurements from the Particle Measuring Systems FSSP-300 Probe and the Deiced PCASP-100X Probe," October 1, 1992. https://journals.ametsoc.org/view/journals/atot/9/5/1520-0426_1992_009_0548_hadasd_2_0_co_2.xml.

Tang, Ignatius N. "Chemical and Size Effects of Hygroscopic Aerosols on Light Scattering Coefficients." *Journal of Geophysical Research: Atmospheres* 101, no. D14 (1996): 19245–50. https://doi.org/10.1029/96JD03003.

Twomey, S. "The Influence of Pollution on the Shortwave Albedo of Clouds," July 1, 1977. https://journals.ametsoc.org/view/journals/atsc/34/7/1520-0469_1977_034_1149_tiopot_2_0_co_2.xml.

vanZanten, M. C., B. Stevens, G. Vali, and D. H. Lenschow. "Observations of Drizzle in Nocturnal Marine Stratocumulus," January 1, 2005. https://doi.org/10.1175/JAS-3355.1.

Watson-Parris, Duncan, and Christopher J. Smith. "Large Uncertainty in Future Warming Due to Aerosol Forcing." *Nature Climate Change* 12, no. 12 (December 2022): 1111–13. https://doi.org/10.1038/s41558-022-01516-0.

Wood, R. "Drizzle in Stratiform Boundary Layer Clouds. Part I: Vertical and Horizontal Structure," September 1, 2005. https://doi.org/10.1175/JAS3529.1.

Wood, R., M. A. Vogt, and I. L. McCoy. "Aggressive Aerosol Mitigation Policies Reduce Chances of Keeping Global Warming to Below 2C." *Earth's Future* 12, no. 7 (2024): e2023EF004233. https://doi.org/10.1029/2023EF004233.

Wood, Robert. "Assessing the Potential Efficacy of Marine Cloud Brightening for Cooling Earth Using a Simple Heuristic Model." *Atmospheric Chemistry and Physics* 21, no. 19 (October 1, 2021): 14507–33. https://doi.org/10.5194/acp-21-14507-2021.

Wood, Robert. "Stratocumulus Clouds," August 1, 2012. https://doi.org/10.1175/MWR-D-11-00121.1.

Wood, Robert, and Christopher S. Bretherton. "On the Relationship between Stratiform Low Cloud Cover and Lower-Tropospheric Stability," December 15, 2006. https://doi.org/10.1175/JCLI3988.1.

Wood, Robert, Terence L. Kubar, and Dennis L. Hartmann. "Understanding the Importance of Microphysics and Macrophysics for Warm Rain in Marine Low Clouds. Part II: Heuristic Models of Rain Formation," October 1, 2009. https://doi.org/10.1175/2009JAS3072.1.

Woodcock, A. H. "SALT NUCLEI IN MARINE AIR AS A FUNCTION OF ALTITUDE AND WIND FORCE," October 1, 1953. https://journals.ametsoc.org/view/journals/atsc/10/5/1520-0469_1953_010_0366_snimaa_2_0_co_2.xml.

Zmijewski, Piotr, Piotr Dziekan, and Hanna Pawlowska. "Modeling Collision–Coalescence in Particle Microphysics: Numerical Convergence of Mean and Variance of Precipitation in Cloud Simulations

Using the University of Warsaw Lagrangian Cloud Model (UWLCM) 2.1." *Geoscientific Model Development* 17, no. 2 (January 30, 2024): 759–80. https://doi.org/10.5194/gmd-17-759-2024.

5.Supplemental figures and tables

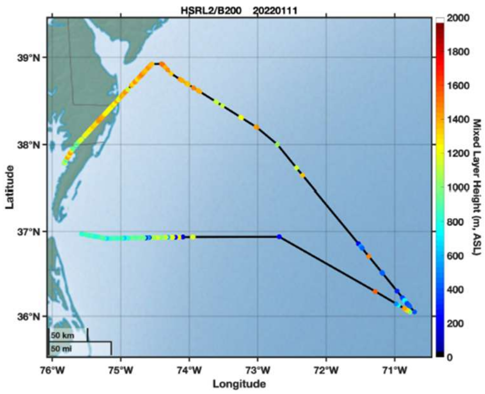
HSRL2/B200 20220111
Latitude
Longitude
Mixed Layer Height (m, ASL)
50 km
50 mi
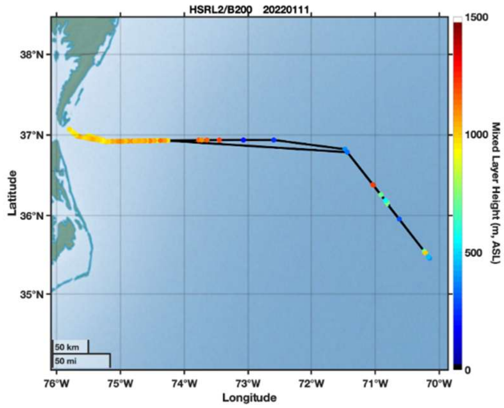
HSRL2/B200 20220111
Latitude
Longitude
Mixed Layer Height (m, ASL)
50 km
50 mi
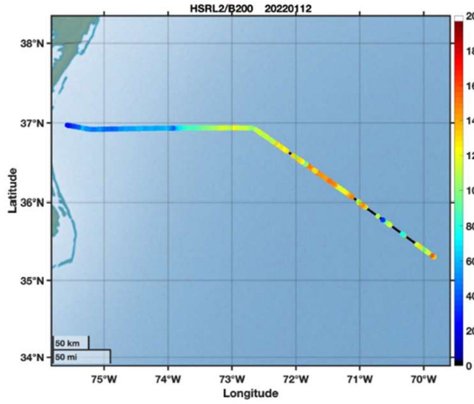
HSRL2/B200 20220112
Latitude
Longitude
Mixed Layer Height (m, ASL)
50 km
50 mi
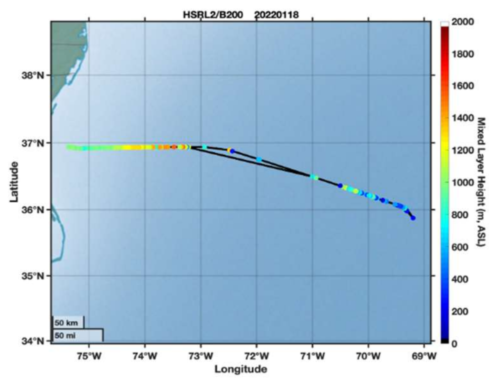
HSRL2/B200 20220118
Latitude
Longitude
Mixed Layer Height (m, ASL)
50 km
50 mi
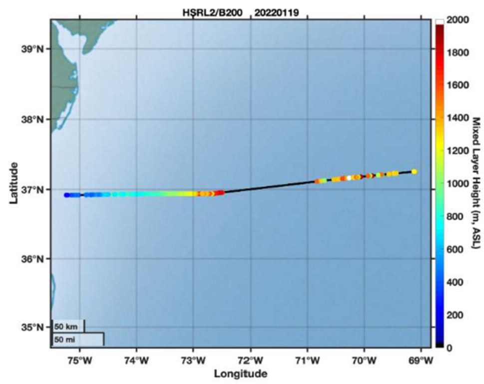
HSRL2/B200 20220119
Latitude
Longitude
Mixed Layer Height (m, ASL)
50 km
50 mi
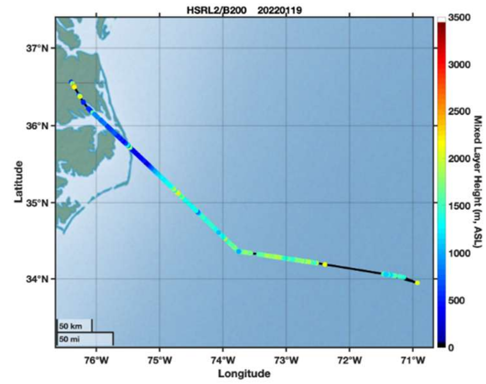
HSRL2/B200 20220119
Latitude
Longitude
Mixed Layer Height (m, ASL)
50 km
50 mi
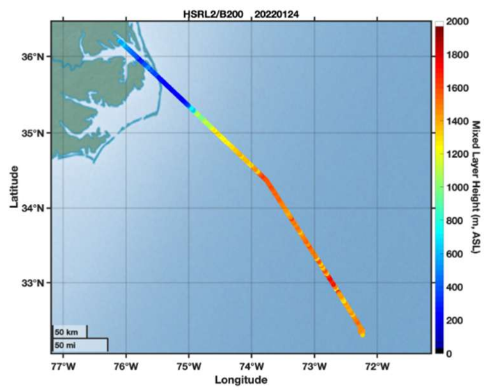
HSRL2/B200 20220124
Latitude
Longitude
Mixed Layer Height (m, ASL)
50 km
50 mi
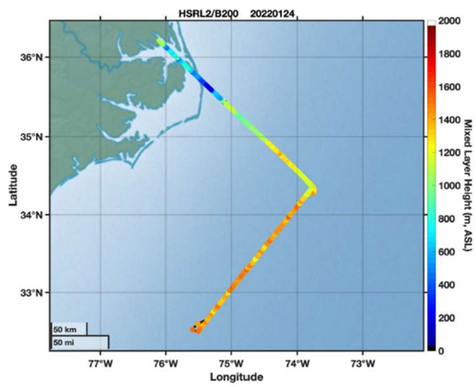
HSRL2/B200 20220124
Latitude
Longitude
Mixed Layer Height (m, ASL)
50 km
50 mi
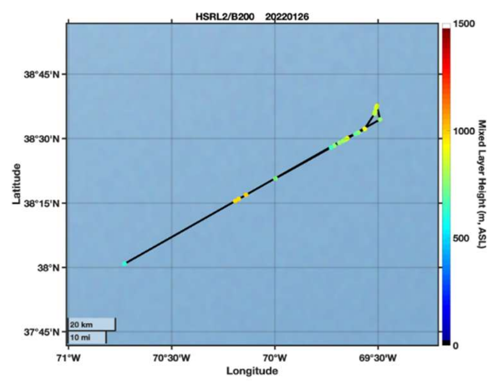
HSRL2/B200 20220126
Latitude
Longitude
Mixed Layer Height (m, ASL)
20 km
10 mi
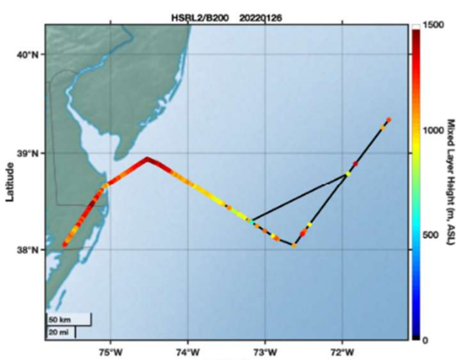
HSRL2/B200 20220126
Latitude
Longitude
Mixed Layer Height (m, ASL)
50 km
20 mi
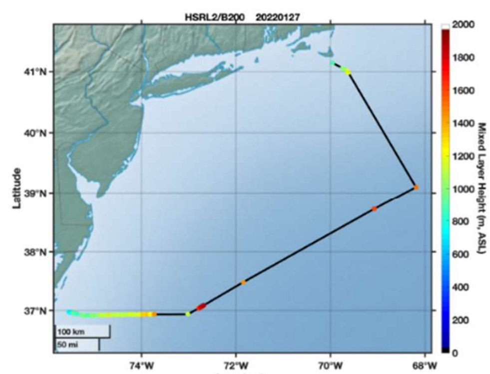
HSRL2/B200 20220127
Latitude
Longitude
Mixed Layer Height (m, ASL)
100 km
50 mi
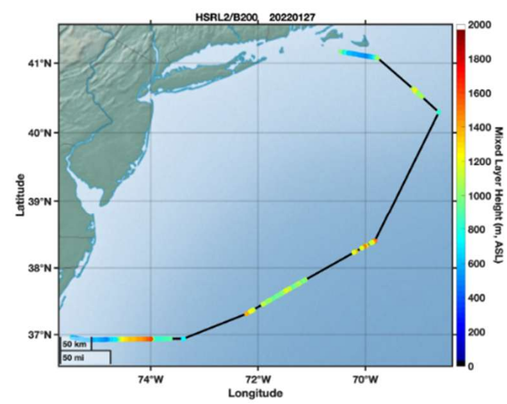
HSRL2/B200 20220127
Latitude
Longitude
Mixed Layer Height (m, ASL)
50 km
50 mi

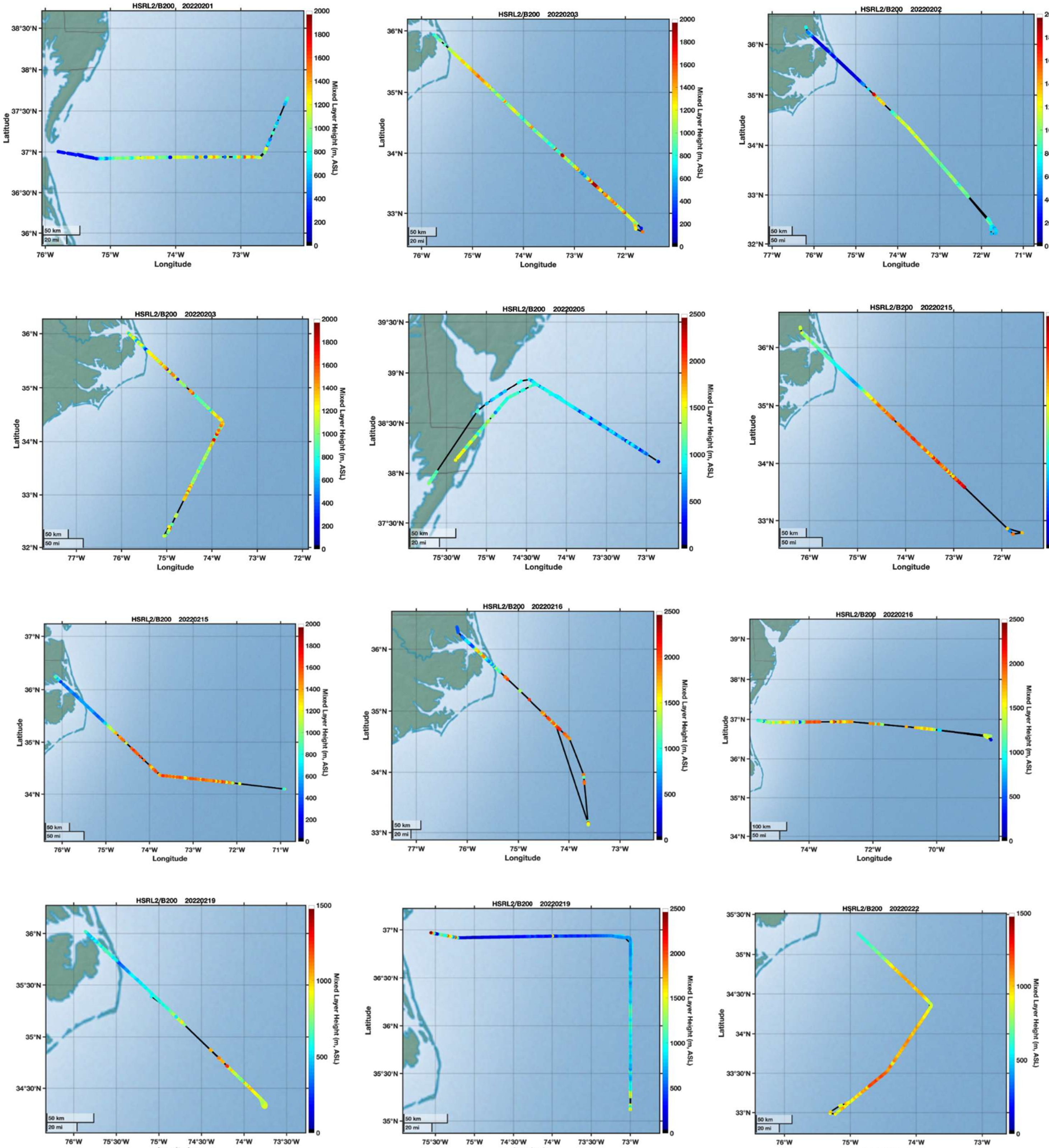
HSRL2/B200 20220201
HSRL2/B200 20220203
HSRL2/B200 20220202
HSRL2/B200 20220203
HSRL2/B200 20220205
HSRL2/B200 20220215
HSRL2/B200 20220215
HSRL2/B200 20220216
HSRL2/B200 20220216
HSRL2/B200 20220219
HSRL2/B200 20220219
HSRL2/B200 20220222
Latitude
Longitude
Mixed Layer Height (m, ASL)

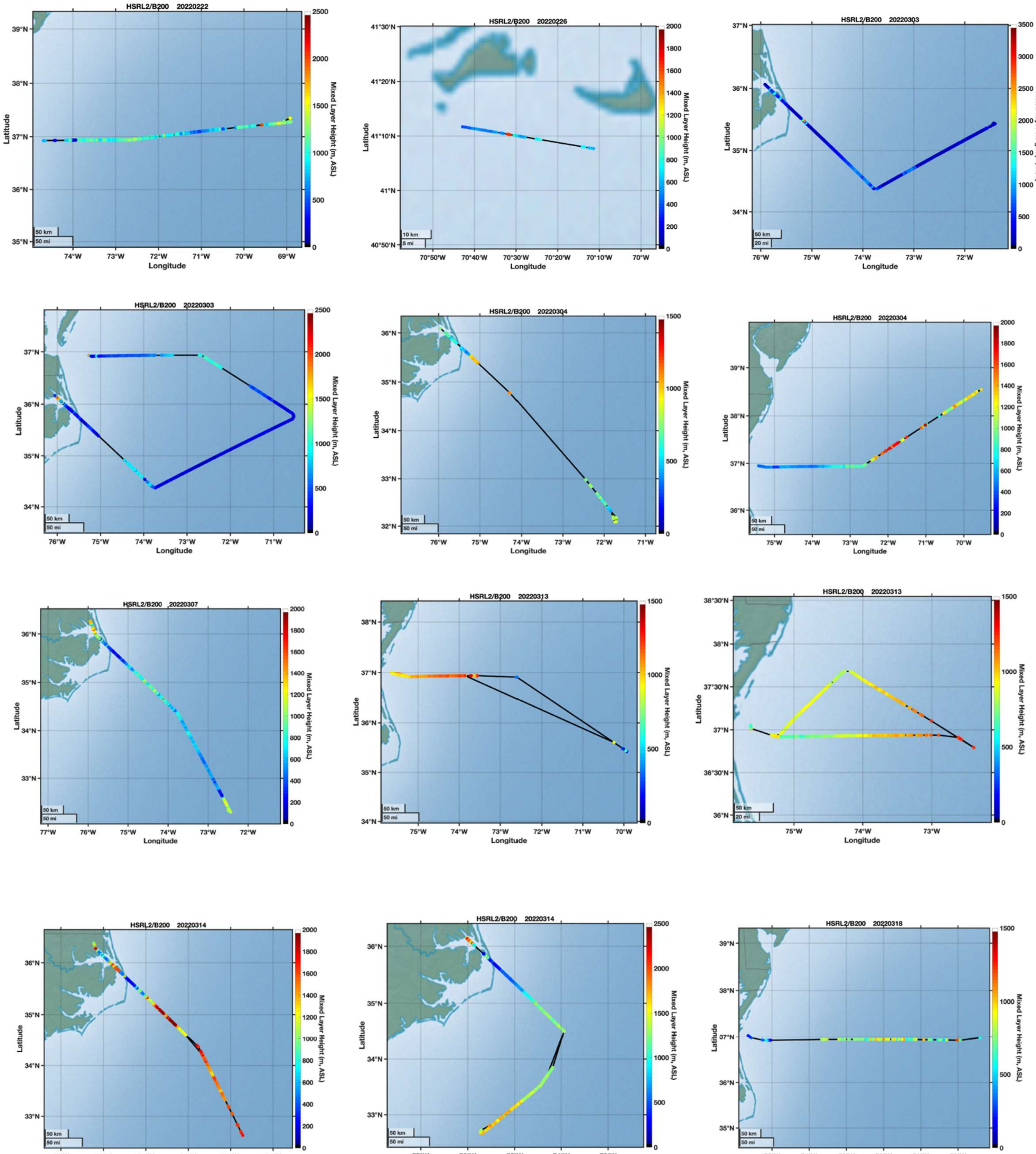
HSRL2/B200 20220222
HSRL2/B200 20220226
HSRL2/B200 20220303
HSRL2/B200 20220303
HSRL2/B200 20220304
HSRL2/B200 20220304
HSRL2/B200 20220307
HSRL2/B200 20220313
HSRL2/B200 20220313
HSRL2/B200 20220314
HSRL2/B200 20220314
HSRL2/B200 20220318
Latitude
Longitude
Mixed Layer Height (m, ASL)
50 km
50 mi

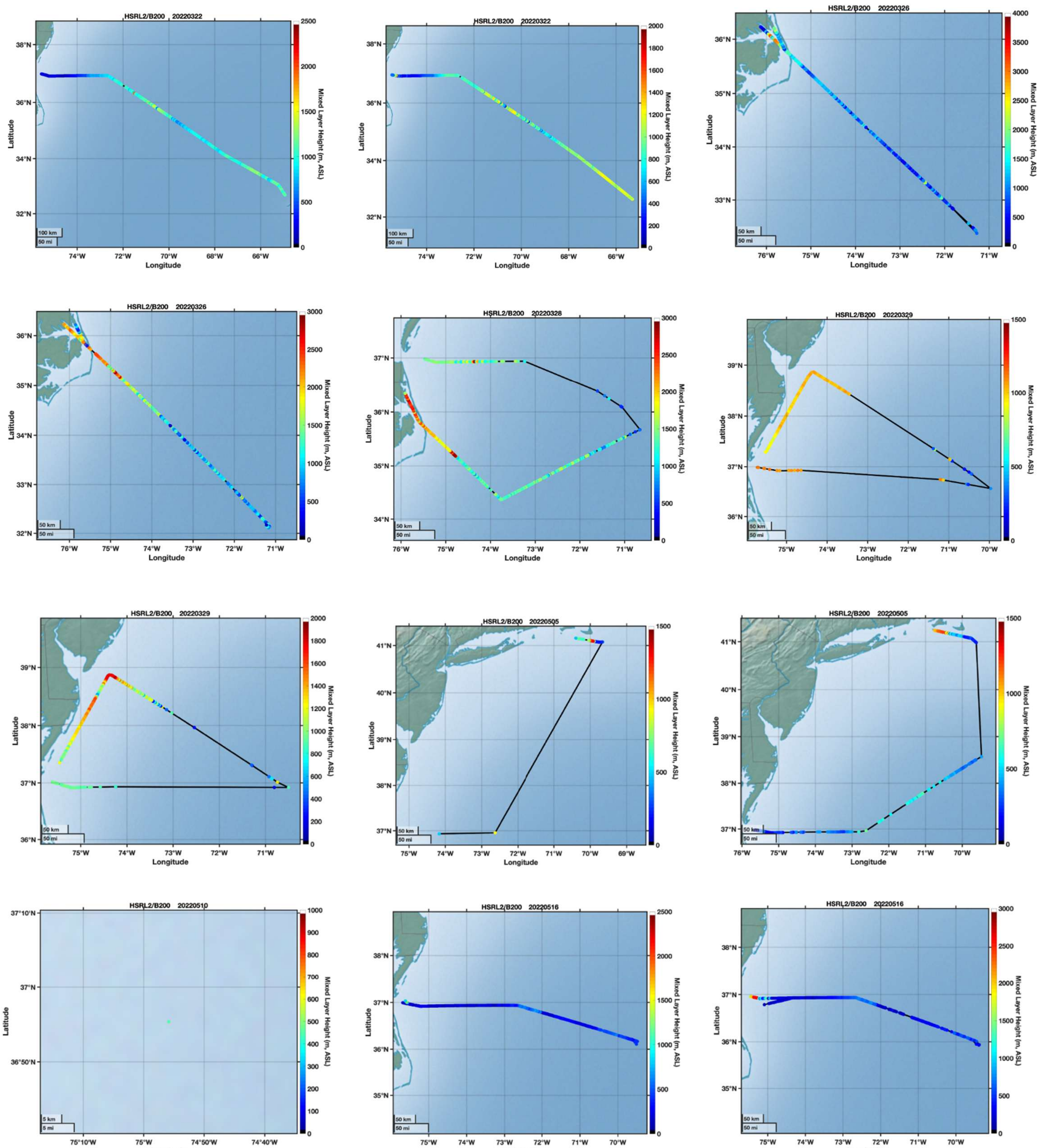
HSRL2/B200 20220322
HSRL2/B200 20220322
HSRL2/B200 20220326
HSRL2/B200 20220326
HSRL2/B200 20220328
HSRL2/B200 20220329
HSRL2/B200 20220329
HSRL2/B200 20220505
HSRL2/B200 20220505
HSRL2/B200 20220510
HSRL2/B200 20220516
HSRL2/B200 20220516
Latitude
Longitude
Mixed Layer Height (m, ASL)

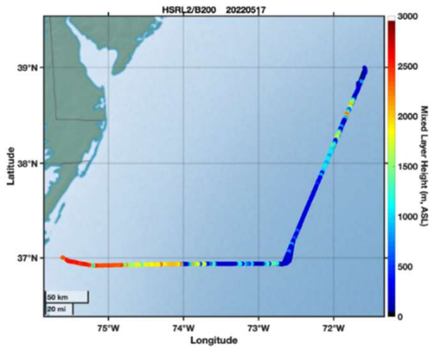
HSRL2/B200 20220517
Latitude
Longitude
Mixed Layer Height (m, ASL)
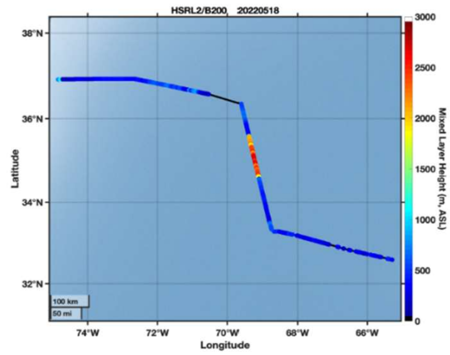
HSRL2/B200 20220518
Latitude
Longitude
Mixed Layer Height (m, ASL)
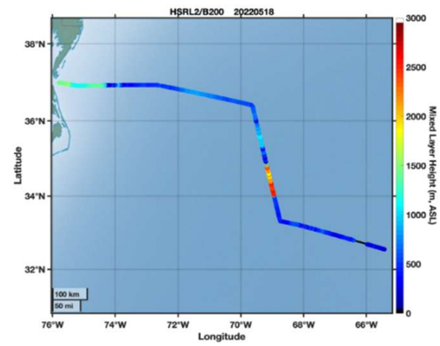
HSRL2/B200 20220518
Latitude
Longitude
Mixed Layer Height (m, ASL)
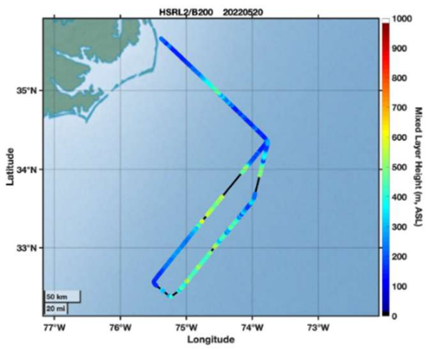
HSRL2/B200 20220520
Latitude
Longitude
Mixed Layer Height (m, ASL)
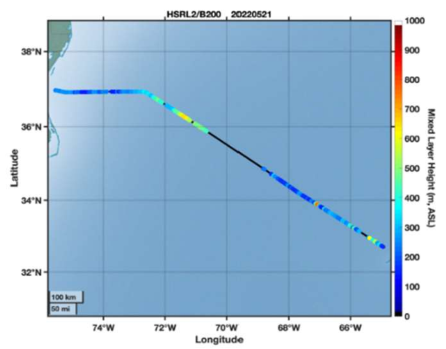
HSRL2/B200 20220521
Latitude
Longitude
Mixed Layer Height (m, ASL)
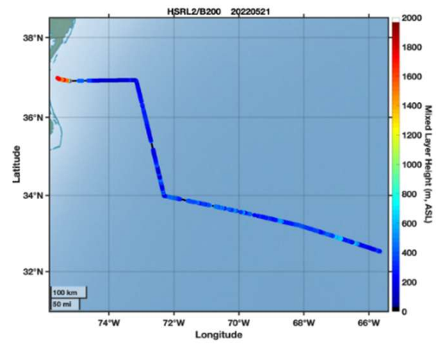
HSRL2/B200 20220521
Latitude
Longitude
Mixed Layer Height (m, ASL)
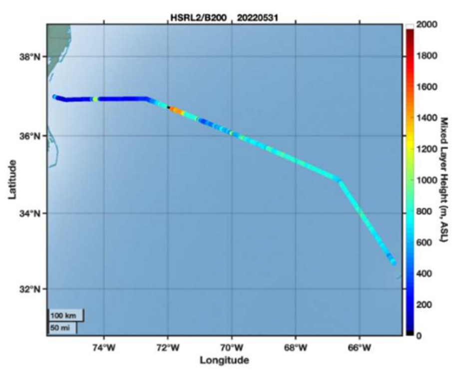
HSRL2/B200 20220531
Latitude
Longitude
Mixed Layer Height (m, ASL)
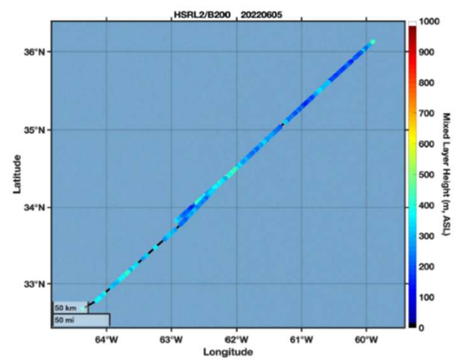
HSRL2/B200 20220605
Latitude
Longitude
Mixed Layer Height (m, ASL)
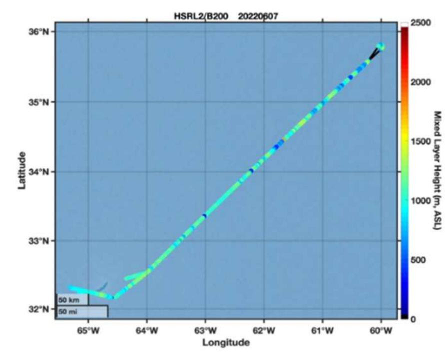
Latitude
Longitude
Mixed Layer Height (m, ASL)
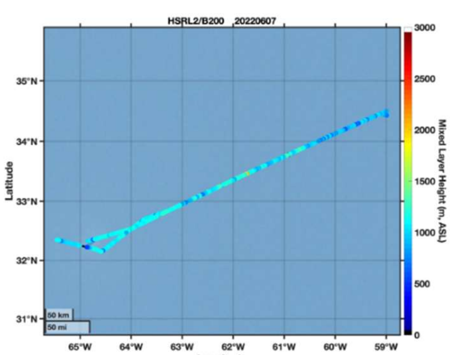
HSRL2/B200 20220607
Latitude
Longitude
Mixed Layer Height (m, ASL)
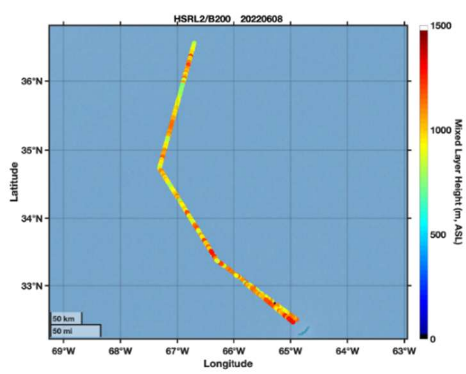
HSRL2/B200 20220608
Latitude
Longitude
Mixed Layer Height (m, ASL)
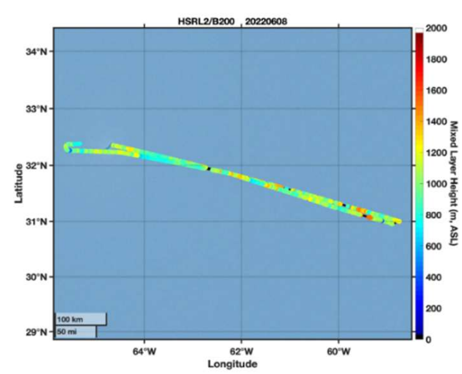
HSRL2/B200 20220608
Latitude
Longitude
Mixed Layer Height (m, ASL)

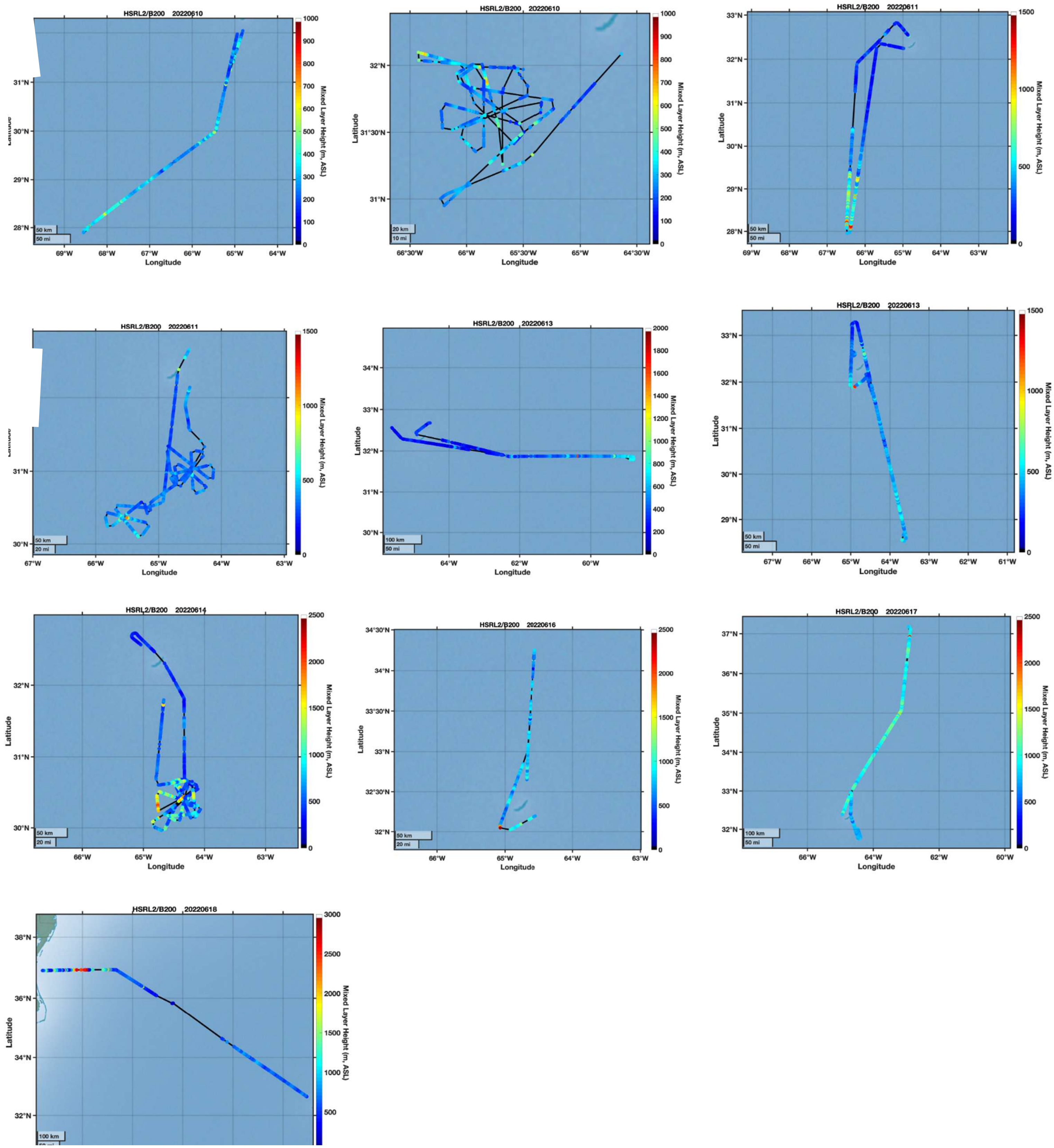

Supplemental Figure 1HSSLR-2 lidar images for the flight paths from all 76 flights utilized in this study for 43 dates spanning January 11 to June 18, 2022. Images show the aircraft flight paths as a function of mixed layer boundary height (m). Some flight paths were the same "out and back", others traveled one path out from Langley and a different path back. Of the 43 dates utilized, 26 of the days involved two flights per day.

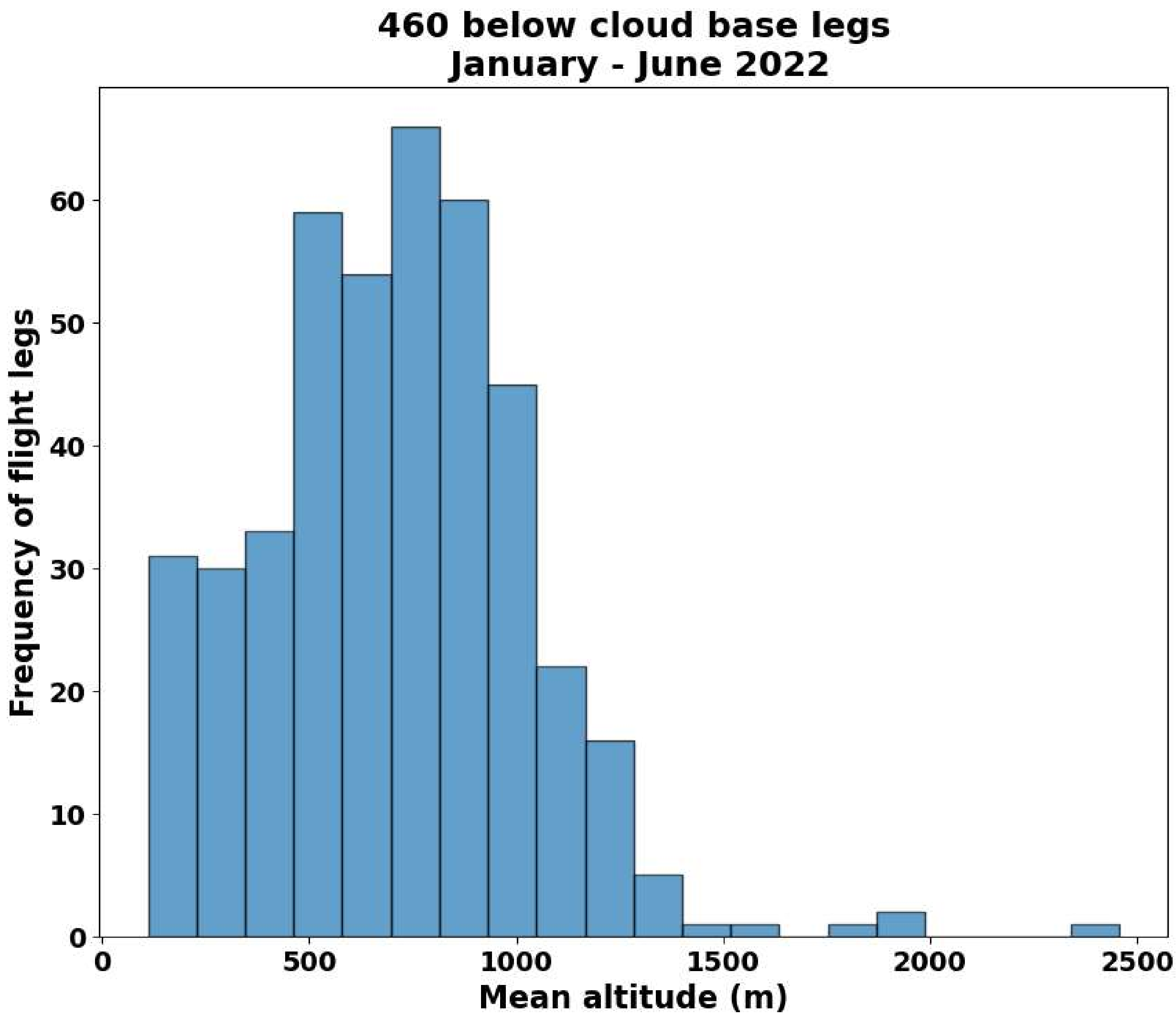

Supplemental Figure 2 The full distribution of average flight leg altitude for all 460 below cloud base legs analyzed in this study.

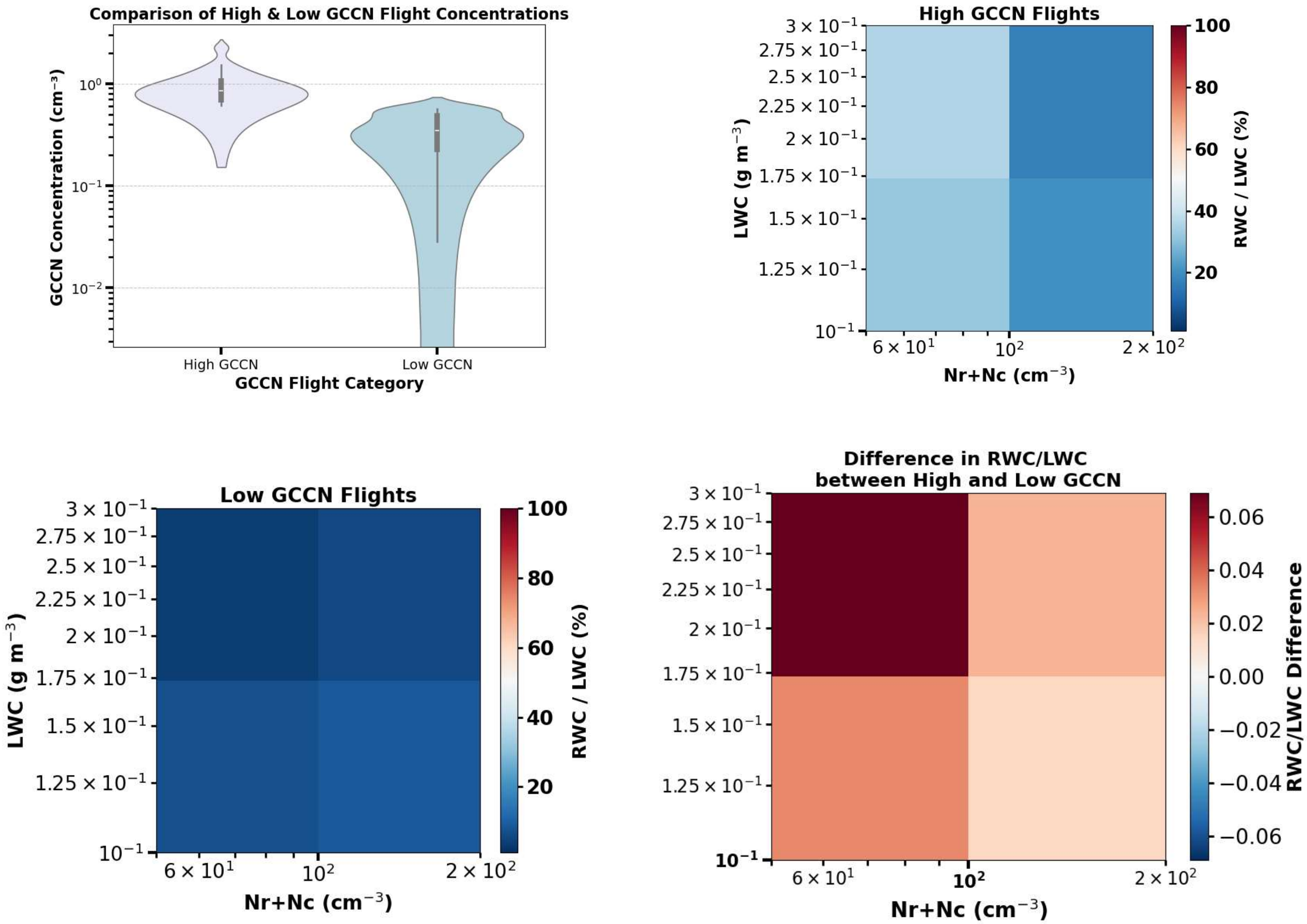

Supplemental Figure 3 RWC as a function of fixed LWC and concentration for a "high GCCN" concentration top 40% split and a bottom 60% "low GCCN" concentration. Higher RWC and higher RWC difference is shown in warmer colors. Violin plot median is shown in white and the IQR is gray. The width of each violin represents the density of data points.

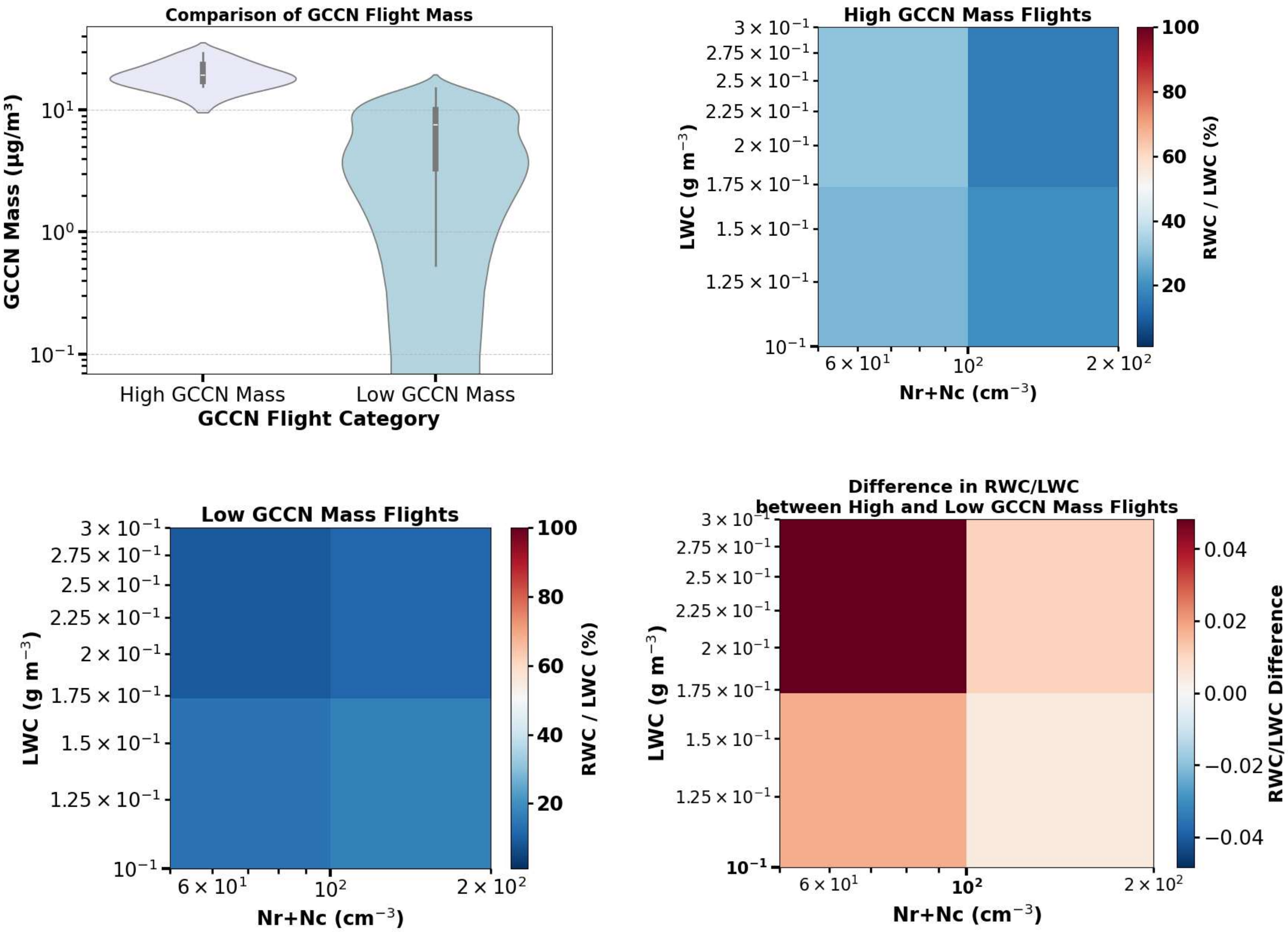

Supplemental Figure 4 RWC as a function of fixed LWC and concentration for a "high GCCN" mass top 20% split and a bottom 80% "low GCCN" mass. Higher RWC and higher RWC difference is shown in warmer colors. Violin plot median is shown in white and the IQR is gray. The width of each violin represents the density of data points.

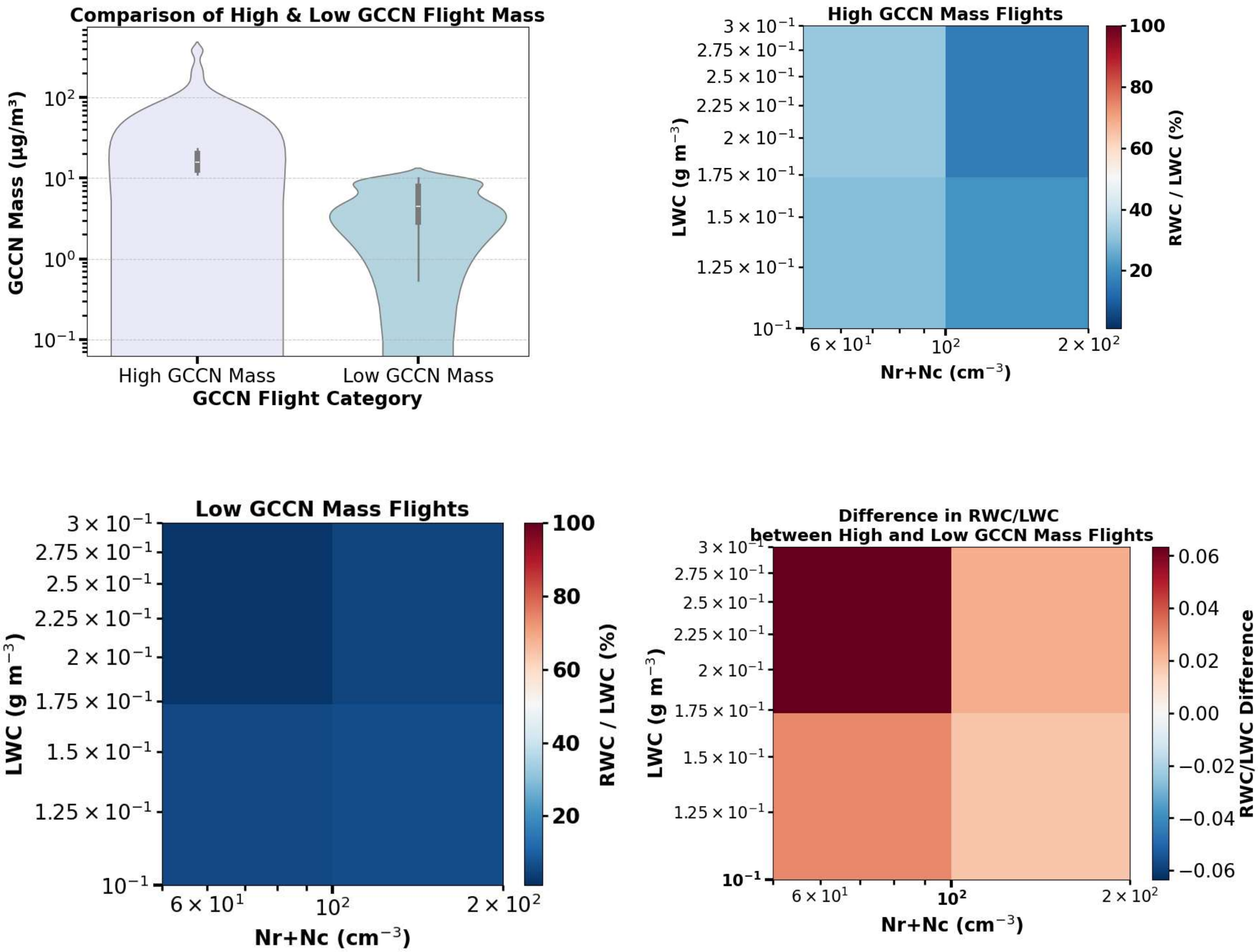

Supplemental Figure 5 RWC as a function of fixed LWC and concentration for a "high GCCN" mass top 40% split and a bottom 60% "low GCCN" mass. Higher RWC and higher RWC difference is shown in warmer colors. Violin plot median is shown in white and the IQR is gray. The width of each violin represents the density of data points.